Control of Structure and Function of Block Copolymer Nanoparticles Manufactured in Microfluidic Reactors: Towards Drug Delivery Applications

by

Zheqi Xu
B.Eng., Zhejiang University, 2012

A Thesis Submitted in Partial Fulfillment
of the Requirements for the Degree of

MASTER OF SCIENCE

in the Department of Chemistry

Supervisory Committee

Control of Structure and Function of Block Copolymer Nanoparticles Manufactured in Microfluidic Reactors: Towards Drug Delivery Applications

by

Zheqi Xu
B.Eng., Zhejiang University, 2012

Supervisory Committee

Dr. Matthew G. Moffitt, Department of Chemistry
Supervisor

Dr. Cornelia Bohne, Department of Chemistry
Departmental Member

Dr. Mohsen Akbari, Department of Mechanical Engineering
Outside Member

Abstract

Supervisory Committee
Dr. Matthew G. Moffitt, Department of Chemistry
Supervisor
Dr. Cornelia Bohne, Department of Chemistry
Departmental Member
Dr. Mohsen Akbari, Department of Mechanical Engineering
Outside Member

This thesis includes three studies on related aspects of structure and function control for drug delivery block copolymer nanoparticles manufactured in segmented gas-liquid microfluidic reactors. First, the self-assembly of a series of photoresponsive poly(*o*-nitrobenzyl acrylate)-*b*-polydimethylacrylamide copolymers is conducted in the gas-liquid segmented microfluidic reactor at various flow rates. The resulting morphologies are found to be flow-variable and distinct from nanoparticles prepared off-chip by dropwise water addition. Photocleaving of the nanoparticles formed at different flow rates reveal flow-variable photodissociation kinetics. Next, we conduct a direct comparison between a commercially-available single-phase microfluidic mixer and the two-phase, gas-liquid segmented microfluidic reactor used in our group, with respect to nanoparticle formation from a typical block copolymer identified for drug delivery applications, polycaprolactone-*b*-poly(ethylene oxide). The two-phase chip yields morphologies and core crystallinities that vary with flow rate; however, the same parameters are found to be flow-independent using the single-phase mixer. This study provides the first direct evidence that flow-variable structure control is a unique feature of the two-phase chip design. Finally, we investigate structure and function control for paclitaxel (PAX)-loaded nanoparticles prepared from a series of poly(6-methyl caprolactone-*co*-*ε*-caprolactone)-*block*-poly(ethylene oxide) copolymers with variable 6-methyl caprolactone (MCL) content. For all MCL-containing copolymers, off-chip preparations form nanoparticles with no measurable crystallinity, although PAX loading levels are higher and release rates are slower compared to the copolymer without MCL. Both off-chip and on-chip preparations yield amorphous spheres of similar size from MCL-containing copolymers, although on-chip nanoparticles showed slower release rates, attributed to more homogeneous PAX distribution due to faster mixing.

Table of Contents

List of Tables

List of Figures

List of Schemes

List of Abbreviations

^{1}H NMR	proton nuclear magnetic resonance
ACN	acetonitrile
AIBN	2,-2’-azobisisobutyronitrile
cwc	critical water content
DCM	dichloromethane
DLS	dynamic light scattering
DMF	N,N-dimethylformamide
DSC	differential scanning calorimeter
GPC	gel permeation chromatography
HPLC	high performance liquid chromatography
LCM	large compound micelle
MCL	6-methyl caprolactone
MWCO	molecular weight cut off
MS	mass spectrometry
PAA	poly(acrylic acid)
PAX	paclitaxel
PBS	phosphate buffer saline
PCL	polycaprolactone
PDI	polydispersity index
PDMA	polydimethylacrylamide
PDMS	polydimethylsiloxane

PEO	poly(ethylene oxide)
PNBA	poly(*o*-nitrobenzyl acrylate)
PS	polystyrene
SLS	static light scattering
TEM	transmission electron microscopy
UV	ultraviolet
XRD	X-ray diffraction

Acknowledgments

First and foremost, I would like to express my gratitude to my supervisor Dr. Matthew Moffitt for the continuous support of my master study and research, for his patience, knowledge and encouragement.

Thanks to everyone in the group. Aman, who guided me through training and answered my questions when I had difficulties; Changhai, who made the copolymers for my project and gave me insightful advice on the direction of research; Alex, who shared his experience with me and helped me when I needed; Brian, Fraser, Yimeng, Amy, Jeff, Sabrina, and Sun for all the fun we had together.

My sincere thanks also go to Patrick Nahirney, Brad Ross and Chris Barr for letting me use their TEM and NMR and for teaching me to operate these instruments; to Prof. Yue Zhao at University of Sherbrooke for providing me with copolymers and advices on photochemical experiments; to Fyles group and van Veggel group for the permission to use their instruments; to Andrew MacDonald and Jeff Trafton for fixing my instrumental problems. Without their precious support it would not be possible to conduct this research.

I would like to thank my family and friends who spent time with me no matter we were together or physically apart. Thank you, mom, for your understanding and your courage to get over all the difficulties without me there. Thank you, grandparents, for the continuous support over these 26 years and the joyful moments from our weekly conversations.

Chapter 1.

General Introduction

1.1. General Introduction to Polymers

1.1.1. What is Polymer?

Polymers are long-chain molecules of very high molecular weight, composed of many repeated monomers linked by covalent bonds.[1] When monomers form a polymer, they are called repeat units. Polymer structural formulas are typically written as the chemical structure of the monomer in brackets with the number of average number of repeat unit in subscripts. For example, a polyethylene chain sample made up of chains with an average of 100 repeat units can be written:

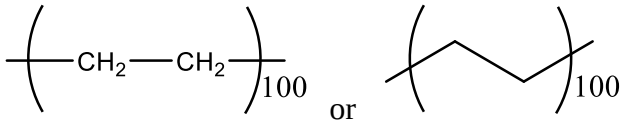

(1-1)

The number of repeat units is called the degree of polymerization.

Polymers can be categorized according to their chain architecture into linear polymers, branched polymers and network polymers.[2] As shown in Figure 1-1A, in a linear polymer each repeat unit possesses two linkages with other repeat units to form a linear chain. When a small number of repeat units possess linkages to three or more repeat units, a branched polymer is formed (Figure 1-1B). Branched polymers may have side chains made up of repeat units that are either the same or different from the repeat units on the backbone. In network polymers (Figure 1-1C), the degree of branching is high enough such that chains are interconnected to form a three-dimensional structures. These materials are usually very tough.

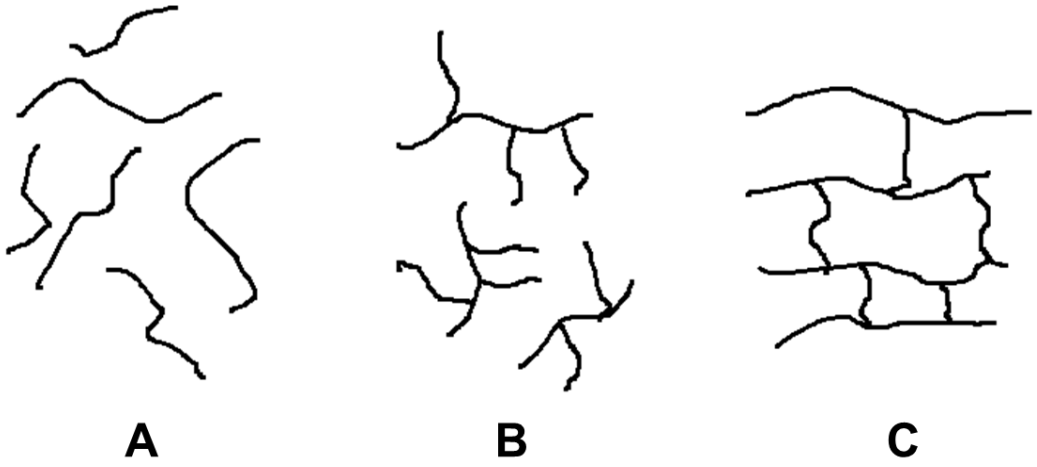

Figure 1-1. Linear (A), branched (B) and network polymers (C).

Polymers can also be divided into different types according to the arrangement of monomers.[3] Polymers containing two or more types of monomers are called copolymers. Statistical copolymers are those in which the distribution of the monomers is statistical in nature, according to the relative reactivities of those monomers. Statistical copolymers consisting of monomers with identical reactivities are called random copolymers (Figure 1-2A). Alternating copolymers (Figure 1-2B), as the name suggests, have two types of monomers distributed in alternating sequence. Block copolymers (Figure 1-2C) consist of blocks of each type of monomer. Finally, in graft copolymers (Figure 1-2D), side chains of one type of monomer are attached, or grafted, to a backbone of another type of monomer.

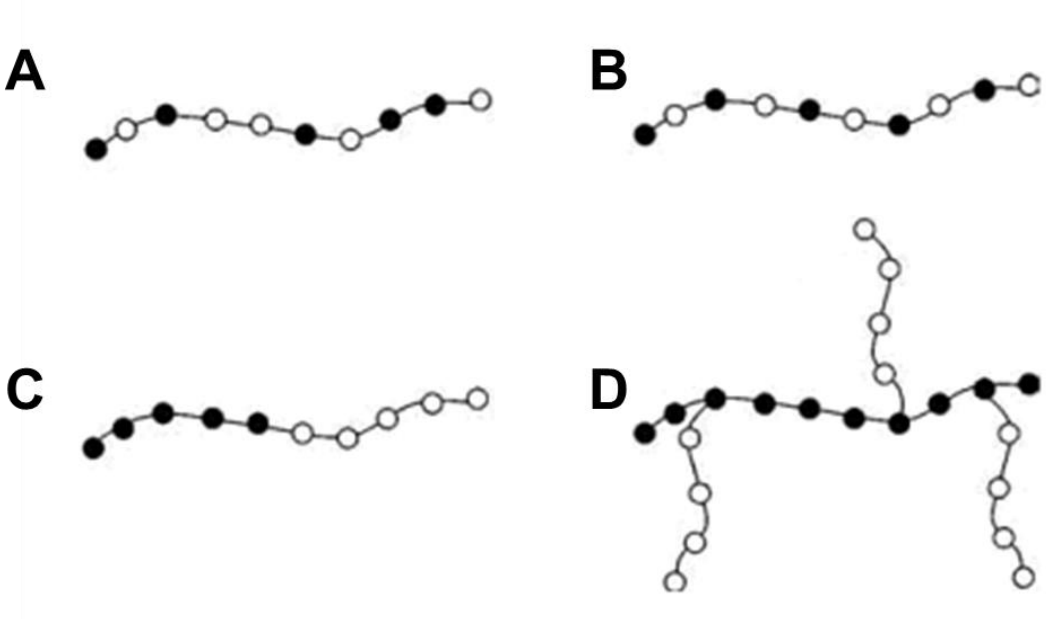

Figure 1-2. Statistical/random (A), alternating (B), block (C) and graft copolymers (D).

1.1.2. Molecular Weight of Polymers

The same polymer type of different molecular weights has different chemical and physical properties. Therefore, determination of the molecular weight is important. Unlike small molecules, polymers don't have an exact molecular weight, but rather a distribution of molecular weights. There are two major types of molecular weight averages that are usually used: the number-average molecular weight, M_n, and the weight-average molecular weight, M_w. They are defined as:

$$M_n = \frac{\sum_i N_i M_i}{\sum_i N_i} \tag{1-2}$$

$$M_w = \frac{\sum_i N_i {M_i}^2}{\sum_i N_i M_i} \tag{1-3}$$

For monomodal distributions, M_n is the smaller than M_w (Figure 1-3).

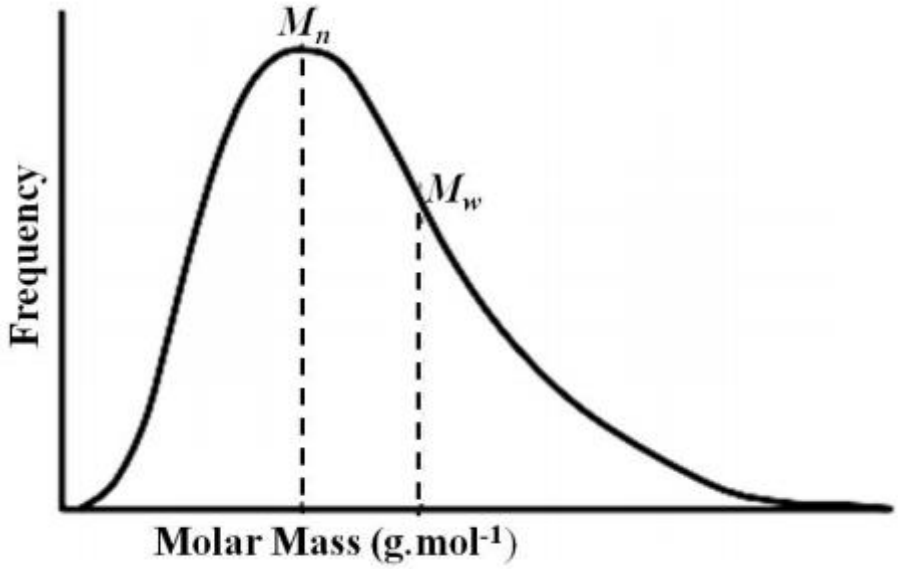

Figure 1-3. Molecular weight distribution of a typical single-peaked polymer sample.[4]

A broader distribution of chain molecular weights is described as a more polydisperse polymer sample. Polydispersity is characterized by the polydispersity index (PDI) (Equation 1-4). A monodisperse sample has PDI = 1. High PDI (> 2) corresponds to a broad distribution.

$$\text{PDI} = \frac{M_w}{M_n} \tag{1-4}$$

Mean polymer molecular weight can be measured using a wide range of techniques, including static light scattering (SLS), gel permeation chromatography (GPC), and mass spectrometry (MS).

1.1.3. Glass Transition

A characteristic thermal transition of polymers is the glass transition. Unlike polymer crystallization, which is a first-order transition, the glass transition is a second-order transition leading to a peak in the heat capacity with respect to temperature.[1] Below the glass transition temperature (T_g), chains are kinetically locked with no thermal

rotational or conformational mobility, making the polymer solid and glassy macroscopically (glassy state in Figure 1-4). At the glass transition temperature, the polymer starts to soften and becomes rubbery (rubbery plateau in Figure 1-4). If the temperature further increases, the polymer will flow like a viscous liquid (liquid flow in Figure 1-4). The T_g can be measured by differential thermal analysis (DTA) and differential scanning calorimetry (DSC).

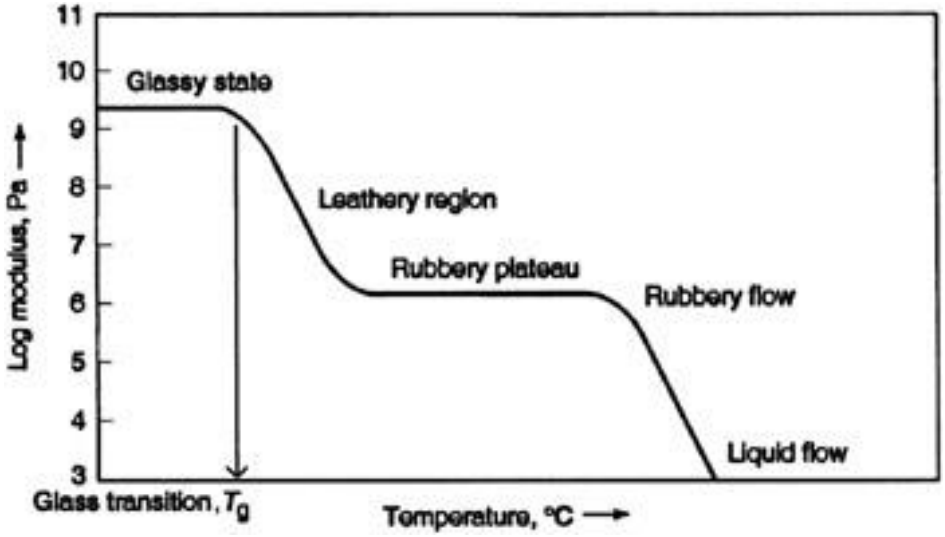

Figure 1-4. Young's modulus of a typical polymer material versus temperature.[5]

1.1.4. Amorphous and Semicrystalline Polymers

Amorphous polymers don't contain any crystalline regions (Figure 1-5A). Polymers with crystalline regions exhibit X-ray diffraction patterns, but they are generally only semicrystalline, possessing a fair amount of amorphous materials (Figure 1-5).

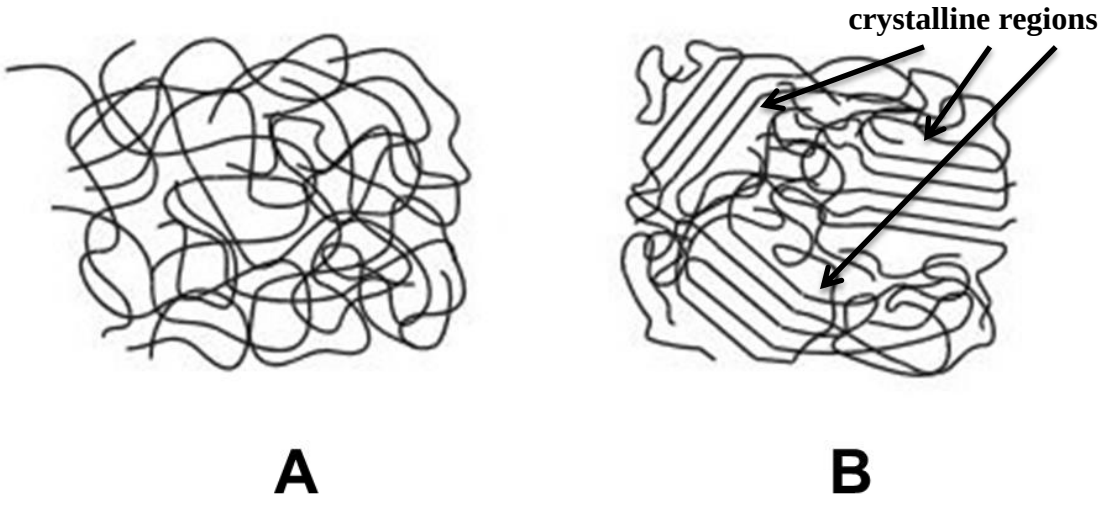

Figure 1-5. Amorphous (A) and semicrystalline polymers (B).

Below the glass transition temperature, amorphous polymers are glassy. Above the glass transition temperature, crosslinked amorphous polymers are rubbery, while non-crosslinked ones are viscoeleastic that exhibit both viscous and elastic characteristics.

Crystallization is a first-order transition leading to softening below the melting temperature (T_m).[1] Unlike small molecules, polymer chains tend to entangle that restricts packing of chains to form crystallites. Therefore, we characterize them as semicrystalline, meaning amorphous regions still exist in semicrystalline polymers below T_m. Whether a polymer is semicrystalline or amorphous depends on its structure and intermolecular forces. If it has ordered structure and strong intermolecular force, it is more likely to be semicrystalline. For semicrystalline polymers, T_m is always higher than T_g, as chains can't move to form crystallites below the T_g. Crystallites scatter light, thus semicrystalline polymers are usually non-transparent. The percentage of crystallinity of a polymer is defined as:

$$\%\ \text{Crystallinity} = \frac{weight\ of\ crystalline\ region}{weight\ of\ total\ material} \times 100\% \qquad (1\text{-}5)$$

Percent crystallinity can be measure by DSC and XRD. XRD is used for this thesis. The detailed calculation will be discussed later in the experimental.

1.2. Block Copolymer Micelles

1.2.1. Formation of Block Copolymer Micelles

Block copolymers in solution undergo micellization (Figure 1-6) in a selected solvent, which is able to dissolve one block but not another, under specific conditions. The core of micelles is formed by the insoluble blocks, while the corona contains soluble blocks. If the corona-forming block is much longer than the core-forming block, the result is called a star micelle. If instead the corona-forming block is much shorter than the core-forming block, the result is called a crew-cut micelle. At fixed temperature and solvent conditions, micellization occurs on increasing the copolymer concentration above the critical micelle concentration (cmc).[6] At fixed temperature and initial copolymer concentration, micellization occurs on increasing the water content above the critical water content (cwc). Block copolymer are referred to as nanoparticles in this thesis.

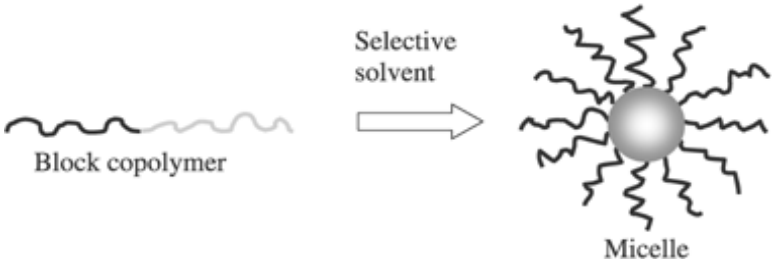

Figure 1-6. Micellization of block copolymer.[7]

1.2.2. Thermodynamics of Micellization

Micellization, as a spontaneous process, is a process driven by minimization of the Gibbs free energy (*G*) of the system. At constant temperature: [8]

$$\Delta G = \Delta H - T\Delta S \quad (1\text{-}6)$$

For nanoparticles in equilibrium just above the cmc:[9, 10]

$$\Delta G \approx \mathrm{R}T\ln(\mathrm{cmc}) \quad (1\text{-}7)$$

$$\Delta H = \mathrm{R}\left(\frac{\partial \ln(cmc)}{\partial \frac{1}{T}}\right) \quad (1\text{-}8)$$

Price and coworkers calculated ΔG, ΔH and $-T\Delta S$ of micellization of polystyrene-*b*-polyisoprene (PS-*b*-PI).[11] They prepared micelles by direct dissolution in n-hexadecane. The determined ΔG, ΔH and ΔS were all negative. Therefore it was an enthalpy-driven process. The negative enthalpy was from the large exothermic interchange energy when favourable PI-PI and solvent-solvent interactions replaced unfavourable PI-solvent interactions.

Alexandridis and coworkers calculated ΔG, ΔH and ΔS of micellization of PEO-*b*-PPO(polypropylene oxide)-*b*-PEO of different molecular weights by direct dissolution in water.[10] Unlike micellization in organic solvent, all changes in enthalpy and entropy were positive, indicating that micellization was an entropy-driven process. The increased entropy was from hydrophobic effect. The Gibbs free energy of micellization became more negative as the molecular weight increased or the percentage of hydrophobic block (PPO) increased, meaning that micelles were more readily formed. The enthalpy and entropy of micellization both became more positive as the molecular weight increased or as the percentage of PPO increased.

Shen and coworkers analyzed the thermodynamics of PS-*b*-PAA micelle formation in DMF by dropwise addition of water. All standard enthalpies, entropies and free energies of micellization in this system are negative in the water content range from 4.3 wt % to 5.0 wt %; therefore, micellization is driven by enthalpy in this case. However, an

increase in water content, a decrease in the PAA block length, or an increase in the PS block length lead to a decrease in the magnitude of the negative enthalpy and entropy of micellization values. When water content increased to 7.5 wt %, the standard entropy of micellization became positive while the standard enthalpy of micellization remained negative but small. However, after 15 wt % water content, the standard enthalpy of micellization became positive, making the increase in entropy the only driving force.[12]

In conclusion, for micelle formation in water-solvent mixture, whether the driving force is enthalpy or entropy depends on the solvent condition, water content, copolymer composition, chemistry of the copolymers and other factors. Entropy decreases upon micellization for various reasons: more stretched chains in the core, more stretched chains in the corona due to repulsion, and localization of chains to form order structures. Entropy increases upon micellization mainly because of the hydrophobic effect;[13] when water comes into contact with the hydrophobic chain, to avoid interaction with it, water molecules utilize hydrogen bonding to form a shell around it. Upon formation of micelles, water molecules become “free”, resulting in a significant increase in entropy. Enthalpy decreases upon micellization when the unfavourable hydrophobic interaction is replaced by favourable water-water interactions and segment-segment interactions of hydrophobic chains. Enthalpy increases upon micellization for two reasons, one is the destruction of hydrogen bonding upon micellization, and the other is the electrostatic repulsion of charged corona chains. According to Equation 1-6, the sign and magnitude of the entropy and enthalpy of micellization together, along with the temperature, determine whether micellization will occur.

1.2.3. Multiple Morphologies of Block Copolymer Nanoparticles

Block copolymers can form nanoparticles of multiple morphologies (Figure 1-7). From lower to higher curvature of structures, there are: spheres, rods/cylinders, cylinder network, vesicles, lamellae and large compound micelles. Nanoparticle morphology is controlled by three components of the free energy: (1) core-forming chain stretching, (2) interfacial energy and (3) interactions among corona-forming chains.[14, 15]

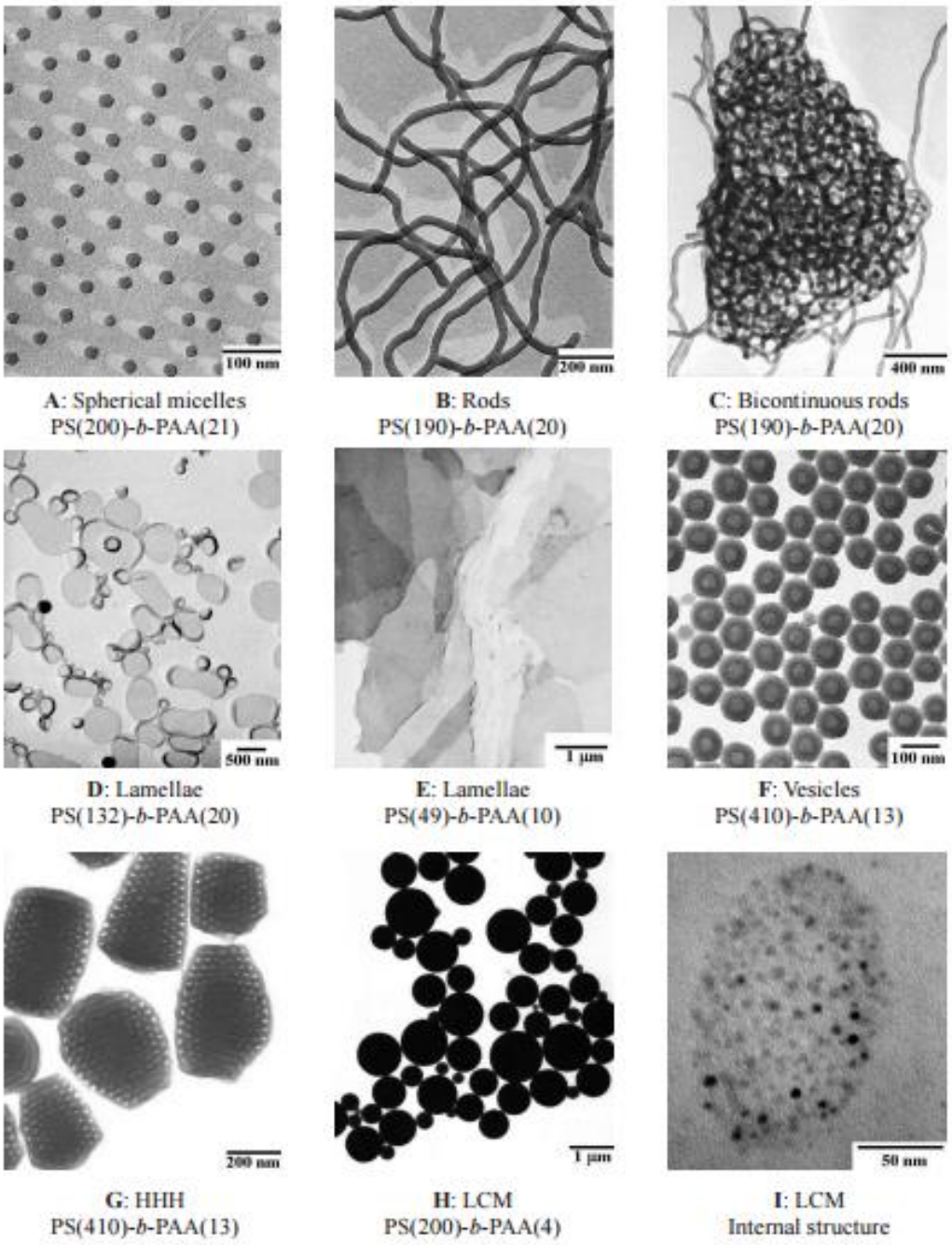

Figure 1-7. Multiple morphologies of PS-*b*-PAA. A. spheres. B. rods. C. bicontinuous rods. D. lamellae. E. lamellae (Platelets). F. vesicles. G. hexagonally packed hollow hoops. H. large compound micelles. I. internal structure of a large compound micelle.[16]

Eisenberg and coworkers has investigated various bottom-up control strategies of PS-*b*-PAA nanoparticle morphology.[17] Bottom-up control refers to chemical control by

changing copolymer composition, concentration, solvent condition, water content, pH and so on, while top-down control refers to external control such as shear, light, temperature, magnetic field and electric field. In Figure 1-8, by increasing polymer concentration and keeping water content constant, morphology changed from monodispersed spheres to mixture of spheres and short rods, and then to long cylinders. Since polymer molecular weight and composition were also constant, increasing polymer concentration increases aggregation number, thus PS chains in the core become more crowded and stretched. The tendency to lower chain stretching pushes curvature to lower. Therefore, lower curvature structures were formed.

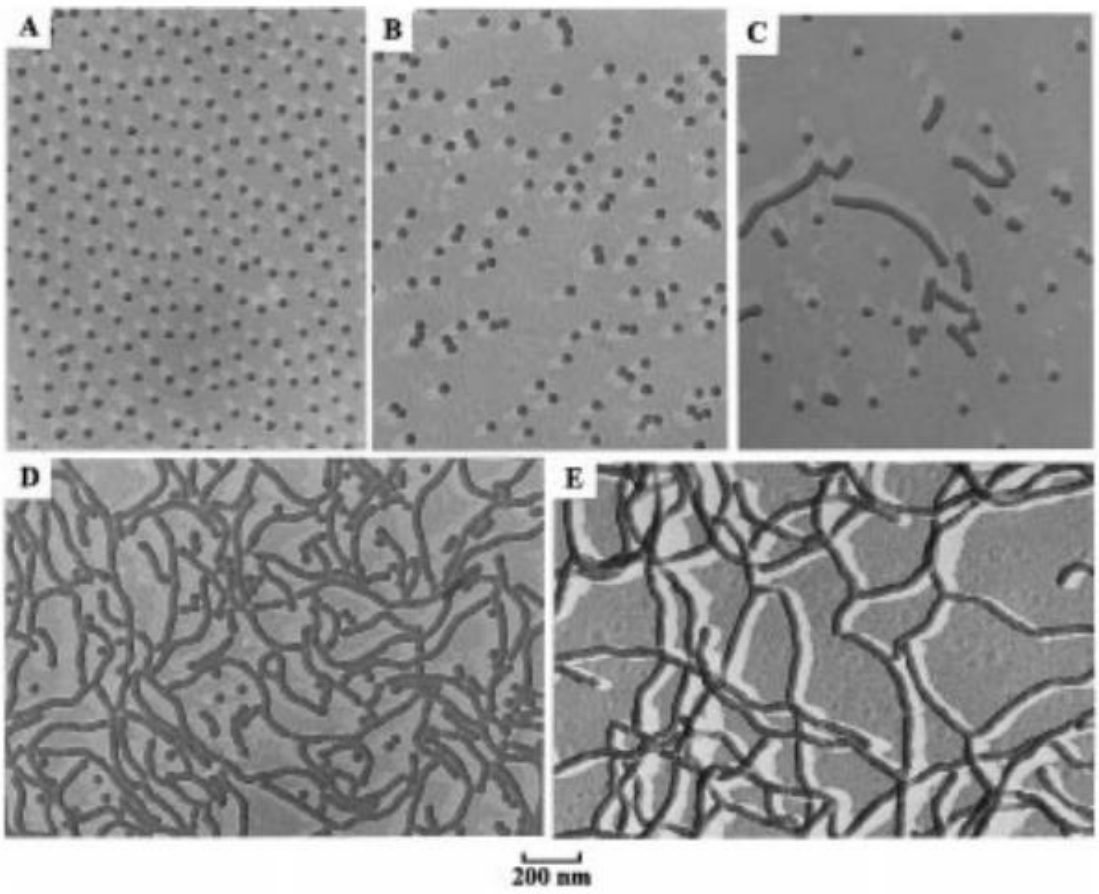

Figure 1-8. Aggregates of PS_{190}-*b*-PAA_{20} in a 94.5/5.5 (w/w) DMF/water mixture to different final copolymer concentration (A) 1.0, (B) 2.0, (C) 2.5, (D) 3.0, (E) 3.5 wt %.[17]

The effect of water content was also reported in the same study (Table 1-1). From left to right, as water content increases, morphology changes from higher-curvature to lower-curvature structure for all polymer concentrations in the range of this study. At a fixed polymer concentration, the aggregation number increases as water content increases,[17] thus nanoparticles of lower-curvature morphology were formed to reduce PS chain stretching.

Table 1-1. Morphologies[a] of PS_{190}-*b*-PAA_{20} at different polymer concentration and water content.[17]

polymer concentration (wt %)	water content in DMF (wt %)				
	5.5	6.5	7.5	8.5	9.5
0.5		S	R, S	R, S	
1.0	S	S	LR	LR	B
1.5	S	S, R	LR, XR	XR, B	
2.0	S	R, S			
2.5	S, R	LR	B		
3.0	R, S				
3.5	LR	B, XR	B	B	

(a) S, spheres; R, rods; LR, long rods; XR, interconnected rods; B, bilayer (vesicles, lamellae, LCM). If two morphologies are listed, the major one is given first.

Block copolymer composition also has an effect on the morphology. In Figure 1-9, by decreasing PAA block length while keeping PS block length constant, morphology of PS-*b*-PAA aggregates changed from spheres to rods, to vesicles and finally to LCMs. It has been observed that PS chain stretching in the core increases as the PAA block length decreases,[18] which makes the entropy of micellization more negative. At some point, the morphology changes to lower-curvature to reduce chain stretching and the entropy

penalty. The effect of PS block length was also investigated empirically and a scaling law was used to show the relationship between spheres' core dimension and block lengths:[19]

$$R_{core} \propto {N_{PS}}^{0.4} {N_{PAA}}^{-0.15} \quad (1\text{-}9)$$

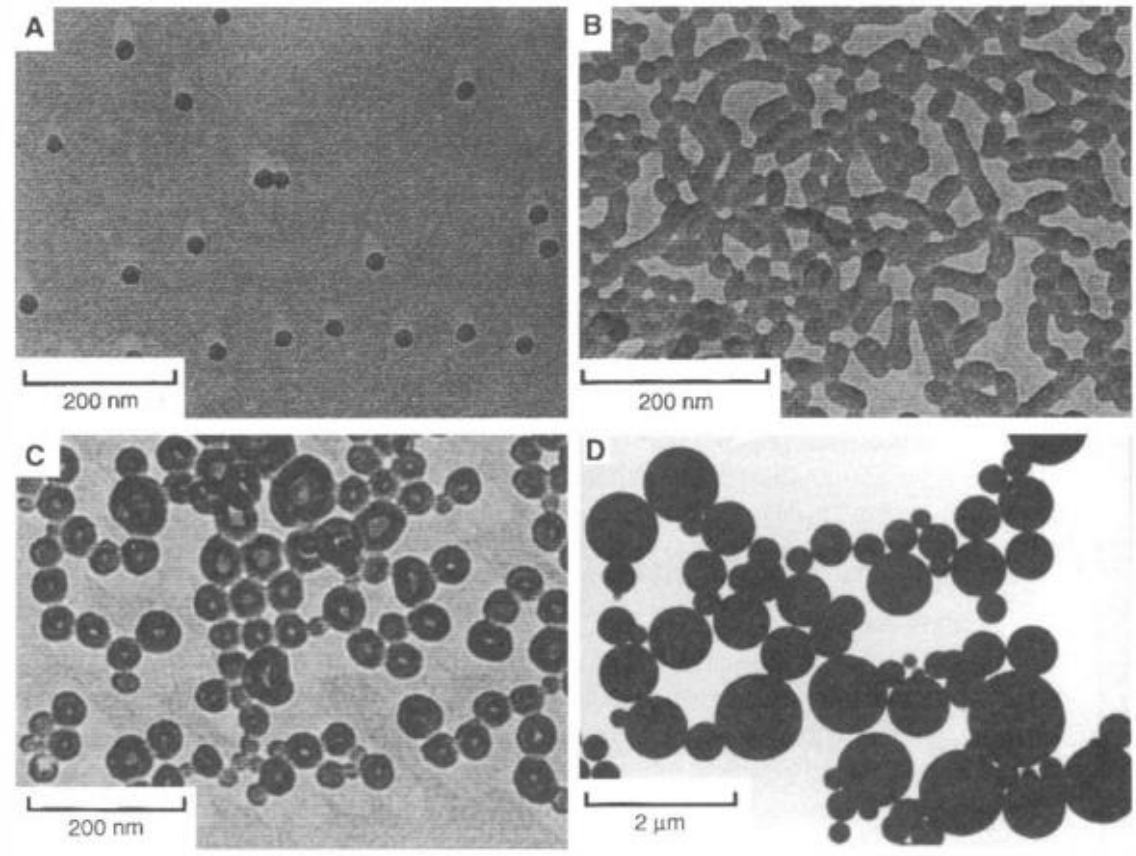

Figure 1-9. Morphologies of "crew-cut" aggregates from PS_{200}-*b*-PAA_{21} (A), PS_{200}-*b*-PAA_{15} (B), PS_{200}-*b*-PAA_{8} (C), PS_{200}-*b*-PAA_{4} (D).[18]

Different types of additives have different effects on nanoparticle morphology of PS-*b*-PAA. PAA is an acid with a pK_a of 4.2. Addition of salt induces electrostatic screening among corona-forming block (polyelectrolytes). As charge along the corona chain decreases, the reduced repulsion between negatively charged coronal chains favours the formation of lower-curvature structures (Figure 1-10). Acid has similar effect but with a different mechanism (Figure 1-11). Protonation of corona-forming chain will

decrease their negative charge and inter-chain repulsion will decrease. However, addition of base enhances the charge density of coronal chains, pushing curvature to become higher (Figure 1-12).

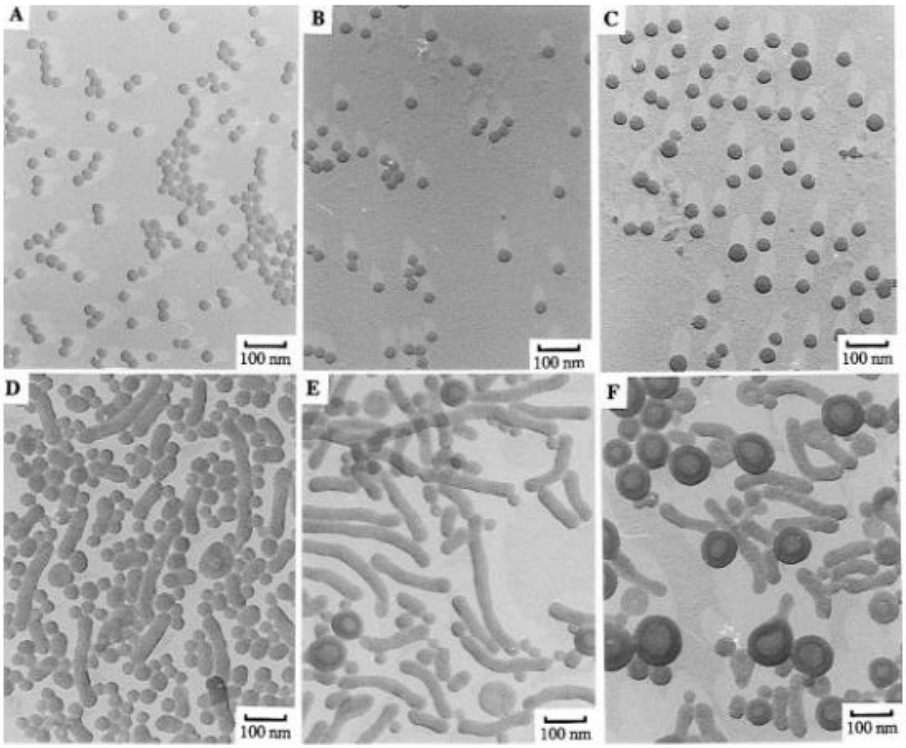

Figure 1-10. Aggregates from PS_{410}-*b*-PAA_{25} without any additive (A) and with added NaCl to different final concentrations: (B) 1.1 mM; (C) 2.1 mM; (D) 3.2 mM; (E) 4.3 mM; (F) 5.3 mM.[20]

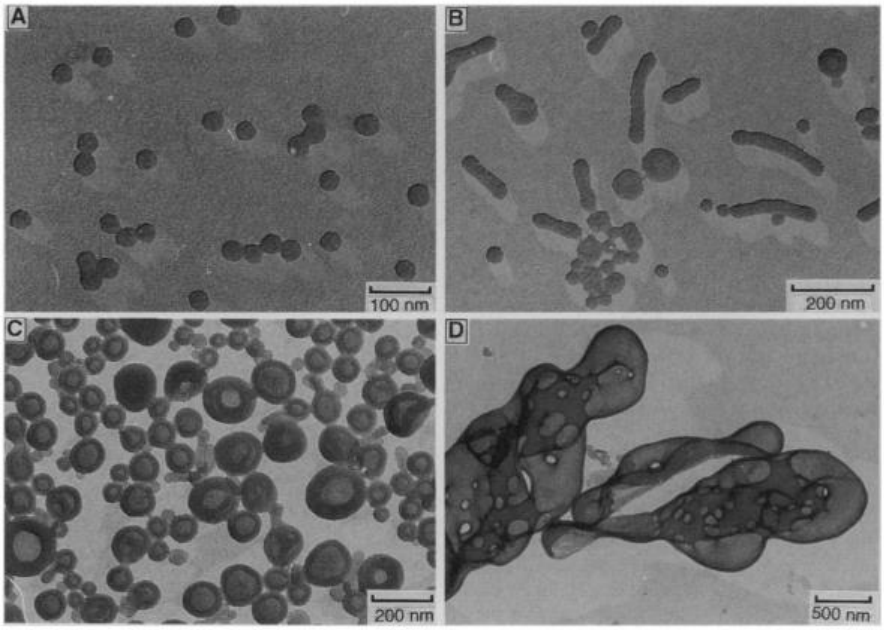

Figure 1-11. Aggregates of PS_{410}-*b*-PAA_{25} formed with various HCl concentrations: (A) 190 μM, (B) 210 μM, (C) 240 μM, and (D) 270 μM.[21]

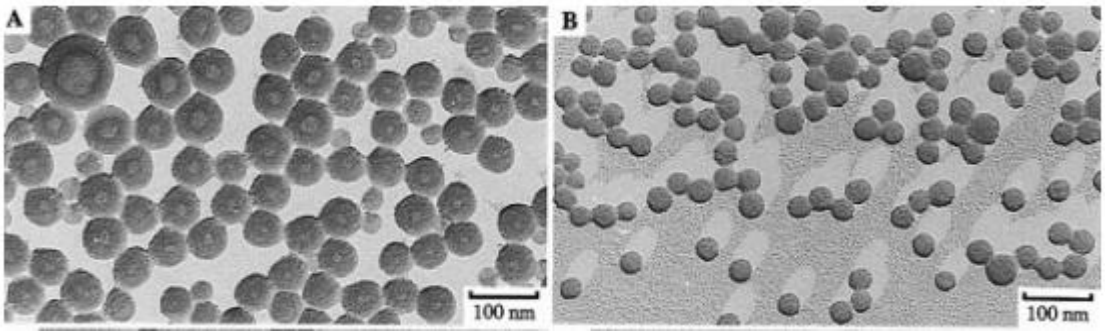

Figure 1-12. Aggregates from PS_{410}-*b*-PAA_{13} without any additive (A) and with 28 μM NaOH (B).[20]

Addition of homopolymer and micellization in different solvents were also studies for PS-*b*-PAA system.[19] Hydrophobic homopolymer can fill the core of nanoparticles, increasing the degree of stretching of the PS block and reducing the PAA content, thus low-curvature structures are formed. Changing solvents changes polymer-solvent interaction and coil volume in the core. Therefore, various morphologies were formed.[22]

1.2.4. Drug Delivery Using Block Copolymer Nanoparticles

Drug delivery is a process to formulate, and transport a pharmaceutical compound in the body as needed to safely achieve its desired therapeutic effect. An ideal drug delivery vehicle must be non-toxic, biocompatible, non-immunogenic, and biodegradable.[23] Drug delivery vehicles include polymeric micelles[24-27] and dendrimers[28, 29], liposomes[30-32], viruses[33, 34], inorganic nanoparticles[35-38] and so on. Block copolymer nanoparticles have been studied extensively as potential drug delivery vehicles because they (1) can be biocompatible and biodegradable, (2) are of tunable size and morphology, (3) are able to load hydrophilic or hydrophobic drugs in the core or shell, (4) can be self-modified to target specific cells or acceptors, (5) can be stimuli-responsive to control release of cargo.

Polycaprolactone (PCL), for example, is a widely-investigated hydrophobic polymer for drug delivery applications. It is very hydrophobic, so it could encapsulate hydrophobic drugs in the core in aqueous solution. There is extensive research in the encapsulation of paclitaxel[39-43], curcumin[44-47], SN-38[48] and other hydrophobic drugs, as well as some hydrophilic drugs[49-52], such as doxorubicin and 5-fluoroucacil. A common block copolymer of PCL and polyethylene oxide, PCL-*b*-PEO's chemical structure is:

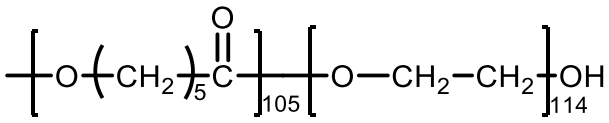

(1-10)

PEO is a biocompatible polymer. It can minimize cell and blood interaction and protein adsorption.[53] Repeat units in PCL are connected by ester bonds, which can be hydrolyzed, making it a biodegradable material. As Figure 1-13 shows, PCL-*b*-PEO can

degrade in hours in acidic environment. Studies were done to demonstrate the biocompatibility of PCL-*b*-PEO.[54]

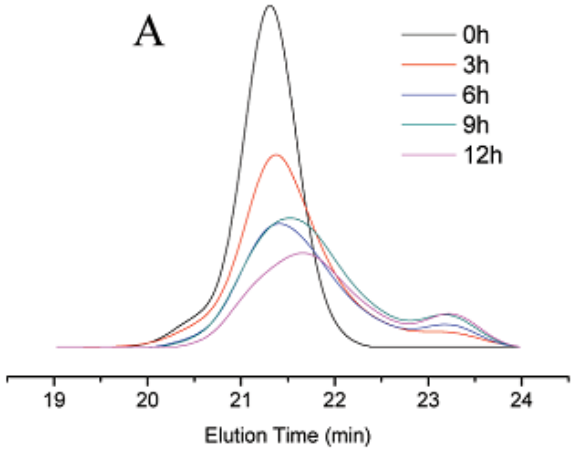

Figure 1-13. GPC trace of hydrolysis of PCL_{62}-*b*-PEO_{45} in HCl (pH = 1) at 25 °C.[55]

1.3. Microfluidics

1.3.1. General Concepts

Microfluidics describes the manipulation of small volumes (10^{-9} to 10^{-18} litres) of fluid in micron-scale channels.[56] Mechanism of fluid, heat and mass transfer in such small length scales is different from that on the macroscale. Since channels are in the order of micrometer the Reynolds number (*Re*) is small and the flow is laminar.[57] Reynolds number is defined as:

$$Re = \frac{\rho v d}{\mu} \qquad (1\text{-}11)$$

In Equation 1-11, ρ is density of the fluid, v is velocity of the fluid, d is the diameter of the channel, and μ is dynamic viscosity of the fluid. When $Re > 4000$, flow is characterized as turbulent flow. The flow pattern is chaotic, with enhanced heat and mass transfer. When $Re < 2300$, the flow type is usually laminar. In laminar flow, viscosity

plays a much more important role than inertia. The absence of inertia in makes the flow instantaneous.[58] Therefore, fluid moves in layers, and heat and mass transfer depends mainly on diffusion. In microfluidics, less volume of reagents is consumed and shorter processing time is required, which is an advantage for synthesis. In a pressure-driven laminar flow, the pressure gradient generates Poiseuille flow (Figure 1-14), which is characterized by a parabolic velocity profile over the cross section of the channel.[59] The center has maximum velocity and the wall has zero velocity.

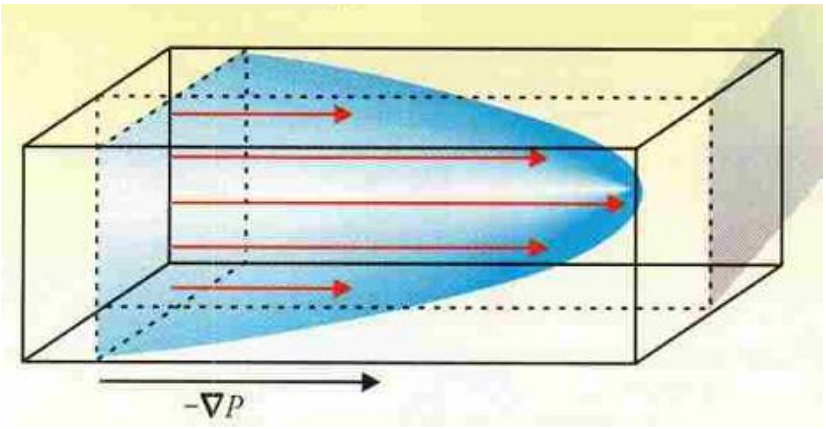

Figure 1-14. Velocity profile in a Poiseuille flow.[60]

Over the last decade, microfluidics has attracted lots of research interest.[61-65] The development of soft lithography technology by Whitesides and coworkers,[66] and the progress in controlling experimental parameters such as temperature and flow rates,[57, 67] makes microfluidic a very convenient tool for various applications. Microfluidics has applications in biochemistry and analytical chemistry.[68, 69] Nanoparticles fabrication using microfluidics is also a significant area. Recent progress includes synthesis of lipid, polymer and metal nanoparticles for drug delivery applications in microfluidic reactors.[70-74] In 2013, the microfluidics market was valued at $1.6 billion.[75]

1.3.2. Gas-Liquid Segmented Microfluidic Reactor

In a typical laminar flow, the fluid flows in layers, thus mass transfer is very slow, resulting in slow mixing. Fast mixing is preferred in chemical and nanoparticle synthesis. Therefore, scientists have worked on increasing mixing in microfluidic reactors. There are generally two ways to solve this problem. One is to design patterned channels, and the other is to use two immiscible phases in reactors.

Stroock et al. has investigated the prediction of flow that has low Re in a closed rectangular channel with a grooved floor (Figure 1-15).[76, 77] They explained that those patterns can induce formation of parallel counter-rotating helices, swapping of flow lines near them,[76] and generating chaotic flow.[77] The chaotic flow increases mixing rate dramatically.

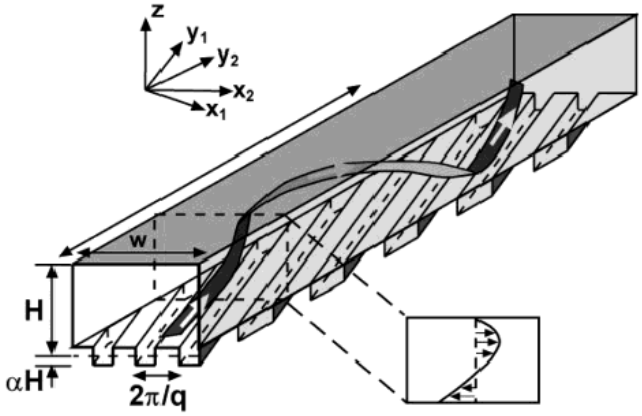

Figure 1-15. Schematic of a microchannel with square grooves on the floor. Helical streamline is indicated with a ribbon.[76]

Microfluidic mixers with similar design, which have staggered herringbone pattern on the bottom, were used for lipid nanoparticles synthesis for drug of siRNA delivery.

It's been demonstrated that the microfluidic mixer offers bottom-up control of size by changing flow ratios of two streams top-down control by changing flow rates.[78-80]

The incorporation of two fluid phases into microfluidic channels was studied by several groups over the last decade.[81-88] There are two types, immiscible liquid-liquid and gas-liquid (Figure 1-16). In liquid-liquid segmented reactors, the liquid that has higher interfacial tension with the channel wall forms droplets and the other is the carrier fluid. In gas-liquid segmented reactors, gas bubbles are the "droplets" and liquid is the carrier fluid.

This thesis focuses on the second type, gas-liquid segmented reactor. The recirculation of gas bubbles induces the formation of rotating vortices in each phase (Figure 1-16B). The rotation of liquid increases mixing greatly.

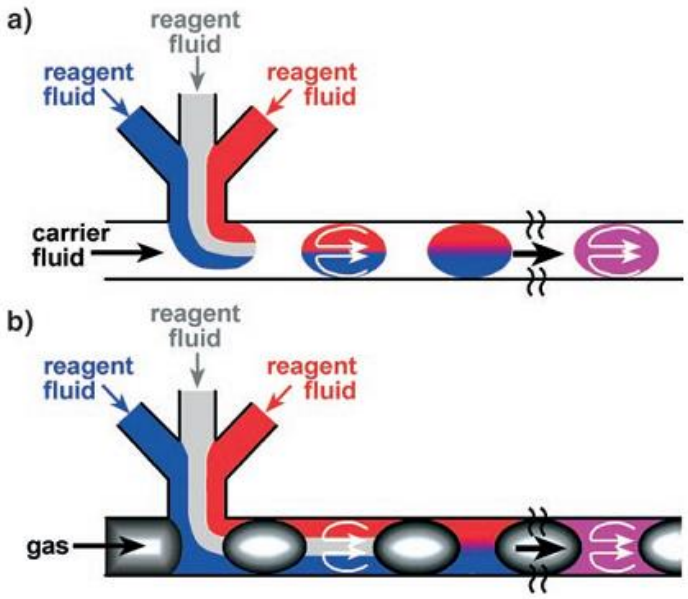

Figure 1-16. Two types of two-phase systems, (A) liquid-liquid, and (B) gas-liquid.[81]

On the gas-liquid segment microfluidic reactor, our group has demonstrated structural and functional control of PS-*b*-PAA and PCL-*b*-PEO nanoparticles. For PS-*b*-

PAA, various morphologies were synthesized at different flow rates, demonstrating top-down control of nanoparticle structure on this reactor.[89, 90] Computational study was done to calculate the on-chip shear rate and it was found that the maximum shear rate (10^4-10^5 s^{-1}) exists at the corners of gas-liquid interfaces, which is significantly higher than the shear rate generated by a stir bar in off-chip preparations.[91] Shear-induced coalescence at low flow rate and shear-induced break-up at high flow rate was a proposed explanation of the morphological changes that were observed.[92] For PCL-*b*-PEO, extensive study on the relationship of morphology and flow rate was done and we discovered that on-chip shear has an effect on crystallinity of the PCL core of the nanoparticles.[93] Furthermore, a hydrophobic anticancer drug, paclitaxel, was loaded in the nanoparticles and improved loading efficiency and slower release were achieved by on-chip preparation.[93]

1.3.3. Microfabrication

At first microfluidic devices were made by silicon or glass. However, silicon is expensive, and the fabrication of glass chips is rather complicated and time consuming. In contrast, soft polymer materials are cheap and easily processed. Polydimethylsiloxane (PDMS) is transparent under UV, allowing for detection in situ.[94] Soft lithography was developed in 90s and has become the major method for microfluidic device fabrication nowadays.

Microfabrication is the process in which gas-liquid segmented microfluidic reactors used in these studies are fabricated. It consists of two main steps, rapid prototyping and replica molding.[95, 96] A photomask (Figure 1-17A) was used in the process to make a master chip (Figure 1-17B) using photolithography, and then the master chip was used to form a negative replica, the PDMS chip that was used in this thesis (Figure 1-17C). A

photomask is printed in a way that where the channels should be is transparent and the background is black in order to block UV light. On a master chip, the channels are raised, while on a PDMS chip the channels are concave. The general process will be discussed as below, but details are also included in experimental in Chapter 2.

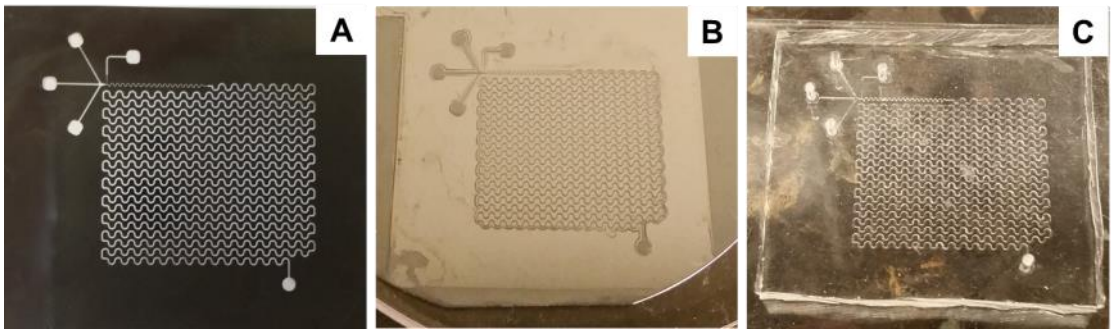

Figure 1-17. Photos of a photomask (A), a master chip (B) and a PDMS chip (C) that was used.

The process of rapid prototyping is shown in Figure 1-18. First, a silicon wafer was cleaned and spin-coated with SU-8. SU-8 is a light-sensitive material acting as a photoresist here. It is cured upon UV irradiation. The spin-coating speed can be controlled to form SU-8 film of certain thickness. In our group a 150 μm-thick film was used. After the wafer is baked to remove solvent, a photomask is placed on the wafer and UV is shone vertically. Following the bake, the wafer is submerged in SU-8 developer which washes away uncured SU-8. In this way, a master chip with pattern of certain height is obtained. A master chip can be used many times for the following step, replica molding, until it is worn out. The cured SU-8 can be washed away using Piranha solution, so the wafer can be used again for spin-coating. However, new wafers are preferred since they have flatter surfaces so the channel height can be better controlled.

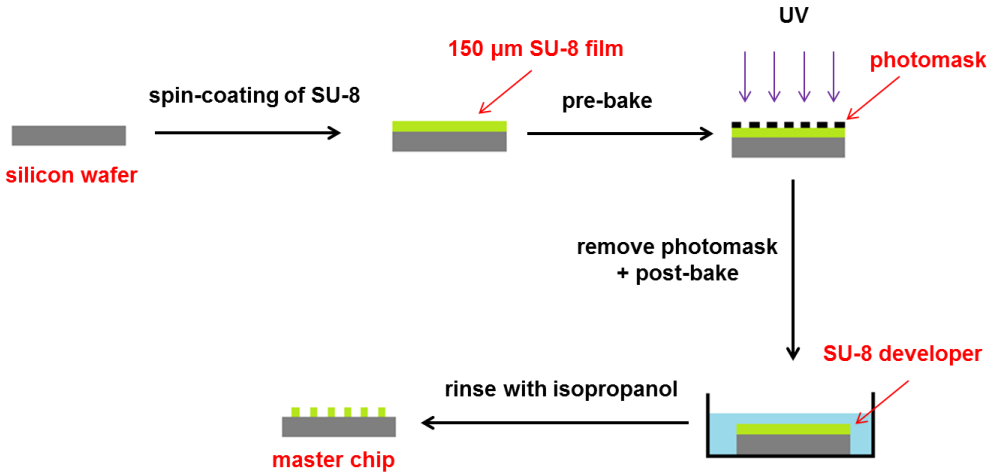

Figure 1-18. Process of rapid prototyping.

Figure 1-19 shows the process of replica molding. PDMS and curing agent is mixed and degassed in vacuum oven, and then the mixture is poured onto a clean master chip in a plastic petri dish, which will be degassed further and cured on a hot plate. After a harden PDMS is formed, it is then carefully cut and peeled out. This forms a negative replica of the master chip used. A substrate which is a thin film of PDMS on a glass slide is made in a same way, except that the mixture is spin-coated onto the glass slide prior to heating. The PDMS chip (channel facing down) is bonded to the substrate (PDMS side up) in a plasma oven. The oxygen plasma oxidizes the surface methyl groups on PDMS to form silanol groups.[97, 98] Oxidized PDMS can be bonded irreversibly to a variety of materials, including itself. We used PDMS here to make sure channels are made of the same materials so that interactions with channel walls at all directions are the same.

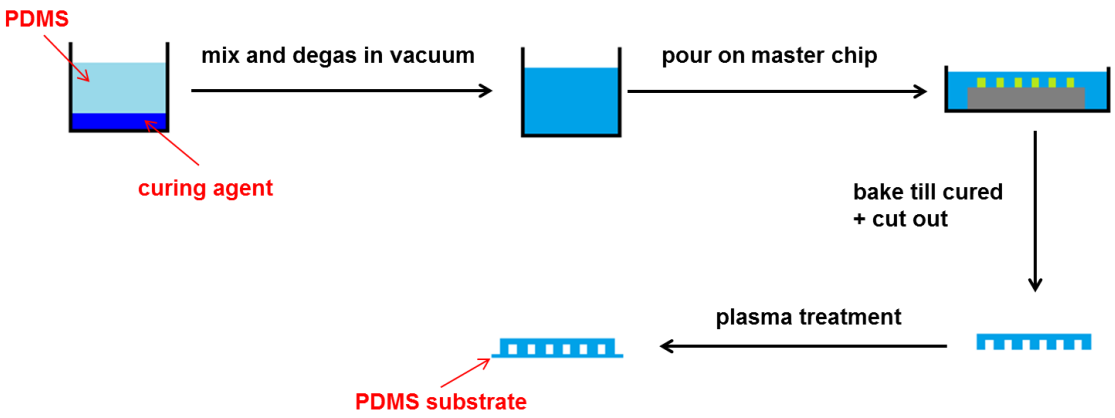

Figure 1-19. Process of replica molding.

1.4. Outline of Thesis

This thesis focuses on the effect of microfluidics on nanoparticles size, morphology, crystallinity, photo response, drug loading and release. The main goal of the thesis is to get better knowledge of the capability of gas-liquid segmented microfluidic reactors for structural and functional control of polymer colloids, and to better understand these effects, in order to apply this microfluidic platform to applications in drug delivery.

Chapter 2 investigates the on-chip self-assembly of a series of photoresponsive copolymers with *o*-nitrobenzyl sidegroups. These copolymers turn hydrophilic from amphiphilic upon UV irradiation. Unique morphologies were obtained on-chip and faster photo-induced decay was demonstrated.

In Chapter 3, the gas-liquid segmented reactor is compared with a commercially available single-phase microfluidic mixer discussed previously. PCL-*b*-PEO with different PCL block lengths was used for this study. Overall, two-phase microfluidic reactor offers flow-variable control of morphology and core crystallinity due to high shear rate, while the effect of flow on morphology and crystallinity in the single-phase reactor are not significant.

Chapter 4 focuses on the self-assembly of P(MCL-*co*-CL)-*b*-PEO nanoparticles with different MCL content. The effect on crystallinity, size, morphology, loading level and release rate is discussed. All MCL-containing copolymers have a tendency to form small, monodispersed spheres with higher loading and slower release. On-chip self-assembly and drug loading behaviour of the copolymers were also studied, i.e. a combination of bottom-up and top-down control. A slower release with neither morphological nor crystallinity effect is demonstrated, and is attributed to better mixing on-chip.

Finally, Chapter 5 discusses general conclusions arising from the thesis work, including recommendations for future work.

1.5. References

1. L. H. Sperling, *Introduction to Physical Polymer Science*. 4 ed.; John Wiley & Sons, Inc.: Hoboken, 2006.

2. V. R. Gowariker, N. V. Viswanathan and J. Sreedhar, *Polymer Science*. 1 ed.; New Age International Limited: New Delhi, 1986.

3. J. M. G. Cowie and V. Arrighi, *Polymers: Chemistry and Physics of Modern Materials*. 3 ed.; CRC Press: Boca Raton, 2007.

4. J. C. E. Carraher, *Polymer Chemistry*. 5 ed.; Eastern Hemisphere Distribution: New York, 2000.

5. C. A. Harper, *Handbook of Plastics, Elastomers, and Composites*. 4 ed.; McGraw-Hill: New York, 2002.

6. I. W. Hamley, *The Physics of Block Copolymers*. Oxford University Press: New York, 1998.

7. J.-F. Gohy, Block Copolymer Micelles. In *Block Copolymers Ii*, V. Abetz, Ed. Springer Berlin Heidelberg: 2005; Vol. 190, pp 65-136.

8. P. W. Atkins and J. De Paula, *Atkins' Physical Chemistry*. Oxford University Press: Oxford; New York, 2014.

9. H. Schott Surfactant Systems: Their Chemistry, Pharmacy and Biology. *Journal of Pharmaceutical Sciences* **1985,** *74*, 1140.

10. P. Alexandridis, J. F. Holzwarth and T. A. Hatton Micellization of Poly(Ethylene Oxide)-Poly(Propylene Oxide)-Poly(Ethylene Oxide) Triblock Copolymers in Aqueous Solutions: Thermodynamics of Copolymer Association. *Macromolecules* **1994,** *27*, 2414.

11. C. Price, E. K. M. Chan, R. H. Mobbs and R. B. Stubbersfield A Thermodynamic Investigation of Micelle Formation by a Polystyrene-B-Polyisoprene Block Copolymer in N-Hexadecane. *European Polymer Journal* **1985,** *21*, 355.

12. H. Shen, L. Zhang and A. Eisenberg Thermodynamics of Crew-Cut Micelle Formation of Polystyrene-B-Poly(Acrylic Acid) Diblock Copolymers in Dmf/H2o Mixtures. *The Journal of Physical Chemistry B* **1997,** *101*, 4697.

13. L. Maibaum, A. R. Dinner and D. Chandler Micelle Formation and the Hydrophobic Effect†. *The Journal of Physical Chemistry B* **2004,** *108*, 6778.

14. L. Zhang and A. Eisenberg Formation of Crew-Cut Aggregates of Various Morphologies from Amphiphilic Block Copolymers in Solution. *Polymers for Advanced Technologies* **1998,** *9,* 677.

15. A. Halperin, M. Tirrell and T. P. Lodge, Tethered Chains in Polymer Microstructures. In *Macromolecules: Synthesis, Order and Advanced Properties*, Springer Berlin Heidelberg: 1992; Vol. 100/1, pp 31-71.

16. N. S. Cameron, M. K. Corbierre and A. Eisenberg 1998 E.W.R. Steacie Award Lecture Asymmetric Amphiphilic Block Copolymers in Solution: A Morphological Wonderland. *Canadian Journal of Chemistry* **1999,** *77,* 1311.

17. L. Zhang and A. Eisenberg Thermodynamic Vs Kinetic Aspects in the Formation and Morphological Transitions of Crew-Cut Aggregates Produced by Self-Assembly of Polystyrene-B-Poly(Acrylic Acid) Block Copolymers in Dilute Solution. *Macromolecules* **1999,** *32,* 2239.

18. L. Zhang and A. Eisenberg Multiple Morphologies of "Crew-Cut" Aggregates of Polystyrene-B-Poly(Acrylic Acid) Block Copolymers. *Science* **1995,** *268,* 1728.

19. L. Zhang and A. Eisenberg Multiple Morphologies and Characteristics of "Crew-Cut" Micelle-Like Aggregates of Polystyrene-B-Poly(Acrylic Acid) Diblock Copolymers in Aqueous Solutions. *Journal of the American Chemical Society* **1996,** *118,* 3168.

20. L. Zhang and A. Eisenberg Morphogenic Effect of Added Ions on Crew-Cut Aggregates of Polystyrene-B-Poly(Acrylic Acid) Block Copolymers in Solutions. *Macromolecules* **1996,** *29,* 8805.

21. L. Zhang, K. Yu and A. Eisenberg Ion-Induced Morphological Changes in "Crew-Cut" Aggregates of Amphiphilic Block Copolymers. *Science* **1996,** *272,* 1777.

22. Y. Yu and A. Eisenberg Control of Morphology through Polymer−Solvent Interactions in Crew-Cut Aggregates of Amphiphilic Block Copolymers. *Journal of the American Chemical Society* **1997,** *119,* 8383.

23. R. C. Scott, D. Crabbe, B. Krynska, R. Ansari and M. F. Kiani Aiming for the Heart: Targeted Delivery of Drugs to Diseased Cardiac Tissue. *Expert Opinion on Drug Delivery* **2008,** *5,* 459.

24. K. Kataoka, A. Harada and Y. Nagasaki Block Copolymer Micelles for Drug Delivery: Design, Characterization and Biological Significance. *Advanced Drug Delivery Reviews* **2001,** *47,* 113.

25. K. Kazunori, K. Glenn S, Y. Masayuki, O. Teruo and S. Yasuhisa Block Copolymer Micelles as Vehicles for Drug Delivery. *Journal of Controlled Release* **1993,** *24,* 119.

26. M.-C. Jones and J.-C. Leroux Polymeric Micelles – a New Generation of Colloidal Drug Carriers. *European Journal of Pharmaceutics and Biopharmaceutics* **1999,** *48*, 101.

27. G. Gaucher, M.-H. Dufresne, V. P. Sant, N. Kang, D. Maysinger and J.-C. Leroux Block Copolymer Micelles: Preparation, Characterization and Application in Drug Delivery. *Journal of Controlled Release* **2005,** *109*, 169.

28. E. R. Gillies and J. M. J. Fréchet Dendrimers and Dendritic Polymers in Drug Delivery. *Drug Discovery Today* **2005,** *10*, 35.

29. Y. Cheng, J. Wang, T. Rao, X. He and T. Xu Pharmaceutical Applications of Dendrimers: Promising Nanocarriers for Drug Delivery. *Front Biosci* **2008,** *13*, 1447.

30. T. M. Allen and P. R. Cullis Liposomal Drug Delivery Systems: From Concept to Clinical Applications. *Advanced Drug Delivery Reviews* **2013,** *65*, 36.

31. S. Li, B. Goins, L. Zhang and A. Bao Novel Multifunctional Theranostic Liposome Drug Delivery System: Construction, Characterization, and Multimodality Mr, near-Infrared Fluorescent, and Nuclear Imaging. *Bioconjugate Chemistry* **2012,** *23*, 1322.

32. K. Maruyama Intracellular Targeting Delivery of Liposomal Drugs to Solid Tumors Based on Epr Effects. *Advanced Drug Delivery Reviews* **2011,** *63*, 161.

33. Q. Zeng, H. Wen, Q. Wen, X. Chen, Y. Wang, W. Xuan, J. Liang and S. Wan Cucumber Mosaic Virus as Drug Delivery Vehicle for Doxorubicin. *Biomaterials* **2013,** *34*, 4632.

34. Y. Ma, R. J. M. Nolte and J. J. L. M. Cornelissen Virus-Based Nanocarriers for Drug Delivery. *Advanced Drug Delivery Reviews* **2012,** *64*, 811.

35. D. Pissuwan, T. Niidome and M. B. Cortie The Forthcoming Applications of Gold Nanoparticles in Drug and Gene Delivery Systems. *Journal of Controlled Release* **2011,** *149*, 65.

36. F. Wang, Y.-C. Wang, S. Dou, M.-H. Xiong, T.-M. Sun and J. Wang Doxorubicin-Tethered Responsive Gold Nanoparticles Facilitate Intracellular Drug Delivery for Overcoming Multidrug Resistance in Cancer Cells. *ACS Nano* **2011,** *5*, 3679.

37. C. E. Probst, P. Zrazhevskiy, V. Bagalkot and X. Gao Quantum Dots as a Platform for Nanoparticle Drug Delivery Vehicle Design. *Advanced Drug Delivery Reviews* **2013,** *65*, 703.

38. C.-L. Huang, C.-C. Huang, F.-D. Mai, C.-L. Yen, S.-H. Tzing, H.-T. Hsieh, Y.-C. Ling and J.-Y. Chang Application of Paramagnetic Graphene Quantum Dots as a Platform for Simultaneous Dual-Modality Bioimaging and Tumor-Targeted Drug Delivery. *Journal of Materials Chemistry B* **2015,** *3*, 651.

39. R. Shi and H. M. Burt Amphiphilic Dextran-Graft-Poly(E-Caprolactone) Films for the Controlled Release of Paclitaxel. *International Journal of Pharmaceutics* **2004,** *271*, 167.

40. S. Dordunoo, J. Jackson, L. Arsenault, A. Oktaba, W. Hunter and H. Burt Taxol Encapsulation in Poly(Ɛ-Caprolactone) Microspheres. *Cancer Chemother. Pharmacol.* **1995,** *36*, 279.

41. Y. Geng and D. E. Discher Visualization of Degradable Worm Micelle Breakdown in Relation to Drug Release. *Polymer* **2006,** *47*, 2519.

42. S. M. Loverde, M. L. Klein and D. E. Discher Nanoparticle Shape Improves Delivery: Rational Coarse Grain Molecular Dynamics (Rcg-Md) of Taxol in Worm-Like Peg-Pcl Micelles. *Advanced Materials* **2012,** *24*, 3823.

43. S. Cai, K. Vijayan, D. Cheng, E. Lima and D. Discher Micelles of Different Morphologies—Advantages of Worm-Like Filomicelles of Peo-Pcl in Paclitaxel Delivery. *Pharm Res* **2007,** *24*, 2099.

44. Z. Ma, A. Haddadi, O. Molavi, A. Lavasanifar, R. Lai and J. Samuel Micelles of Poly(Ethylene Oxide)-B-Poly(E-Caprolactone) as Vehicles for the Solubilization, Stabilization, and Controlled Delivery of Curcumin. *Journal of Biomedical Materials Research Part A* **2008,** *86A*, 300.

45. R. Feng, Z. Song and G. Zhai Preparation and in Vivo Pharmacokinetics of Curcumin-Loaded Pcl-Peg-Pcl Triblock Copolymeric Nanoparticles. *International Journal of Nanomedicine* **2012,** *7*, 4089.

46. J. G. Merrell, S. W. McLaughlin, L. Tie, C. T. Laurencin, A. F. Chen and L. S. Nair Curcumin-Loaded Poly(E-Caprolactone) Nanofibres: Diabetic Wound Dressing with Anti-Oxidant and Anti-Inflammatory Properties. *Clinical and Experimental Pharmacology and Physiology* **2009,** *36*, 1149.

47. C. Mohanty, S. Acharya, A. K. Mohanty, F. Dilnawaz and S. K. Sahoo Curcumin-Encapsulated Mepeg/Pcl Diblock Copolymeric Micelles: A Novel Controlled Delivery Vehicle for Cancer Therapy. *Nanomedicine* **2010,** *5*, 433.

48. G. Quanrong, Z. X. James, H. Min, H. Chuan and C. Jie Sn-38 Loaded Polymeric Micelles to Enhance Cancer Therapy. *Nanotechnology* **2012,** *23*, 205101.

49. Y.-Y. Diao, H.-Y. Li, Y.-H. Fu, M. Han, Y.-L. Hu, H.-L. Jiang, Y. Tsutsumi, Q.-C. Wei, D.-W. Chen and J.-Q. Gao Doxorubicin-Loaded Peg-Pcl Copolymer Micelles Enhance Cytotoxicity and Intracellular Accumulation of Doxorubicin in Adriamycin-Resistant Tumor Cells. *International Journal of Nanomedicine* **2011,** *6*, 1955.

50. X. Gao, B. Wang, X. Wei, W. Rao, F. Ai, F. Zhao, K. Men, B. Yang, X. Liu, M. Huang, M. Gou, Z. Qian, N. Huang and Y. Wei Preparation, Characterization and Application of Star-Shaped Pcl/Peg Micelles for the Delivery of Doxorubicin in the Treatment of Colon Cancer. *International Journal of Nanomedicine* **2013,** *8*, 971.

51. X. Shuai, H. Ai, N. Nasongkla, S. Kim and J. Gao Micellar Carriers Based on Block Copolymers of Poly(E-Caprolactone) and Poly(Ethylene Glycol) for Doxorubicin Delivery. *Journal of Controlled Release* **2004,** *98*, 415.

52. N.-V. Cuong, Y.-L. Li and M.-F. Hsieh Targeted Delivery of Doxorubicin to Human Breast Cancers by Folate-Decorated Star-Shaped Peg-Pcl Micelle. *Journal of Materials Chemistry* **2012,** *22*, 1006.

53. J. Hoffmann, J. Groll, J. Heuts, H. Rong, D. Klee, G. Ziemer, M. Moeller and H. P. Wendel Blood Cell and Plasma Protein Repellent Properties of Star-Peg-Modified Surfaces. *Journal of Biomaterials Science, Polymer Edition* **2006,** *17*, 985.

54. S.-H. Hsu, C.-M. Tang and C.-C. Lin Biocompatibility of Poly(E-Caprolactone)/Poly(Ethylene Glycol) Diblock Copolymers with Nanophase Separation. *Biomaterials* **2004,** *25*, 5593.

55. X. Zhu, M. Fryd, B. D. Tran, M. A. Ilies and B. B. Wayland Modifying the Hydrophilic–Hydrophobic Interface of Peg-B-Pcl to Increase Micelle Stability: Preparation of Peg-B-Pbo-B-Pcl Triblock Copolymers, Micelle Formation, and Hydrolysis Kinetics. *Macromolecules* **2012,** *45*, 660.

56. G. M. Whitesides The Origins and the Future of Microfluidics. *Nature* **2006,** *442*, 368.

57. H. A. Stone, A. D. Stroock and A. Ajdari Engineering Flows in Small Devices. *Annual Review of Fluid Mechanics* **2004,** *36*, 381.

58. E. M. Purcell Life at Low Reynolds Number. *Am. J. Phys* **1977,** *45*, 3.

59. R. F. Probstein, *Physicochemical Hydrodynamics: An Introduction*. John Wiley & Sons: 2005.

60. G. Whitesides and A. Stroock Flexible Methods for Microfluidics. *Phys Today* **2001,** *54*, 42.

61. R. B. Fair, A. Khlystov, T. D. Tailor, V. Ivanov, R. D. Evans, P. B. Griffin, S. Vijay, V. K. Pamula, M. G. Pollack and J. Zhou Chemical and Biological Applications of Digital-Microfluidic Devices. *Design & Test of Computers, IEEE* **2007,** *24*, 10.

62. H. Andersson and A. v. d. Berg Microfabrication and Microfluidics for Tissue Engineering: State of the Art and Future Opportunities. *Lab on a Chip* **2004,** *4*, 98.

63. T. Nisisako, S. Okushima and T. Torii Controlled Formulation of Monodisperse Double Emulsions in a Multiple-Phase Microfluidic System. *Soft Matter* **2005,** *1*, 23.

64. Y. Berdichevsky, J. Khandurina, A. Guttman and Y. H. Lo Uv/Ozone Modification of Poly(Dimethylsiloxane) Microfluidic Channels. *Sensors and Actuators B: Chemical* **2004,** *97*, 402.

65. R. Gorkin, J. Park, J. Siegrist, M. Amasia, B. S. Lee, J.-M. Park, J. Kim, H. Kim, M. Madou and Y.-K. Cho Centrifugal Microfluidics for Biomedical Applications. *Lab on a Chip* **2010,** *10*, 1758.

66. Y. Xia and G. M. Whitesides Soft Lithography. *Annual Review of Materials Science* **1998,** *28*, 153.

67. A. I. K. Lao, T. M. H. Lee, I. M. Hsing and N. Y. Ip Precise Temperature Control of Microfluidic Chamber for Gas and Liquid Phase Reactions. *Sensors and Actuators A: Physical* **2000,** *84*, 11.

68. K. g. Jan, S. Kirat, O. N. Alan, J. Carl, M. Alan and O. B. Peter Development of a Microfluidic Device for Fluorescence Activated Cell Sorting. *Journal of Micromechanics and Microengineering* **2002,** *12*, 486.

69. Y. Sai, M. Yamada, M. Yasuda and M. Seki Continuous Separation of Particles Using a Microfluidic Device Equipped with Flow Rate Control Valves. *Journal of Chromatography A* **2006,** *1127*, 214.

70. L. Capretto, D. Carugo, S. Mazzitelli, C. Nastruzzi and X. Zhang Microfluidic and Lab-on-a-Chip Preparation Routes for Organic Nanoparticles and Vesicular Systems for Nanomedicine Applications. *Advanced Drug Delivery Reviews* **2013,** *65*, 1496.

71. E. Dashtimoghadam, H. Mirzadeh, F. A. Taromi and B. Nyström Microfluidic Self-Assembly of Polymeric Nanoparticles with Tunable Compactness for Controlled Drug Delivery. *Polymer* **2013,** *54*, 4972.

72. J. He, Z. Wei, L. Wang, Z. Tomova, T. Babu, C. Wang, X. Han, J. T. Fourkas and Z. Nie Hydrodynamically Driven Self-Assembly of Giant Vesicles of Metal Nanoparticles for Remote-Controlled Release. *Angewandte Chemie International Edition* **2013,** *52*, 2463.

73. F. S. Majedi, M. M. Hasani-Sadrabadi, S. Hojjati Emami, M. A. Shokrgozar, J. J. VanDersarl, E. Dashtimoghadam, A. Bertsch and P. Renaud Microfluidic Assisted Self-Assembly of Chitosan Based Nanoparticles as Drug Delivery Agents. *Lab on a Chip* **2013,** *13*, 204.

74. A. C. Mendes, E. T. Baran, R. L. Reis and H. S. Azevedo Fabrication of Phospholipid–Xanthan Microcapsules by Combining Microfluidics with Self-Assembly. *Acta Biomaterialia* **2013,** *9*, 6675.

75. L. R. Volpatti and A. K. Yetisen Commercialization of Microfluidic Devices. *Trends in Biotechnology* **2014,** *32*, 347.

76. A. D. Stroock, S. K. Dertinger, G. M. Whitesides and A. Ajdari Patterning Flows Using Grooved Surfaces. *Analytical Chemistry* **2002,** *74*, 5306.

77. A. D. Stroock, S. K. W. Dertinger, A. Ajdari, I. Mezić, H. A. Stone and G. M. Whitesides Chaotic Mixer for Microchannels. *Science* **2002,** *295*, 647.

78. E. Kastner, R. Kaur, D. Lowry, B. Moghaddam, A. Wilkinson and Y. Perrie High-Throughput Manufacturing of Size-Tuned Liposomes by a New Microfluidics Method Using Enhanced Statistical Tools for Characterization. *International Journal of Pharmaceutics* **2014,** *477*, 361.

79. N. M. Belliveau, J. Huft, P. J. C. Lin, S. Chen, A. K. K. Leung, T. J. Leaver, A. W. Wild, J. B. Lee, R. J. Taylor, Y. K. Tam, C. L. Hansen and P. R. Cullis Microfluidic Synthesis of Highly Potent Limit-Size Lipid Nanoparticles for in Vivo Delivery of Sirna. *Mol Ther Nucleic Acids* **2012,** *1*, e37.

80. I. V. Zhigaltsev, N. Belliveau, I. Hafez, A. K. K. Leung, J. Huft, C. Hansen and P. R. Cullis Bottom-up Design and Synthesis of Limit Size Lipid Nanoparticle Systems with Aqueous and Triglyceride Cores Using Millisecond Microfluidic Mixing. *Langmuir* **2012,** *28*, 3633.

81. H. Song, D. L. Chen and R. F. Ismagilov Reactions in Droplets in Microfluidic Channels. *Angewandte Chemie International Edition* **2006,** *45*, 7336.

82. A. Gunther and K. F. Jensen Multiphase Microfluidics: From Flow Characteristics to Chemical and Materials Synthesis. *Lab on a Chip* **2006,** *6*, 1487.

83. A. Gunther, S. A. Khan, M. Thalmann, F. Trachsel and K. F. Jensen Transport and Reaction in Microscale Segmented Gas-Liquid Flow. *Lab on a Chip* **2004,** *4*, 278.

84. H. Song, J. D. Tice and R. F. Ismagilov A Microfluidic System for Controlling Reaction Networks in Time. *Angewandte Chemie* **2003,** *115*, 792.

85. M. R. Bringer, C. J. Gerdts, H. Song, J. D. Tice and R. F. Ismagilov Microfluidic Systems for Chemical Kinetics That Rely on Chaotic Mixing in Droplets. *Philosophical Transactions of the Royal Society of London A: Mathematical, Physical and Engineering Sciences* **2004,** *362*, 1087.

86. Y. Song, J. Hormes and C. S. S. R. Kumar Microfluidic Synthesis of Nanomaterials. *Small* **2008,** *4*, 698.

87. S. A. Khan, A. Günther, M. A. Schmidt and K. F. Jensen Microfluidic Synthesis of Colloidal Silica. *Langmuir* **2004,** *20*, 8604.

88. H. Song, M. R. Bringer, J. D. Tice, C. J. Gerdts and R. F. Ismagilov Experimental Test of Scaling of Mixing by Chaotic Advection in Droplets Moving through Microfluidic Channels. *Applied Physics Letters* **2003,** *83*, 4664.

89. C.-W. Wang, D. Sinton and M. G. Moffitt Morphological Control Via Chemical and Shear Forces in Block Copolymer Self-Assembly in the Lab-on-Chip. *ACS Nano* **2013,** *7*, 1424.

90. C.-W. Wang, A. Bains, D. Sinton and M. G. Moffitt Flow-Directed Assembly of Block Copolymer Vesicles in the Lab-on-a-Chip. *Langmuir* **2012,** *28*, 15756.

91. G. Schabas, C.-W. Wang, A. Oskooei, H. Yusuf, M. G. Moffitt and D. Sinton Formation and Shear-Induced Processing of Quantum Dot Colloidal Assemblies in a Multiphase Microfluidic Chip. *Langmuir* **2008,** *24*, 10596.

92. C.-W. Wang, D. Sinton and M. G. Moffitt Flow-Directed Block Copolymer Micelle Morphologies Via Microfluidic Self-Assembly. *Journal of the American Chemical Society* **2011,** *133*, 18853.

93. A. Bains, Y. Cao and M. G. Moffitt Multiscale Control of Hierarchical Structure in Crystalline Block Copolymer Nanoparticles Using Microfluidics. *Macromolecular Rapid Communications* **2015**, n/a.

94. A. J. DeMello Control and Detection of Chemical Reactions in Microfluidic Systems. *Nature* **2006,** *442*, 394.

95. J. R. Anderson, D. T. Chiu, H. Wu, O. Schueller and G. M. Whitesides Fabrication of Microfluidic Systems in Poly (Dimethylsiloxane). *Electrophoresis* **2000,** *21*, 27.

96. D. C. Duffy, J. C. McDonald, O. J. A. Schueller and G. M. Whitesides Rapid Prototyping of Microfluidic Systems in Poly(Dimethylsiloxane). *Analytical Chemistry* **1998,** *70*, 4974.

97. M. J. Owen and P. J. Smith Plasma Treatment of Polydimethylsiloxane. *Journal of Adhesion Science and Technology* **1994,** *8*, 1063.

98. A. D. Stroock and G. M. Whitesides Components for Integrated Poly (Dimethylsiloxane) Microfluidic Systems. *Electrophoresis* **2002,** *23*, 3461.

Chapter 2.

Microfluidic Synthesis of Photoresponsive Spool-Like Block Copolymer Nanoparticles: Flow-Directed Formation and Light-Triggered Disruption

2.1. Introduction

Amphiphilic block copolymers self-assemble in selective solvents into micellar nanoparticles of various morphologies with a range of diverse applications, from sensors,[2] to medical imaging,[3] to drug delivery.[4-11] For many applications, responsive block copolymer nanoparticles that can be disrupted by controllable external stimuli, such as temperature,[12-14] pH,[15-17] light[18-20] or redox reactions[21-23], are of particular interest. For example, in drug delivery applications, light responsive nanoparticles could be employed to release drug cargo where it is needed by applying light to a specific region of the body and triggering the dissociation of the nanoparticles. A demonstrated synthetic route to such light-responsive block copolymers is to attach chromophores to the hydrophobic block via ester linkages.[24] Upon irradiation, a photolysis reaction leads to cleavage of the chromophores and transformation of ester groups to carboxylic acid groups, thus making the initially hydrophobic block hydrophilic. As a result, the block copolymer loses its amphiphilicity and the associated micellar nanoparticles dissociate, releasing any cargo dissolved in the core. For example, the block copolymer poly(*o*-nitrobenzyl methacrylate)-*b*-poly(ethylene oxide) (PNBM-*b*-PEO) has been shown to produce light-

responsive nanoparticles by virtue of the photocleavable ester linkages along the PNBM block, and results showed that the rate of photoinduced disruption of PNBM-*b*-PEO nanoparticles and concomitant release of encapsulated dye depended on both the hydrophobic block length and irradiation intensity.[25]

Recently, microfluidic systems have been used to synthesize nanostructures.[26-28] Flow within a microfluidic environment can be manipulated to exert significant shear stress during nanofabrication, resulting in the formation of novel nanostructures.[29, 30] Block copolymer nanoparticle morphologies have been conventionally controlled by a variety of "bottom-up" chemical factors, which influence self-assembly by modulating inter- and intramolecular enthalpic and entropic forces.[31-33] In our group, we have shown that when nanoparticles are formed by mixing block copolymer solutions with water in a gas-liquid segmented microfluidic reactor, strong on-chip shear forces provide a non-chemical "top-down" handle on morphologies.[34-39] For example, we have used this microfluidic platform to produce stable, flow-directed nanoparticles of the amorphous block copolymer polystyrene-*b*-poly(acrylic acid) (PS-*b*-PAA), demonstrating that structures formed on-chip are distinct from those formed in the bulk under identical chemical conditions,[36] and also that changes in on-chip flow rate result in different sizes and morphologies of the resulting nanoparticles.[37, 38] More recently, we have applied the same microfluidic reactor to the self-assembly of the biocompatible and semicrystalline block copolymer polycaprolactone-*b*-poly(ethylene oxide) (PCL-*b*-PEO), of particular interest for drug delivery applications, showing that flow rate provides control over structural features on multiple length scales, including not only size and morphology, but also the internal crystallinity of the resulting nanoparticles.[39]

Turning our attention to the on-chip self-assembly of photoresponsive block copolymer materials, we consider the intriguing possibility that microfluidic shear fields might be used to direct not only the size and shape, but also the responsivity of nanoparticles in the presence of light. In this paper, we apply a gas-liquid microfluidic reactor (Figure 2-1) to nanoparticle formation from a series of poly(*o*-nitrobenzyl acrylate)-*b*-polydimethylacrylamide (PNBA-*b*-PDMA, Figure 2-2A) block copolymers with variable lengths of the photoresponsive and hydrophobic PNBA block. In this case, exposure to light triggers ester cleavage along the PNBA block, leading to nanoparticle dissociation. To our knowledge, this work represents the first time photoresponsive block copolymers have been assembled using a high-shear microfluidic device. The various copolymers are found to self-assemble into spherical nanoparticles when water is added by a conventional bulk method but form fascinating spool-like nanoparticles in the microfluidic channels at higher flow rates (Figure 2-2B). These spooled cylinders represent a new block copolymer morphology that is a direct result of PNBA-*b*-PDMA self-assembly in the unique high-shear environment of the microfluidic channels, not observed during our previous work using PS-*b*-PAA and PCL-*b*-PEO. The PNBA nanoparticles possess a soft amorphous core, in contrast to the previously tested materials, which had glassy (PS) or semicrystalline (PCL) cores. Moreover, we demonstrate different light-triggered dissociation kinetics for nanoparticles formed on-chip at different flow rates, which is attributed to the resulting differences in excess free energies (with respect to equilibrium states) of nonergodic nanoparticles formed in the microfluidic channels under different shear conditions.

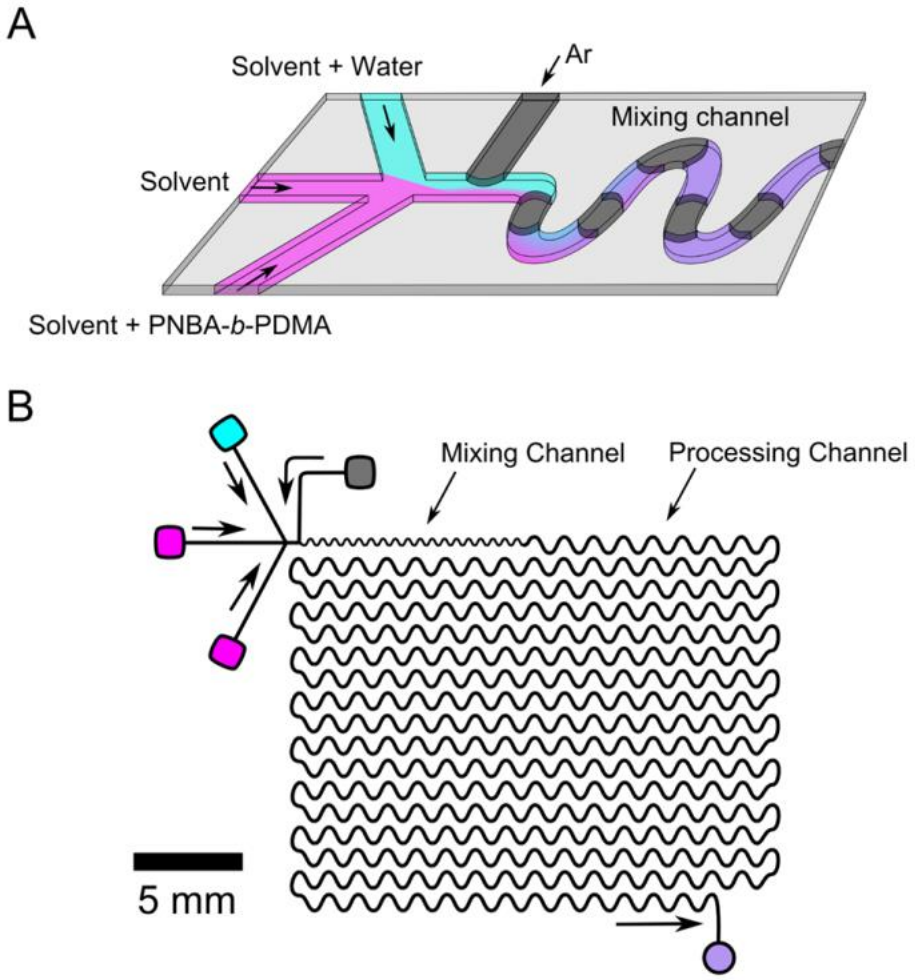

Figure 2-1. (A) Schematic of the microfluidic injector and mixing channel within the gas-liquid segmented reactor. (B) Full chip schematic.

2.2. Experimental

Materials. All the chemicals for block copolymer synthesis were purchased from Sigma Aldrich and used as received. 2, 2'-Azobis(isobutyronitrile) (AIBN) (Aldrich) was recrystallized twice from methanol and used as a thermal initiator. The functional photoresponsive monomer, 2-nitrobenzyl acrylate, was synthesized according to the reported reference.[40] The RAFT agent, 2-(dodecylthiocarbonothioylthio)-2-methylpropionic acid (DMP) was synthesized according to a previously-reported

procedure.[41] 1,4-Dioxane (Fisher Scientific, 99.9%) was used as received without further purification.

Synthesis of Macro-RAFT Agent. DMP (0.365 g, 1 mmol), *N,N'*-dimethylacrylamide (DMA) (7.92 g, 80 mmol), AIBN (0.0162 g, 0.1 mmol) were dissolved in 10 mL of dioxane in a one-neck flask (25 mL). After 20 min of N_2 purging, the homogeneous solution was put into a preheated oil bath at 70 °C for 1 hr. The reaction was quenched in liquid nitrogen and precipitated in a large amount of ethyl ether three times and dried to a constant weight under vacuum. The obtained polymer was characterized by GPC and ^{1}H NMR. From ^{1}H NMR spectrum, the degree of polymerization was determined to be 37.

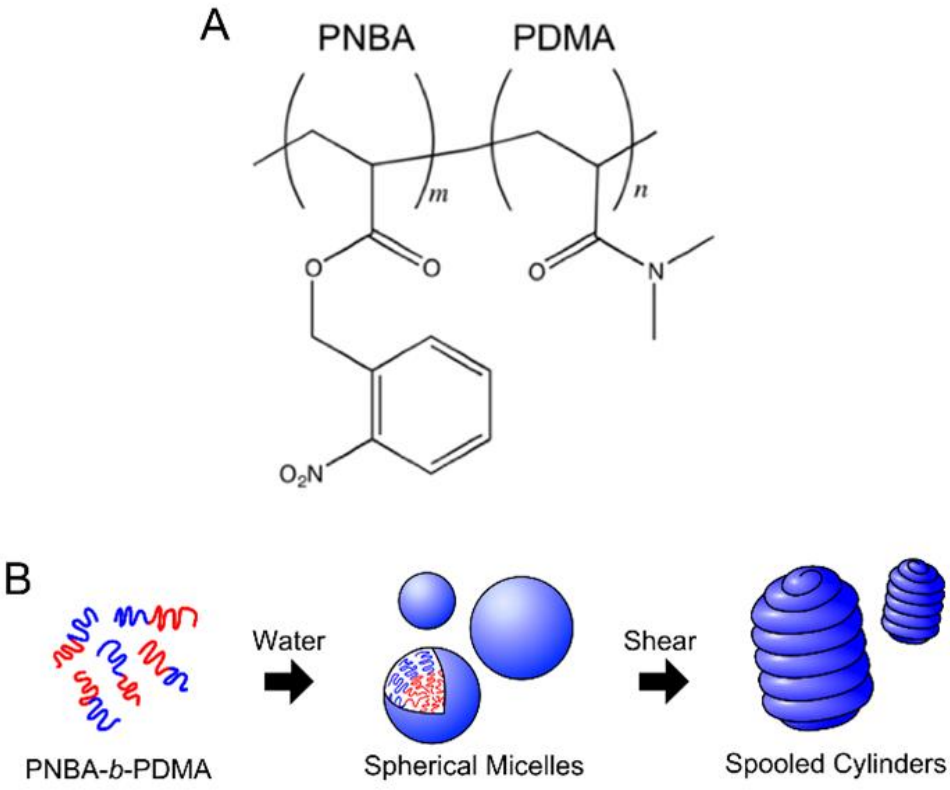

Figure 2-2. (A) Chemical structure of PNBA-*b*-PDMA copolymers. (B) Schematic of nanoparticle formation.

Synthesis of Photoresponsive Block Copolymers. A series of PNBA-*b*-PDMA block copolymers (Figure 2A), which possess the same hydrophilic block length (PDMA) and a hydrophobic block of variable length (PNBA), was synthesized by RAFT polymerization using $PDMA_{37}$-DMP as a macro-RAFT agent. For example, the following procedure was used to synthesize $PNBA_{22}$-*b*-$PDMA_{37}$ (numbers in subscripts indicate number-average degrees of polymerization of the respective blocks): to a one-neck flask (10 mL), $PDMA_{37}$-DMP (0.37 g, 0.1 mmol), 2-nitrobenzyl acrylate (0.828 g, 40 mmol), 1 mL DMF and AIBN (0.008g, 0.05mmol) was added. After 20 min of N_2 purging, the formed solution was placed in a preheated oil bath at 70 °C for 12 hr. The reaction was quenched in liquid nitrogen and purified by precipitation in a large amount of ethyl ether three times and dried under vacuum overnight. The obtained block copolymer was further characterized by GPC and ^{1}H NMR. The composition of the resultant block copolymer was determined to be $PNBA_{22}$-*b*-$PDMA_{37}$. Similarly, by changing the starting molar ratio of $PDMA_{37}$-DMP and 2-nitrobenzyl acrylate, a series of block copolymers with different PNBA chain lengths were obtained (Table 2-1). The three copolymers $PNBA_{22}$-*b*-$PDMA_{37}$, $PNBA_{52}$-*b*-$PDMA_{37}$, $PNBA_{66}$-*b*-$PDMA_{37}$ are designated NBA-22, NBA-52, NBA-66, respectively.

Critical Water Content (cwc) Determination. Static light scattering measurements were carried out to determine the cwc of 0.33 wt % solutions of each copolymer in dioxane. Light scattering experiments were performed on a Brookhaven Instruments photocorrelation spectrometer equipped with a BI-200SM goniometer, a BI-9000AT digital autocorrelator, and a Melles Griot He-Ne Laser (632.8 nm) with a

maximum power output of 75 mW, at a scattering angle of 90° and a temperature of 23 °C.

For each copolymer, a 0.66 wt % solution in dioxane was prepared and allowed to equilibrate overnight. This stock solution was then filtered through 2 x 0.45 μm teflon syringe filters (VWR) in series and then diluted to a final concentration of 0.33 wt % using filtered dioxane (2 x 0.20 μm teflon syringe filter, National Scientific). To initiate nanoparticle formation, filtered deionized water (2 x 0.20 μm Nylon syringe filters, National Scientific) was added in successive 0.03-0.06 g quantities to this solution. After each addition of water, the solution was vortexed to help mixing and then equilibrated for 15 min before the scattered light intensity was measured. From the resulting plots of scattered light intensity vs. water concentration, cwc values were determined by extrapolation of the steep increase in intensity to the baseline. The resulting titration plots and cwc determinations for each copolymer are shown in Figure S2-1; the resulting cwc values for each copolymer are tabulated in Table 2-1 and were used as reference values for selecting water contents for bulk and microfluidic nanoparticle preparations.

Table 2-1. Description of PNBA$_m$-*b*-PDMA$_n$ Copolymers.

Copolymer	*m*	*n*	PDI	cwc / wt %[a]
NBA-22	22	37	1.21	21 ± 1
NBA-52	52	37	1.27	18.5 ± 0.1
NBA-66	66	37	1.26	± 0.1

a) cwc measured for 0.33 wt % copolymer solutions in 1,4-dioxane

Bulk Preparation of PNBA-*b*-PDMA Nanoparticles. As a control experiment for comparison with on-chip nanoparticle formation, nanoparticles of each block copolymer were also formed by the conventional method of dropwise water addition.[42] For these

experiments, deionized water was added dropwise to 3 g of 0.33 wt % copolymer solution in dioxane at a rate of 20 µL every 10 s up to a target water content of cwc + 10 wt % with moderate stirring. The resulting nanoparticles in dioxane/water were designated “unquenched” and were analyzed immediately by TEM. To investigate the effect of organic solvent removal on the nanoparticle morphology, nanoparticles following dropwise water addition were immediately quenched into a 10 × excess (by volume) of deionized water, followed by overnight dialysis (6-8 kD MWCO dialysis membrane, Spectrum Laboratories) against deionized water; the resulting nanoparticles were designated “dialyzed”.

Microfluidic Reactor Fabrication. Negative masters were fabricated on silicon wafers (Silicon Materials) using the negative photoresist SU-8 100 (Microchem). A 150 µm-thick SU-8 film was spin-coated at 2000 rpm onto the silicon wafer and heated at 65 °C for 12 min and then at 95 °C for 50 min. After the wafer was cooled, a photomask was placed directly above and the wafer was exposed to UV light for 100 s. Then, the UV-treated film was heated at 65 °C for 1 min and then 95 °C for 20 min. Finally, the silicon wafer was submerged in SU-8 developer (Microchem) and rinsed with isopropanol until all unexposed photoresist was removed.

Microfluidics chips were fabricated from poly(dimethyl siloxane) (PDMS) using a SYLGARD 184 silicon elastomer kit (Dow Corning). For fabrication of all PDMS chips, the elastomer and curing agent were mixed at a 7:1 ratio and degassed under vacuum. The resulting mixture was poured over a clean negative master chip in a Petri dish and further degassed until all remaining air bubbles were removed. The PDMS was heated at 85 °C until cured (~20 min), and then peeled from the negative master; holes were

punched through the reservoirs of the resulting PDMS chip to allow for the insertion of tubing. A thin PDMS film (substrate layer) was also made on a glass slide by spin-coating a 20:1 elastomer / curing agent mixture followed by curing. The substrate layer was then permanently bonded to the base of the microfluidic reactor (channel layer) after both components were exposed to oxygen plasma for 45 s. The resulting reactor has a set channel depth of 150 μm and consists of a sinusoidal mixing channel 100 μm wide and a sinusoidal processing channel 200 μm wide (Figure 1B).

Flow Delivery and Control. Pressure-driven flow of liquids to the reactor inlet was provided using 1 mL gastight syringes (Hamilton, Reno, NV) mounted on syringe pumps (Harvard Apparatus, Holliston, MA). The microfluidic chip was connected to the liquid syringes via 1/16th-inch (OD) Teflon tubing (Scientific Products and Equipment, ON). Gas flow was introduced to the chip via an Ar tank regulator and a downstream regulator (Johnston Controls) for fine adjustments. The chip was connected to the downstream regulator through a 1/16th-inch (OD) / 100-μm (ID) Teflon tube (Upchurch Scientific, Oak Harbor, WA). The liquid flow rate (Q_{liq}) was programmed via the syringe pumps and the gas flow rate (Q_{gas}) was fine-tuned via the downstream pressure regulator in order to set the nominal total flow rates of 25, 50 and 100 μL/min described in the main text. Due to the compressible nature of the gas and the high gas/liquid interfacial tension, discrepancies arise between the nominal (programmed) and actual values of Q_{gas}, Q_{gas}/Q_{liq}, and the total flow rate (Q_{total}). Therefore, actual gas flow rates were calculated from the frequency of bubble formation and the average volume of gas bubbles, determined from image analysis of the mean lengths of liquid and gas plugs, L_{liq} and L_{gas}, respectively, under a given set of flow conditions. This method of flow calculation has

been previously employed in the context of gas-liquid segmented flow in the microfluidic device.[35, 43] Actual flow parameters pertaining to each microfluidic experiment described in the paper are listed in Table S2-2. For all experiments, the relative gas-to-liquid flow ratio, Q_{gas}/Q_{liq} ~1 and all actual Q_{total} values are within 10 % of nominal values reported in the main text.

Visualization of the gas bubbles and liquid plugs within the microfluidic reactor was achieved using an upright optical microscope (Omax) with a 10 × objective lens. Images were captured using a 2.07 megapixel PupilCam (Ken-A-Vision) and mean lengths of liquid and gas plugs were determined from the images using image analysis software (ImageJ).

Microfluidic Preparation of PNBA-*b*-PDMA Nanoparticles. For microfluidic preparation of nanoparticles (Figure 2-1A), the following three fluid streams were combined to form gas-segmented liquid plugs within the reactor: (1) 0.66 wt % PNBA-*b*-PDMA solution in dioxane, (2) pure dioxane, and (3) water/dioxane mixtures. The relative flow rates of the three liquid streams, Q_{liq1}, Q_{liq2}, Q_{liq3}, respectively, were set such that the combination of the streams yielded steady-state on-chip concentrations of 0.33 wt % copolymer and either 31.0, 28.5, or 28.0 wt % water, corresponding to 10.0 wt % above the cwc for NBA-22, NBA-52, and NBA-66, respectively (Table S2-1). Microfluidic flow conditions were selected and controlled as described in the previous section. Although the mixing of water and dioxane is mildly exothermic in the investigated range of solvent composition (~-125 J/mol),[44] fast heat dissipation and the absence of significant viscous heating means thermal effects on nanoparticle formation will be negligible.

For each copolymer and flow rate, samples were first collected from the chip into empty vials; the resulting nanoparticles in dioxane/water were designated “unquenched” and were analyzed immediately by TEM or used directly for photoirradiation studies. To investigate the effect of organic solvent removal on the nanoparticle morphology, nanoparticles were collected into a vial containing a 10 × excess by volume of deionized water, followed by overnight dialysis (6-8 kD MWCO dialysis membrane, Spectrum Laboratories) against deionized water; the resulting nanoparticles were designated “dialyzed”. Finally, to investigate the off-chip stability of flow-directed morphologies, unquenched nanoparticles were left in the dark under ambient and quiescent conditions and observed by TEM at various times (1 , 3, and 7 days); the resulting nanoparticles were designated “aged”.

Transmission Electron Microscopy. Negatively-stained samples for TEM imaging were prepared by depositing a drop of block copolymer nanoparticle dispersion on a carbon-coated 300-mesh copper TEM grid followed by a drop of 1 wt % uranyl acetate aqueous solution as a negative staining agent. Excess liquid was immediately removed using lens paper, followed by drying of the remaining liquid under ambient conditions. For unstained TEM samples, a drop of dispersion was deposited on the grid and then vitrified by flash freezing in liquid ethane followed by freeze-drying under vacuum. Imaging was performed on a JEOL JEM-1400 transmission electron microscope, operating at an accelerating voltage of 80 kV and equipped with a Gatan Orius SC1000 CCD camera. For each preparation, at least 5 images were taken in different regions of the grid.

For each copolymer and flow condition, morphology and size analysis was performed based on three separate preparations; for each preparation, morphology and size analysis was carried out using at least three images taken in different regions of the grid. Mean dimensions for each condition were determined from a total of at least 450 nanoparticles of each morphology (with the exception of LCM diameters which were sometimes less numerous within the populations; LCM mean diameters were determined from a total of at least 120 nanoparticles). Identified morphologies and mean dimensions for each copolymer and preparation condition are reported in Table 2-2. Averaging and statistical analysis of dimensions from TEM images were conducted using Image J software.

3D TEM tomography was performed on a FEI Tecnai G2 transmission electron microscope, operating at an accelerating voltage of 200 kV and equipped with a high speed AMT 2K side mount CCD camera, and a high resolution FEI Eagle 4K bottom mount CCD camera.

UV/Vis Spectra Measurement. UV/Vis absorbance/transmission measurements were performed on a PE Lambda 1050 spectrometer. Scanning range was 200 nm to 600 nm with a resolution of 0.2 nm. Dialyzed nanoparticles prepared by the bulk method were in deionized water and the constituent copolymer was in dioxane for this measurement. Deionized water and dioxane were used as background references respectively. Figure S2-3 shows the UV/Vis spectrum of NBA-66 and its nanoparticles.

Nanoparticle Photoirradiation and Disruption Kinetics. Photoirradiation of nanoparticle dispersions was performed using an OmniCure S1500 UV/Visible spot curing system with a 320-500 nm filter. Light was transmitted by a liquid light guide at

an intensity of 1000 mW/cm^2 with a distance of ~3.5 cm between the end of the light guide and the nanoparticle dispersion. Prior to irradiation, unquenched NBA-22 dispersions prepared at two different flow rates were diluted with a dioxane/water mixture of 31 wt % water to a copolymer concentration of 0.066 wt % such that the solvent composition remained unchanged upon dilution. 1.25 mL of diluted dispersion was placed in a glass test tube and then irradiated in 5 s intervals under stirring with subsequent cooling to minimize temperature increase. At predetermined cumulative irradiation times, static light scattering intensity and hydrodynamic sizes were measured on the same Brookhaven Instruments photon correlation spectrometer used for cwc measurements, at a scattering angle of 90° and a temperature of 23°C. For determinations of hydrodynamic sizes from dynamic light scattering (DLS) data, refractive index and dynamic viscosity values of 1.40 and 1.18 cP, respectively, were employed; these values for the mixed solvent system were calculated using a method described previously.[45] At cumulative irradiation times of 35 s, 65 s, 95 s, 215 s and 410 s, aliquots of sample were also extracted for TEM imaging. Each photocleaving experiment, including cumulative irradiation time, cooling time, and measurement time, took ~6 hrs. Therefore, in order to distinguish light-triggered dissociation from time-dependent dissociation, control experiments were carried out in which both investigated nanoparticle samples were held at 25 °C for 6 hrs without irradiation, and light scattering intensity was measured every 30 min (Figure S2-4). Reported light scattering intensities are mean values from three separate nanoparticle preparations while reported hydrodynamic sizes are mean values from three measurements of one nanoparticle preparation.

2.3. Results and Discussion

2.3.1. Effect of Flow Rate on Nanoparticle Structure.

Figure 2-3 shows TEM images with negative staining of unquenched NBA-22, NBA-52 and NBA-66 nanoparticles prepared using the bulk method of dropwise water addition, and also using the microfluidic reactor at various flow rates under identical chemical conditions (Figure 2-3). Table 2-2 lists the shape and mean dimensions of shapes observed during these experiments. In the negative stained images, lighter contrast regions correspond to the hydrophobic PNBA cores of the nanoparticles, due to high-electron density uranyl acetate localized in the PDMA coronae. The role of the variable shear environment of the microfluidic multiphase reactor is directly observed through various nanoparticle morphologies. Nanoparticles formed by the conventional bulk method result in a collection of largely monodisperse small spheres, of ~30 nm mean diameter. These spherical nanoparticles are observed in all three bulk prepared solutions: NBA-22, NBA-52 and NBA-62 (Figure 2-3, A, E and I). On-chip nanoparticle formation at the lowest investigated flow rate (25 μL/min, Figure 2-3, B, F, and J) resulted in three distinct nanoparticle types: small spheres, large spheres and cylinders. TEM images without negative staining were used to determine that the larger spheres do not have a low-density center and so they are not vesicles; since they are significantly larger than the ~30 nm spheres, these large spheres are referred to as large compound micelles (LCMs), in keeping with Zhang et al. nomenclature.[42] The LCMs and cylinders represent morphologies formed on-chip that were not observed in dispersions prepared in the bulk. The cylinders were of similar thickness to the small spheres, and were observed with a range of lengths between ~50 nm and ~300 nm. Most of the cylinders are linear with

varying degrees of entanglement on the grid, but a few appear as small closed hoops. In addition to cylinders, large compound micelles were observed in the NBA-52 and NBA-66 cases. At a higher flow rate of 50 μL/min, four distinct nanoparticle geometries are observed: ~30 nm spheres, large compound micelles, cylinders, and what we have named spooled cylinders (50 μL/min, Figure 3, C, G and K). From the two-dimensional TEM images, the spooled cylinders resemble close-packed arrays of many straight and bent cylinders, although as discussed below there is evidence that these two-dimensional projections are due to a three-dimensional winding of long cylinders. Although this winding of cylinders sometimes forms what appear to be regular helical structures, the result is often irregular (Figure 2-3D, inset), resembling more a spool of thread than a neat coil of rope. When the flow rate was increased to 100 μL/min, small spheres, LCMs, cylinders and spooled cylinders were observed for all copolymers (Figure 2-3, D, H and L). In the case of NBA-66 nanoparticles, the spooled cylinders appear compressed (flattened). The majority of spooled cylinders formed at 50 μL/min (Figure 2-3, C, G, and K) and at 100 μL/min in NBA-22 and NBA-52 cases (Figure 2-3, D and H) resemble cocoons with approximate ellipsoidal or triangular shape and a long axis lying parallel to the grid surface. In contrast, most of the spooled cylinder nanoparticles observed from NBA-66 at 100 μL/min appear as roughly circular features with an internal spiral structure (Figure 2-3L, inset). We note that the seemingly compressed, spiral structures could be explained by cocoon-like aggregates oriented with long axes perpendicular to the grid surface, although 3D TEM tomography of these nanoparticles (Figure S2-15) indicates their heights are significantly less than their cross-sectional diameter, suggesting that their long axis has been compressed either by deposition on the substrate

or by shear processing at high flow rate. Still other circular aggregates formed by NBA-66 at 100 μL/min appear hollow, resembling rings, or possess an internal structure of two concentric rings (Figure 2-3L). These could be vesicles or else are additional features arising from the collapse or compression of spooled cylinders at the higher flow rate.

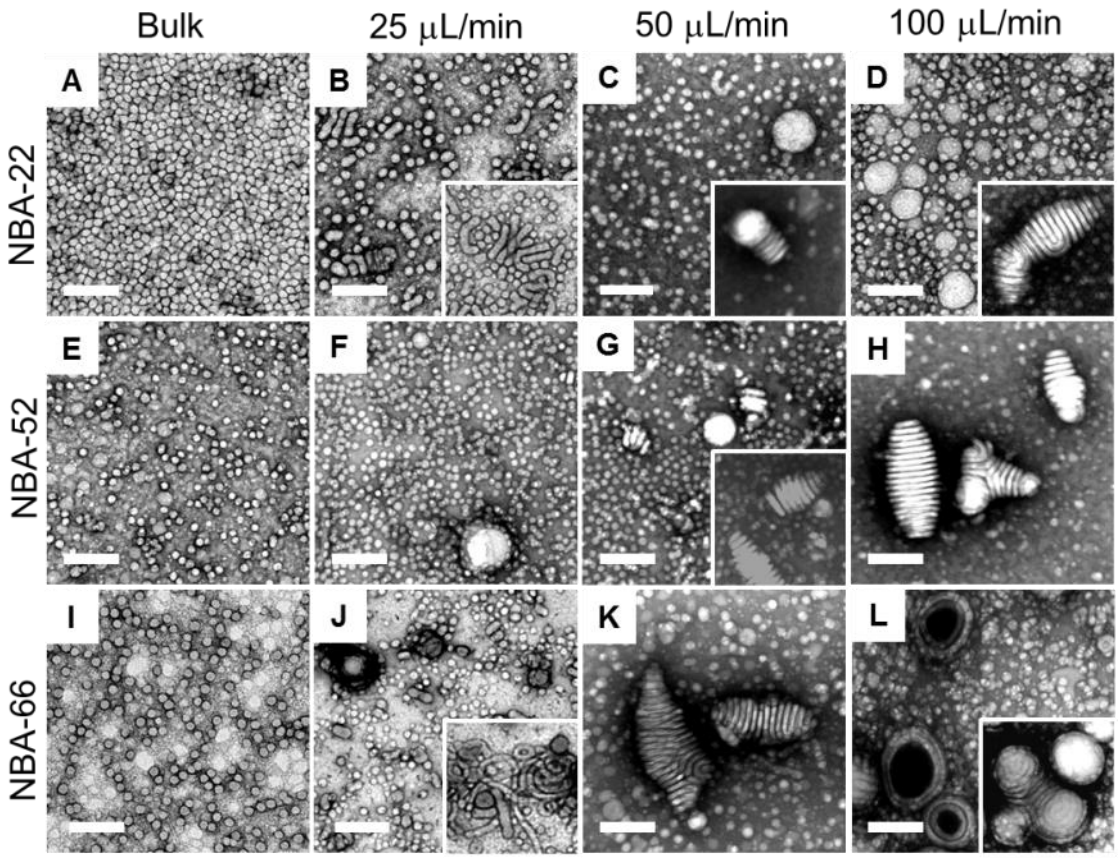

Figure 2-3. Effect of flow rate on the structure of unquenched NBA-22, NBA-52 and NBA-66 nanoparticles, as determined through TEM imaging. Nanoparticles formed in the bulk are included for comparison. Insets show features imaged in a different region of the same sample, or on a different sample prepared under identical conditions. Scale bars are 200 nm; main images and insets share the same scale bar.

Table 2-2. Morphologies[a] and Mean Dimensions[b] for Unquenched PNBA-*b*-PDMA Nanoparticles Prepared in the Microfluidic Reactor at Various Flow Rates.

Sample	bulk	25 μL/min	50 μL/min	100 μL/min
NBA-22	S (30 ± 1 nm)	S (29 ± 1 nm) C (24 ± 2 nm)	S (28 ± 2 nm) C (20 ± 2 nm) LCM (70 ± 10 nm) SC (17 ± 3 nm)	S (29 ± 1 nm) C (21 ± 3 nm) LCM (80 ± 10 nm) SC (18 ± 1 nm)
NBA-52	S (27 ± 1 nm)	S (24 ± 1 nm) LCM (70 ± 10 nm)	S (26 ± 1 nm) C (20 ± 2 nm) LCM (80 ± 10 nm) SC (18 ± 1 nm)	S (26 ± 1 nm) C (16 ± 1 nm) LCM (80 ± 10 nm) SC (16 ± 1 nm)
NBA-66	S (30 ± 1 nm)	S (28 ± 3 nm) C (23 ± 4 nm) LCM (70 ± 10 nm)	S (30 ± 1 nm) C (22 ± 3 nm) LCM (80 ± 10 nm) SC (18 ± 1 nm)	S (31 ± 2 nm) C (27 ± 3 nm) LCM (80 ± 10 nm) SC (23 ± 4 nm)

a) Morphologies are indicated as S (spheres), C (cylinders), LCM (large compound micelles), or SC (spooled cylinders).

b) Numbers refer to sphere or LCM diameters and cylinder or spooled cylinder widths. Reported errors for microfluidic-prepared nanoparticles are standard deviations of three separate preparations. Reported errors for bulk-prepared nanoparticles are standard deviations of mean values from three images of a single preparation.

2.3.2. Effect of PNBA Block Length on Spooled Cylinder Morphology.

Figure 2-3 and statistical analysis of the associated TEM data also provides insight into the relationship between PNBA block length and nanoparticle morphology and frequency. One key difference between on-chip nanoparticle formation for the different PNBA block lengths is that for the two higher PNBA block lengths, NBA-52 and NBA-66, the spooled cylinders are a prominent morphology starting at a flow rate of 50 μL/min, with higher frequency for the longer PNBA block length: ~1 and ~3 spooled cylinders per 100 nanoparticles were found for NBA-52 and NBA-66, respectively (Figure 2-3, G and K). However, for the NBA-22 sample, spooled cylinders appeared only very

infrequently at 50 μL/min (~2 spooled cylinders per 1000 nanoparticles, Figure 2-3C, inset) but increased in frequency when the flow rate increased to 100 μL/min (~1 spooled cylinders per 100 nanoparticles, Figure 2-3D). In the context of a proposed mechanism for cylinder spooling discussed below, the more hydrophobic and stickier surfaces of NBA-52 and NBA-66 nanoparticles arising from their longer hydrophobic blocks compared to NBA-22 nanoparticles might explain this trend. An additional effect of PNBA block length is the observed compression of NBA-66 spooled cylinders at the highest flow rate (Figure 2-3L), which was not observed for the NBA-22 or NBA-52 copolymers (Figure 2-3, D and H) as discussed above.

2.3.3. Probing Spooled Cylinder Morphology Using 2D and 3D TEM.

In Figure 2-4, further insight is gained regarding the morphology of the spooled cylinders. In some regions of the grid, the ends of these unusual structures are bent upwards, affording an end-on view of the nanoparticles and providing some insight into their three-dimensional structure (Figure 2-4, A and B). In this example, TEM imaging suggests the cylindrical packing originates from a single long cylinder spiraling from the end of the aggregate. In other cases, it was found that these coiled cylinders can "unwind", leaving only a thread in their wake (Figure 2-4C). 3D imaging from TEM tomography (Figure 2-5) of a triangular-shaped spooled cylinder of NBA-66 formed at 50 μL/min clearly shows the "corkscrew" conformation of spiraling cylinders at two different ends of the nanoparticle (Figure 2-5, B and C, white arrows), as well as an encapsulated LCM (Figure 2-5, B and C, dashed circles). These spooled cylinders are very different from other reported copolymer structures. In various works, Eisenberg and coworkers describe aggregate superstructures consisting of building blocks of cylindrical

micelles, termed “hexagonally-packed hollow hoops”[46] that in some cases have similar two-dimensional projections to our spooled cylinders. However, the relatively disordered combination of straight and bent cylindrical structures of our samples within many of the two-dimensional projections (Figure 2-3D, inset), as well as the spiral ends observed at the nanoparticle poles (Figure 2-5, B and C), are not consistent with those reported morphologies. Other works have produced helical nanostructures,[47, 48] but none that resemble the unique spooled cylinder morphology observed in this work.

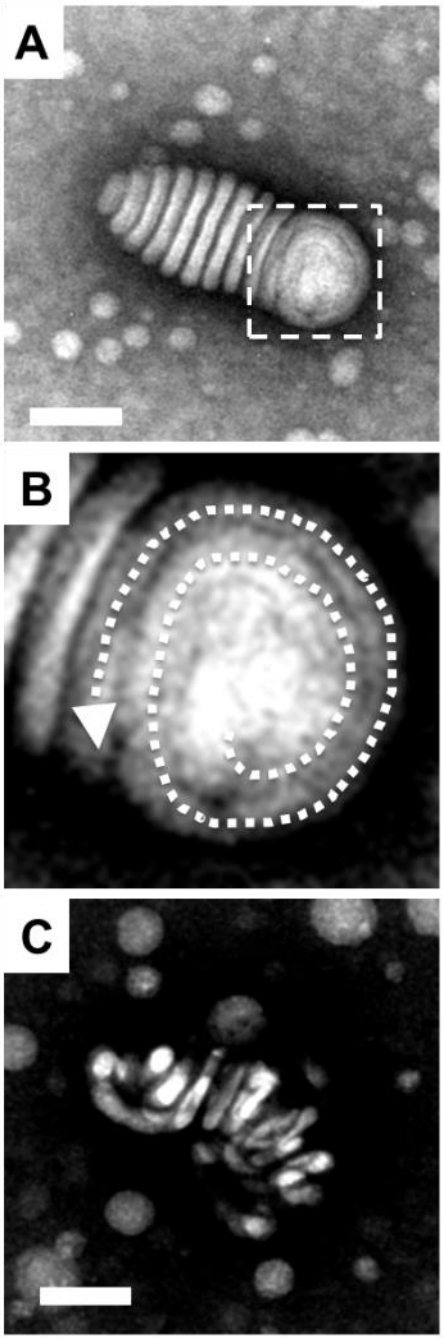

Figure 2-4. Determining the structure of an unquenched NBA-22 spooled cylinder using TEM imaging. (A) Spooled cylinder showing end-on view of spiraling cylinder. (B) Enlarged view of the spooled cylinder shown in (A). (C) Uncoiled spooled cylinder. Scale bars are 100 nm.

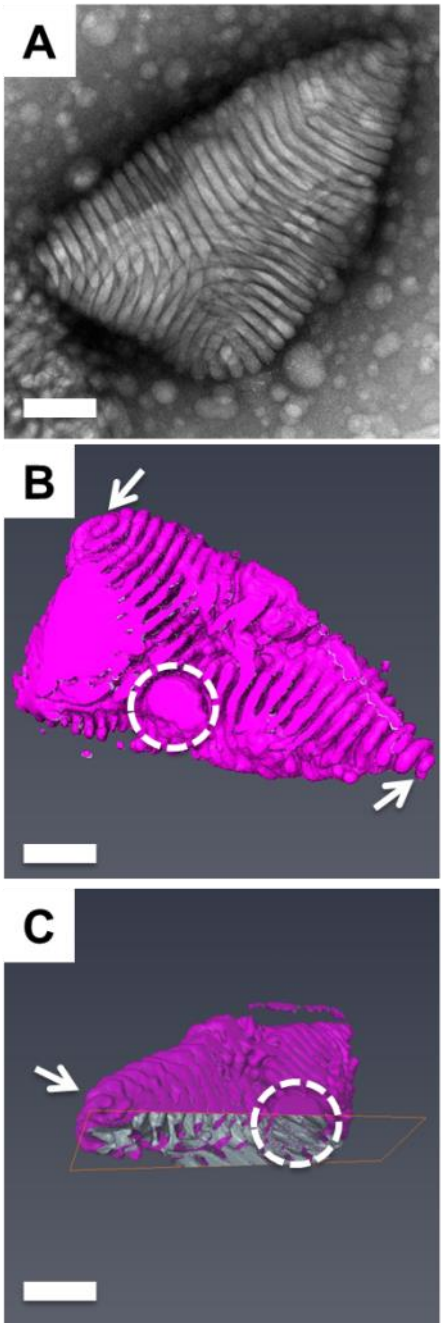

Figure 2-5. 2D TEM image of a triangular-shaped spooled cylinder of NBA-66 formed in the microfluidic reactor at 50μL/min (A) and 3D TEM tomography images of the same nanoparticle taken from two different directions (B and C); arrows in B and C show the striated structure originating from a spiraling cylinder or cylinders at two different ends of the nanoparticle, and dashed circles indicate encapsulated LCM sphere. Scale bars are 100 nm.

2.3.4. Discussion of Spooled Cylinder Formation.

As reported previously,[36] flow-directed nanoparticle morphologies within the two-phase microfluidic reactor are explained by nanoparticle exposure to localized high-shear "hot spots" within the processing channel, following initial nanoparticle formation triggered by fast (~1 s) water mixing within the mixing channel (Figure 2-1B).

The recirculating flow within the two-phase gas-segmented microfluidic reactor produced these localized high-shear hot spots in the corner regions where the liquid plug contacts the liquid film. In our previous work, simulations on a similar system performed using a computational fluid dynamics model indicated a high-vorticity flow much closer to simple shear flow than to elongational flow.[33,49] Chaotic advection during recirculation creates a nonuniform shear, leading to a mixing regime conducive to shear-induced collision-coalescence events.

Since the PNBA core-forming block is noncrystalline, the flow-induced crystallization effects discussed previously in connection with on-chip nanoparticle formation from PCL-*b*-PEO copolymers are not operative here.[39] We note that flow-directed long cylinders have been previously prepared within this microfluidic reactor from other block copolymers, including PS-*b*-PAA[36-38] and PCL-*b*-PEO,[39] although spooled cylinders were not observed to form from either of those materials at any flow rate. We point out that unlike the current block copolymer, which possesses an amorphous and relatively low-T_g (~25 °C) core-forming block (PNBA),[50] the nanoparticle cores from previously-investigated copolymers were either semicrystalline (PCL) or glassy (PS). Based on the bulk nanoparticle preparation experiment, we conclude that the equilibrium morphology of PNBA-*b*-PDMA nanoparticles under the

current chemical conditions are spheres with mean diameter of 30 nm (Figure 2-3, A, E and I). Due to expected fast equilibration of solvent-swollen nanoparticles upon on-chip mixing, supported by previous work,[35] and so similar small spheres should form in the mixing channel before significant exposure to high shear in the processing channel. As these initial small spheres circulate through the hot spots, the localized high shear rates in these regions (10^4-10^5 s^{-1}) describe Péclet numbers in which shear effects will strongly determine the number of collision-coalescence events, leading to larger nonergodic nanoparticles (LCMs, Scheme 2-1) with aggregation numbers increasing with flow rate.[36] Due to kinetic barriers to global equilibration, the resulting shear-induced aggregates will then relax via chain rearrangements to their local free energy minima following microphase separation principles, forming cylinders and LCMs at 25 μL/min (Figure 2-3, B, F and J), 50 μL/min (Figure 2-3, C, G and K) and 100 μL/min (Figure 2-3, D, H and L). According to the above shear-induced coalescence mechanism, described previously for PS-*b*-PAA[36-38] and PCL-*b*-PEO[39] nanoparticle formation within this reactor, the primary role of shear is to increase aggregation numbers, whereas it is chemical forces that direct subsequent morphological transformations via intraparticle chain diffusion and associated conformational changes. However, it appears unlikely that the unusual spooled cylinders are either thermodynamic or kinetic products of chemical forces alone, since to our knowledge similar morphologies have not been previously produced via conventional block copolymer nanoparticle formation in bulk solvent environments. We therefore propose that complex flow fields associated with the counter-rotating vortices within the liquid plugs of the two-phase reactor[34] direct the spooling of long cylinders as they progress through the processing channel. As a cylinder transits high-shear hot-spots at

sufficiently high flow rate, elongated cylinders are driven to coil into themselves. The presence of LCMs attached to spooled cylinders, as seen in Figure 2-5, suggest these structures may play a role in this spooling process, perhaps as an anchor around which spooling occurs. While our data suggest shear as a primary driver of spooled cylinder formation (Scheme 2-1), the exact mechanism through which spooled cylinders are formed is unclear.

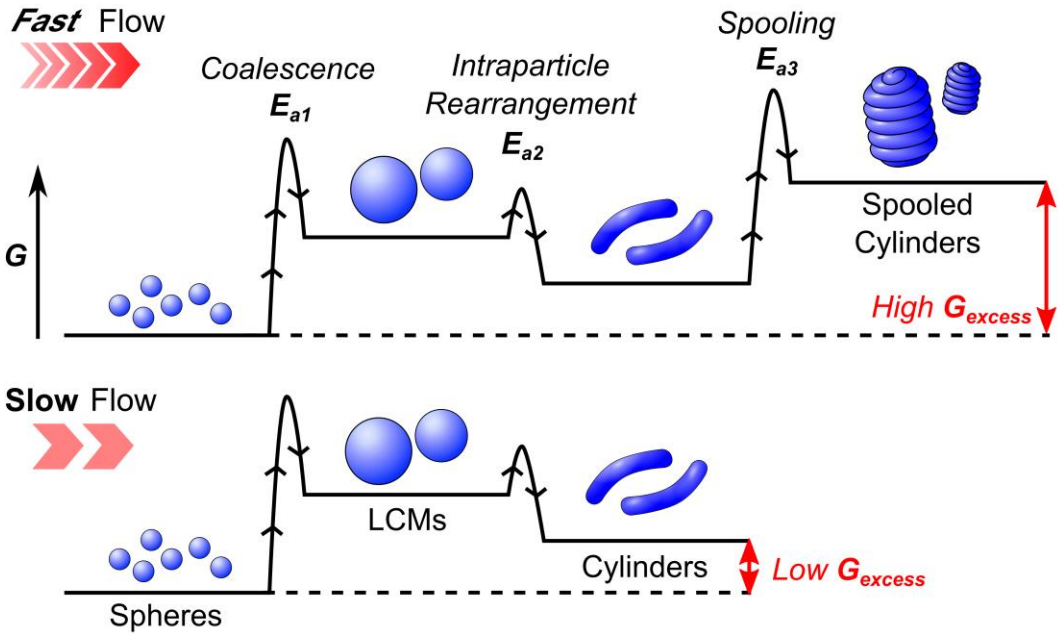

Scheme 2-1. Energy diagram showing the dependence of flow rate on the shear-induced formation and excess free energies of nanoparticles formed in the microfluidic reactor.

2.3.5. Effect of Dialysis on Nanoparticle Structure.

Another consequence of the low-T_g cores of flow-directed nanoparticles formed from PNBA-*b*-PDMA is their lack of morphological stability upon transfer into pure water. This is in contrast to flow-directed colloidal structures formed from PS-*b*-PAA and PCL-*b*-PEO, which can be kinetically trapped by sudden transfer of the DMF/water solutions into a large excess of pure water followed by dialysis to remove residual DMF.

Such kinetic trapping of PS-*b*-PAA[36-38] and PCL-*b*-PEO[39] nanoparticles is explained by the fast expulsion of solvent from the cores triggered by quenching into pure water, resulting in vitrification of PS or increased crystallization of PCL, in both cases leading to rigid and stable nanoparticles "frozen" in their initial flow-directed states. PNBA cores, on the other hand, are neither glassy nor crystalline following removal of solvent;[50] the dynamic block copolymer chains are therefore capable of responding to the sudden change in solvent environment, which under quiescent conditions effectively "erases" the flow-directed morphologies. Figure 2-6 shows TEM images with negative staining of the dialyzed NBA-22 nanoparticles prepared by quenching and dialysis of the unquenched nanoparticles shown in Figure 2-3, A-D.In the on-chip samples, none of the flow-directed nanoparticle morphologies are observed at any flow rate (Figure 2-6, B-D), and all show populations of low-polydispersity spheres similar to those formed by the bulk method (Figure 2-6A), indicating nearly complete relaxation of nonequilibrium structures to the equilibrium morphology of spheres. We note that the mean diameter of unquenched bulk spheres (30 nm, Table 2-2) is larger than the mean diameter of dialyzed bulk spheres (24 nm, Table S2-4), confirming removal of solvent and core deswelling during the quenching/dialysis process. We find that the mean sizes of dialyzed spheres formed at the two higher flow rates (50 and 100 μL/min) are somewhat larger (~30 nm, Table S2-4) than those formed in the bulk and at the lower flow rate of 25 μL/min (~24 nm, Table S2-4), suggesting that for nanoparticles formed at higher shear rates, the shear history is not completely erased by quenching and overnight dialysis even though the flow-directed morphologies (cylinders, LCMs and spooled cylinders) have not persisted.

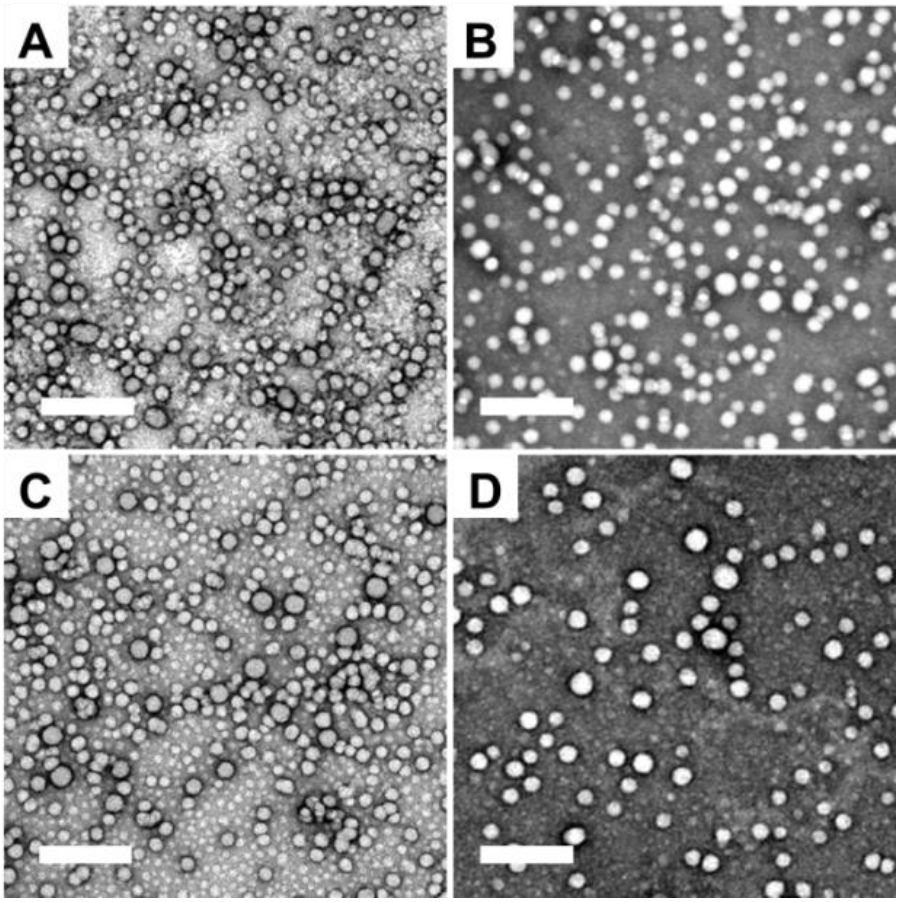

Figure 2-6. Effect of dialysis on NBA-22 nanoparticle structure. TEM images of dialyzed NBA-22 nanoparticles formed in the bulk (A) and in the microfluidic reactor at various flow rates: 25 μL/min (B), 50 μL/min (C), and 100 μL/min (D). Scale bars are 200 nm.

2.3.6. Effect of Aging on Nanoparticle Structure.

Since the unquenched NBA-22 nanoparticle sample formed at the highest flow rate (100 μL/min) contained all three flow-directed morphologies (cylinders, LCMs and spooled cylinders), we also investigated the time stability of these various structures under quiescent conditions, after collection from the chip but without quenching and dialysis (Figure 2-7). Immediately after collection (Figure 2-7A), all three flow-directed morphologies were present, in addition to the equilibrium morphology of spheres. After

only 1 day, although most of the initial morphologies could still be identified, no spooled cylinders were found on the TEM grids. Instead, prominent loose clusters of hoops, short cylinders, and medium cylinders (Figure 2-7B) suggest the spontaneous unwinding and breakup of the spooled cylinders over 1 day. After 3 days (Figure 2-7C), these clusters had disappeared but LCMs and small spheres continued to persist. We note that starting at 1 day, some LCMs had started to develop a porous structure and that by 3 days this had become a prominent feature of many LCMs (Figure 2-7C, inset). Finally, after 7 days, the equilibrium spheres were the prominent morphology, and residual LCMs appeared to be much smaller or else had degraded into irregularly shaped loose porous structures (Figure 2-7D). These observations suggest that the spooled cylinders represent the most unstable morphology of the various flow-directed nanoparticles formed in the microfluidic channels. This is consistent with the fact that they are the one identified structure from NBA-22 found to be present in significant numbers only at the highest flow rate, and so should possess the highest excess free energy (compared to thermodynamically stable states, Scheme 2-1). The effects of aging on NBA-52 and NBA-66 nanoparticles are shown in Figure S2-14 and Figure S2-15, respectively.

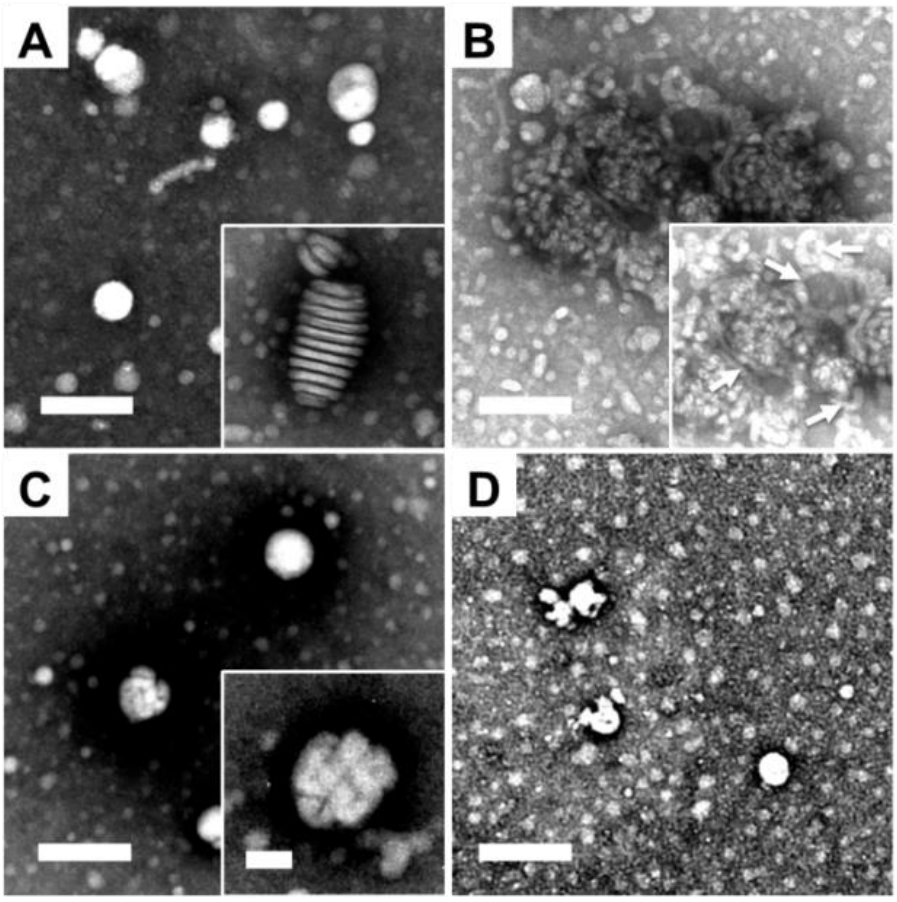

Figure 2-7. Effect of aging on NBA-22 nanoparticle structure. TEM images of unquenched NBA-22 nanoparticles formed in the microfluidic reactor at 100 μL/min and imaged immediately (A), and corresponding aged nanoparticles after 1 day (B), 3 days (C) and 7 days (D). Inset to A shows a spooled cylinder found in a different region of the same sample; inset to B shows a detail of the main image at increased brightness but the same magnification; inset to C shows a porous LCM at higher magnification. Scale bars are 200 nm (main images) and 50 nm (C, inset); other insets share the same scale bar as the main images.

2.3.7. Effect of Flow-Directed Structure on Light-Triggered Nanoparticle Dissociation.

Finally, we compared the light-triggered dissociation of the NBA-22 nanoparticles prepared by the bulk method and on-chip at flow rates of 25 μL/min (Figure 2-3B) and 100 μL/min (Figure 2-3D). TEM data of on-chip samples at selected irradiation times of

0 s, 35 s, 65 s, 95 s, 215 s, and 410 s (Figure 2-8, A-L) were compared. In all of these images (obtained with reverse staining), PNBA cores are identified as distinct white PNBA particles with a surrounding dark boundary of the PDMA coronae; based on this criterion, for the two samples we identified irradiation times at which PNBA-*b*-PDMA nanoparticles can no longer be identified in the TEM images. For the 25 μL/min sample, small irregularly-shaped PNBA-*b*-PDMA nanoparticles are identified after 215 s of irradiation (Figure 2-8E), but no such features are visible after 410 s of irradiation (Figure 8F). On the other hand, for the 100 μL/min sample, we identify PNBA-*b*-PDMA nanoparticles up to 95 s of irradiation (Figure 2-8J) but find that such nanoparticles have completely dissociated by 215 s of irradiation (Figure 2-8K). These TEM data therefore support the conclusion that light-triggered dissociation is faster for the nanoparticles prepared at higher flow rate. Insight into the relative stabilities of the various flow-induced nanoparticles during irradiation can also be obtained from the TEM data in Figure 2-8. Nanoparticles formed at low flow rate begin as spheres and short cylinders before irradiation (Figure 2-8A); after 35 s irradiation, these morphologies still persist although the diameters and widths of spheres and cylinders have decreased significantly (Figure 2-8B). However, in addition to nanoparticle dissociation, a second population of larger spheres have appeared after 35 s and persist through to 65 s irradiation time (Figure 2-8C); this suggests that during the photocleaving reaction, either intraparticle chain rearrangements or the association of more hydrophilic unimers released from dissociating nanoparticles lead to the formation of new transient nanoparticle populations prior to complete dissociation. In contrast, irradiation of the 100 μL/min sample leads to complete disappearance of spooled cylinders (Figure 2-8G) within the first 35 s of

irradiation (Figure 2-8H) while both small spheres and LCMs persist but have become smaller. Larger versions of the TEM images in Figure 8, A-L are available in Supporting Information (Figures S2-16 and S2-17).

Figure 8M shows the corresponding decrease in normalized light scattering intensity upon irradiation of the nanoparticles, associated with the concomitant decrease in nanoparticle concentration as the nanoparticles dissociate. The 100 μL/min sample shows significantly faster decay (red, $t_{1/2}$ = 40 s) than that prepared at 25 μL/min (blue, $t_{1/2}$ = 70 s), indicating faster light-triggered nanoparticle dissociation for the former sample. As expected, the bulk control sample shows the slowest rate of photodegradation (black, $t_{1/2}$ = 80 s). In addition to scattered light intensity, we also tracked changes in mean hydrodynamic diameter by DLS for the first 100 s of irradiation (Figure 2-8N) over which time the scattering intensity decays to ≤ 20% of its initial value for both samples; the corresponding ~25% decrease in mean hydrodynamic size of the 100 μL/min sample (Figure 2-8N, red) suggests the preferential dissociation of larger nanoparticles in the first 100 s of irradiation, in contrast to the slight increase in mean hydrodynamic size for the 25 μL/min and bulk samples (Figure 2-8N, blue and black) which we attribute to the formation of transient larger particles during irradiation as discussed above. The fast dissociation of spooled cylinders and concomitant gradual dissociation of spheres and LCMs observed by TEM for the 100 μL/min sample (Figure 2-8, G-L), without the formation of transient larger nanoparticles, are consistent with the observed decrease in mean hydrodynamic size as the nanoparticles dissociate (Figure 2-8N).

The relatively fast light-triggered dissociation of spooled cylinders compared to other morphologies is attributed to the higher excess free energy (with respect to

equilibrium states) of these unusual flow-induced assemblies (Scheme 2-1). This rapid dissociation suggests that the tunable shear forces within the microfluidic multiphase reactor allow variable amounts of chemical strain to be built into colloidal nanostructures simply by changing the flow rate. In theory, this platform provides a new handle on controlling the responsivity of smart colloids upon exposure to various stimuli. For example, for drug delivery applications, one could envision loading co-active drugs for which relative release times are crucial into the same photoresponsive block copolymer but at different flow rates; upon simultaneous exposure to light, drug A (encapsulated at high flow rate) would be released first, followed by drug B (encapsulated at low flow rate), due to the higher chemical strain built into the former nanoparticles during on-chip self-assembly. For this and other applications, future strategies for integrating shear-directed nanoparticle formation with on-chip nanoparticle separation, in order to isolate specific nanostructures, are currently being considered.

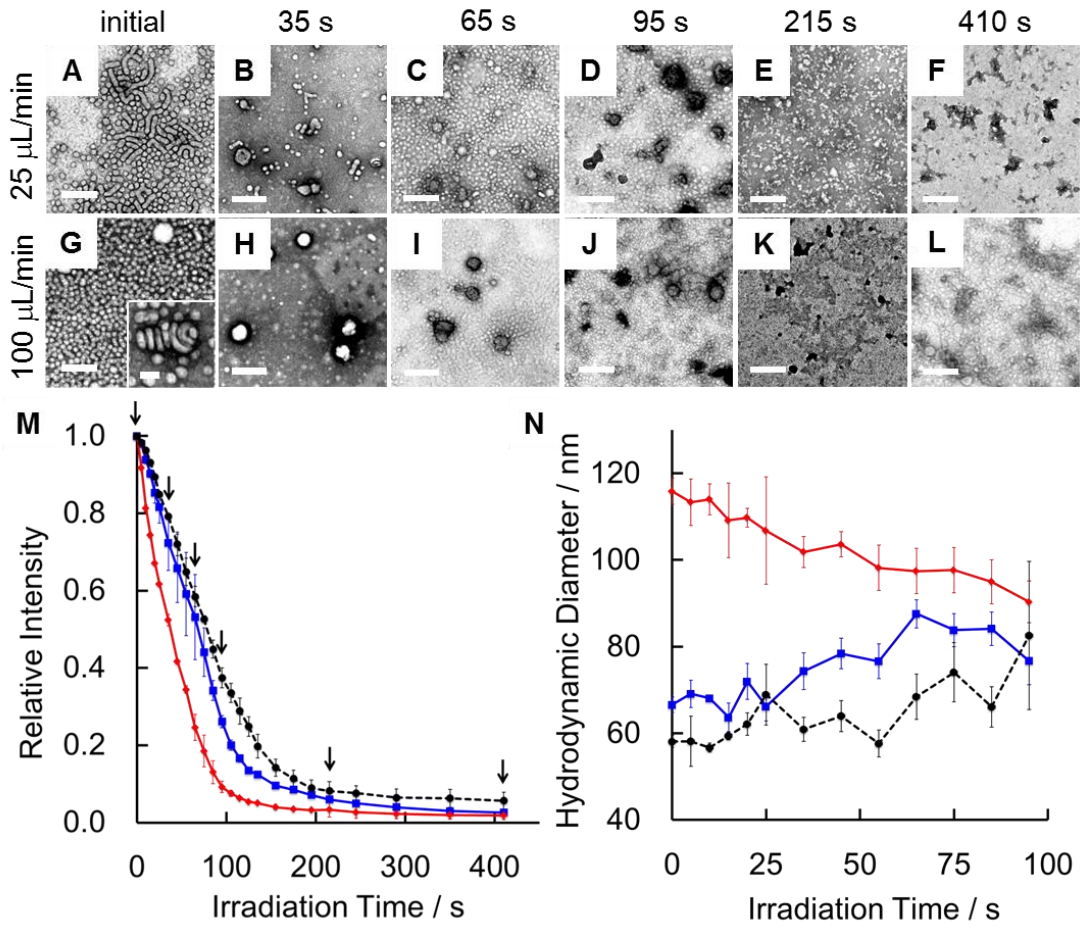

Figure 2-8. Effect of flow rate on light-triggered dissociation of NBA-22 nanoparticles. (A-L) TEM images of irradiated NBA-22 nanoparticles formed in the microfluidic reactor at 25 μL/min and 100 μL/min for different irradiation times. Inset to G shows a spooled cylinder found in a different region of the same sample. Scale bars are 200 nm (main images) and 50 nm (G, inset). (M) Mean relative light scattering intensity versus irradiation time (averaged from three separate nanoparticle preparations). Arrows show times at which TEM images were taken. Bulk: black circles, 25 μL/min: blue squares, 100 μL/min: red diamonds. (N) Mean hydrodynamic size versus irradiation time (averaged from three measurements of one nanoparticle preparation).

2.4. Conclusion

We have demonstrated the flow-directed self-assembly of various PNBA-*b*-PDMA copolymers with different hydrophobic and photoresponsive PNBA block lengths (NBA-

22, NBA-52, NBA-66) in a gas-liquid segmented microfluidic reactor. Using conventional bulk water addition, small spherical nanoparticles were obtained for all copolymers, whereas on-chip flow-directed assembly produced a variety of morphologies dependent on flow rate, including short cylinders, LCMs, and unique spooled cylinders. Similar structures and trends were observed for all three copolymers, with spheres and short cylinders, then LCMs, then spooled cylinders appearing as flow rate increased. The higher excess free energy of spooled cylinders relative to equilibrium states was evidenced by their faster off-chip relaxation times (~1 day) compared to other flow-directed structures. Light-triggered dissociation of flow-directed nanoparticles prepared from NBA-22 at two different flow rates showed faster decay in light scattering intensity for the sample prepared at faster flow rate, associated with the fast disruption of spooled cylinders. The application of variable on-chip shear to direct not only the structure but the responsivity of materials sensitive to light offers numerous interesting possibilities for controlled microfluidic manufacturing of "smart" polymeric colloids.

2.5. Supporting Information

Please see Appendix A for supporting information: Data for cwc determination; Sample image of stable two-phase flow; Table of actual flow conditions; UV-Vis spectra of copolymer and copolymer nanoparticles; Irradiation controls; TEM images of triplicate preparations; Additional size histograms and TEM images of NBA-52 and NBA-66 nanoparticles; Additional TEM tomography; Larger versions of TEM images in Figure 2-8.

2.6. References

1. Z. Xu, B. Yan, J. Riordon, Y. Zhao, D. Sinton and M. G. Moffitt Microfluidic Synthesis of Photoresponsive Spool-Like Block Copolymer Nanoparticles: Flow-Directed Formation and Light-Triggered Dissociation. *Chemistry of Materials* **2015,** *27*, 8094.

2. J. Hu and S. Liu Responsive Polymers for Detection and Sensing Applications: Current Status and Future Developments. *Macromolecules* **2010,** *43*, 8315.

3. C. Oerlemans, W. Bult, M. Bos, G. Storm, J. F. Nijsen and W. Hennink Polymeric Micelles in Anticancer Therapy: Targeting, Imaging and Triggered Release. *Pharm. Res.* **2010,** *27*, 2569.

4. C. Allen, D. Maysinger and A. Eisenberg Nano-Engineering Block Copolymer Aggregates for Drug Delivery. *Colloids and Surfaces B: Biointerfaces* **1999,** *16*, 3.

5. D. E. Discher, V. Ortiz, G. Srinivas, M. L. Klein, Y. Kim, D. Christian, S. Cai, P. Photos and F. Ahmed Emerging Applications of Polymersomes in Delivery: From Molecular Dynamics to Shrinkage of Tumors. *Prog. Polym. Sci.* **2007,** *32*, 838.

6. Z. L. Tyrrell, Y. Shen and M. Radosz Fabrication of Micellar Nanoparticles for Drug Delivery through the Self-Assembly of Block Copolymers. *Prog. Polym. Sci.* **2010,** *35*, 1128.

7. S. Parveen, R. Misra and S. K. Sahoo Nanoparticles: A Boon to Drug Delivery, Therapeutics, Diagnostics and Imaging. *Nanomed. Nanotechnol. Biol. Med.* **2012,** *8*, 147.

8. J. Gong, M. Chen, Y. Zheng, S. Wang and Y. Wang Polymeric Micelles Drug Delivery System in Oncology. *J. Control. Release* **2012,** *159*, 312.

9. Z. Ahmad, A. Shah, M. Siddiq and H.-B. Kraatz Polymeric Micelles as Drug Delivery Vehicles. *RSC Adv.* **2014,** *4*, 17028.

10. N. S. Oltra, P. Nair and D. E. Discher From Stealthy Polymersomes and Filomicelles to "Self" Peptide-Nanoparticles for Cancer Therapy. *Annu. Rev. Chem. Biomol. Eng.* **2014,** *5*, 281.

11. M. Yokoyama Polymeric Micelles as Drug Carriers: Their Lights and Shadows. *J. Drug Targeting* **2014,** *22*, 576.

12. J. E. Chung, M. Yokoyama, M. Yamato, T. Aoyagi, Y. Sakurai and T. Okano Thermo-Responsive Drug Delivery from Polymeric Micelles Constructed Using Block Copolymers of Poly(N−Isopropylacrylamide) and Poly(Butylmethacrylate). *J. Control. Release* **1999,** *62*, 115.

13. M. Kurisawa, M. Yokoyama and T. Okano Gene Expression Control by Temperature with Thermo-Responsive Polymeric Gene Carriers. *J. Control. Release* **2000,** *69*, 127.

14. S. Cammas, K. Suzuki, C. Sone, Y. Sakurai, K. Kataoka and T. Okano Thermo-Responsive Polymer Nanoparticles with a Core-Shell Micelle Structure as Site-Specific Drug Carriers. *J. Control. Release* **1997,** *48*, 157.

15. E. R. Gillies and J. M. J. Fréchet Ph-Responsive Copolymer Assemblies for Controlled Release of Doxorubicin. *Bioconjugate Chem.* **2005,** *16*, 361.

16. J. D. Debord and L. A. Lyon Synthesis and Characterization of Ph-Responsive Copolymer Microgels with Tunable Volume Phase Transition Temperatures. *Langmuir* **2003,** *19*, 7662.

17. J. Rodríguez-Hernández and S. Lecommandoux Reversible inside-out Micellization of Ph-Responsive and Water-Soluble Vesicles Based on Polypeptide Diblock Copolymers. *J. Am. Chem. Soc.* **2005,** *127*, 2026.

18. G. Wang, X. Tong and Y. Zhao Preparation of Azobenzene-Containing Amphiphilic Diblock Copolymers for Light-Responsive Micellar Aggregates. *Macromolecules* **2004,** *37*, 8911.

19. J.-M. Schumers, C.-A. Fustin and J.-F. Gohy Light-Responsive Block Copolymers. *Macromol. Rapid Commun.* **2010,** *31*, 1588.

20. F. D. Jochum and P. Theato Thermo- and Light Responsive Micellation of Azobenzene Containing Block Copolymers. *Chem. Commun.* **2010,** *46*, 6717.

21. N. Ma, Y. Li, H. Xu, Z. Wang and X. Zhang Dual Redox Responsive Assemblies Formed from Diselenide Block Copolymers. *J. Am. Chem. Soc.* **2010,** *132*, 442.

22. Y.-C. Wang, F. Wang, T.-M. Sun and J. Wang Redox-Responsive Nanoparticles from the Single Disulfide Bond-Bridged Block Copolymer as Drug Carriers for Overcoming Multidrug Resistance in Cancer Cells. *Bioconjugate Chem.* **2011,** *22*, 1939.

23. J. Liu, Y. Pang, W. Huang, Z. Zhu, X. Zhu, Y. Zhou and D. Yan Redox-Responsive Polyphosphate Nanosized Assemblies: A Smart Drug Delivery Platform for Cancer Therapy. *Biomacromolecules* **2011,** *12*, 2407.

24. N. Fomina, J. Sankaranarayanan and A. Almutairi Photochemical Mechanisms of Light-Triggered Release from Nanocarriers. *Adv. Drug Del. Rev.* **2012,** *64*, 1005.

25. J. Jiang, X. Tong, D. Morris and Y. Zhao Toward Photocontrolled Release Using Light-Dissociable Block Copolymer Micelles. *Macromolecules* **2006,** *39*, 4633.

26. R. Karnik, F. Gu, P. Basto, C. Cannizzaro, L. Dean, W. Kyei-Manu, R. Langer and O. C. Farokhzad Microfluidic Platform for Controlled Synthesis of Polymeric Nanoparticles. *Nano Lett.* **2008,** *8*, 2906.

27. C.-X. Zhao, L. He, S. Z. Qiao and A. P. J. Middelberg Nanoparticle Synthesis in Microreactors. *Chem. Eng. Sci.* **2011,** *66*, 1463.

28. G. Wang, G. Shi, H. Wang, Q. Zhang and Y. Li In Situ Functionalization of Stable 3d Nest-Like Networks in Confined Channels for Microfluidic Enrichment and Detection. *Adv. Funct. Mater.* **2014,** *24*, 1017.

29. G. Wang, C. Yuan, B. Fu, L. He, E. Reichmanis, H. Wang, Q. Zhang and Y. Li Flow Effects on the Controlled Growth of Nanostructured Networks at Microcapillary Walls for Applications in Continuous Flow Reactions. *ACS Appl. Mater. Interfaces* **2015,** *7*, 21580.

30. R. Hinchet and S.-W. Kim Wearable and Implantable Mechanical Energy Harvesters for Self-Powered Biomedical Systems. *ACS Nano* **2015,** *9*, 7742.

31. L. Zhang and A. Eisenberg Multiple Morphologies of "Crew-Cut" Aggregates of Polystyrene−B-Poly(Acrylic Acid) Block Copolymers. *Science* **1995,** *268*, 1728.

32. L. Zhang and A. Eisenberg Multiple Morphologies and Characteristics of "Crew-Cut" Micelle-Like Aggregates of Polystyrene−B-Poly(Acrylic Acid) Diblock Copolymers in Aqueous Solutions. *J. Am. Chem. Soc.* **1996,** *118*, 3168.

33. L. Zhang, K. Yu and A. Eisenberg Ion-Induced Morphological Changes in "Crew-Cut" Aggregates of Amphiphilic Block Copolymers. *Science* **1996,** *272*, 1777.

34. G. Schabas, C.-W. Wang, A. Oskooei, H. Yusuf, M. G. Moffitt and D. Sinton Formation and Shear-Induced Processing of Quantum Dot Colloidal Assemblies in a Multiphase Microfluidic Chip. *Langmuir* **2008,** *24*, 10596.

35. C.-W. Wang, A. Oskooei, D. Sinton and M. G. Moffitt Controlled Self-Assembly of Quantum Dot−Block Copolymer Colloids in Multiphase Microfluidic Reactors. *Langmuir* **2010,** *26*, 716.

36. C.-W. Wang, D. Sinton and M. G. Moffitt Flow-Directed Block Copolymer Micelle Morphologies Via Microfluidic Self-Assembly. *Journal of the American Chemical Society* **2011,** *133*, 18853.

37. C.-W. Wang, A. Bains, D. Sinton and M. G. Moffitt Flow-Directed Assembly of Block Copolymer Vesicles in the Lab-on-a-Chip. *Langmuir* **2012,** *28*, 15756.

38. C.-W. Wang, D. Sinton and M. G. Moffitt Morphological Control Via Chemical and Shear Forces in Block Copolymer Self-Assembly in the Lab-on-Chip. *ACS Nano* **2013,** *7*, 1424.

39. A. Bains, Y. Cao and M. G. Moffitt Multiscale Control of Hierarchical Structure in Crystalline Block Copolymer Nanoparticles Using Microfluidics. *Macromol. Rapid Commun.* **2015,** *In Press*.

40. B. Yan, J.-C. Boyer, N. R. Branda and Y. Zhao Near-Infrared Light-Triggered Dissociation of Block Copolymer Micelles Using Upconverting Nanoparticles. *J. Am. Chem. Soc.* **2011,** *133*, 19714.

41. B. Yan, X. Tong, P. Ayotte and Y. Zhao Light-Responsive Block Copolymer Vesicles Based on a Photo-Softening Effect. *Soft Matter* **2011,** *7*, 10001.

42. Y. Yu, L. Zhang and A. Eisenberg Morphogenic Effect of Solvent on Crew-Cut Aggregates of Apmphiphilic Diblock Copolymers. *Macromolecules* **1998,** *31*, 1144.

43. S. A. Kazemi Oskooei and D. Sinton Partial Wetting Gas-Liquid Segmented Flow Microreactor. *Lab Chip* **2010,** *10*, 1732.

44. G. N. Malcolm and J. S. Rowlinson The Thermodynamic Properties of Aqueous Solutions of Polyethylene Glycol, Polypropylene Glycol and Dioxane. *Trans Faraday Soc* **1957,** *53*, 921.

45. T. Ribeiro, T. J. V. Prazeres, M. Moffitt and J. P. S. Farinha Enhanced Photoluminescence from Micellar Assemblies of Cadmium Sulfide Quantum Dots and Gold Nanoparticles. *J. Phys. Chem. C* **2013,** *117*, 3122.

46. L. Zhang, C. Bartels, Y. Yu, H. Shen and A. Eisenberg Mesosized Crystal-Like Structure of Hexagonally Packed Hollow Hoops by Solution Self-Assembly of Diblock Copolymers. *Phys. Rev. Lett.* **1997,** *79*, 5034.

47. S. Zhong, H. Cui, Z. Chen, K. L. Wooley and D. J. Pochan Helix Self-Assembly through the Coiling of Cylindrical Micelles. *Soft Matter* **2008,** *4*, 90.

48. J. Xu, H. Wang, C. Liu, Y. Yang, T. Chen, Y. Wang, F. Wang, X. Liu, B. Xing and H. Chen Mechanical Nanosprings: Induced Coiling and Uncoiling of Ultrathin Au Nanowires. *J. Am. Chem. Soc.* **2010,** *132*, 11920.

49. H. A. Stone Dynamics of Drop Deformation and Breakup in Viscous Fluids. *Anne. Rev. Fluid Mech.* **1994,** *26*, 65.

50. D. Saenger and H. Barzynski Process of Making and Using a Positive Working Photosensitive Film Resist Material. US4576902 A, 18 Mar, 1986.

Chapter 3.

Comparison of Single-Phase and Two-Phase Microfluidic Mixing for Block Copolymer Nanoparticle Formation

3.1. Introduction

In the past decade, there has been tremendous progress in the development of microfluidic systems for use in chemical[1-3] and nanoparticle[4-6] synthesis, including drug-loaded nanoparticles. The high control precision of flow rate, small reagent consumption, enhanced heat transfer and the ability to incorporate different processes onto one device makes microfluidics a very convenient platform for synthesis. Laminar flow is observed in micro-scaled channels, so mixing is dominated by diffusion. That's to say, the mixing rate is lower than those in turbulent flow.

There are two major strategies for achieving fast mixing of reagents in microfluidic reactors. In single-phase reactors, complex grooved patterns, such as a staggered herringbone structure, have been employed to improve mixing. This type of reactor was invented by Whitesides group.[7, 8] Experiments were done to mix dye on the reactor and fast mixing was observed when a herringbone structures was present within the microfluidic device.[8] Computational fluid dynamics (CFD) and other calculation models were used to study the flow pattern of these reactors.[8-12] When liquid passes through a groove, a swirl is generated and this in turn disturbs the flow in the main channel, leading to rapid mixing.[10] Deeper grooves improve mixing better but create more dead volume.[11] The wall shear rate of 800 s^{-1} on a similar herringbone single-phase microfluidic reactor was reported in literature.[13] This system has been used by the Cullis group to synthesize

phospholipid nanoparticles; by changing flow rate and flow ratio, control of size was achieved and the polydispersity was better than nanoparticles formed by conventional methods under the same chemical condition.[14-16] This chip design is already commercialized and sold by the company Presicion Nanosystems as a benchtop device for fabricating lipid-based drug delivery systems.

An alternative mixing strategy is the two-phase reactor, including gas-liquid reactors and liquid-liquid reactors. Gas liquid reactors are more common and easier to use, developed by Ismagilov group[17] and Jensen group[18]. Its applications in block copolymer self-assembly was studied by Moffitt group.[19] In a gas-liquid segmented microfluidic reactor, the introduction of gas bubbles induces rotating vortices in liquid plugs, improving mass and heat transfer. Compared to single-phase flow, gas-liquid segmented flow features rapid mixing, reduced residence time distribution and narrow size distribution.[20] In our group, we have shown that a gas-liquid segmented microfluidic reactor could be used to synthesize PS-*b*-PAA and PCL-*b*-PEO nanoparticles of various morphologies.[19, 21-23] The structures of the on-chip prepared nanoparticles were distinct from that of the bulk control and change in flow rate had an effect on size and morphology. The difference was explained by shear effect. It was calculated by CFD that the maximum shear rate on this specific chip at 25 μL/min is 1×10^5 s^{-1}, many orders of magnitude higher than the wall shear rate of the single-phase herringbone mixer. The maximum shear rate appeared around the "hot spots" where gas-liquid interface meets the wall.[24] Péclet number and capillary number was estimated, indicating that at low flow rate, Péclet number ~10 increases the probability of shear-induced aggregation,[19] while at

high flow rate, shear rate give rise to capillary number and thus lead to shear-induced breakup.[24]

Shear is known to induce orientation of polymer chains and enhance the nucleation step of polymer crystallization. Increase in shear has a positive effect on crystallinity for polymers in the bulk.[25] Furthermore, our group found that flow rate had a linear positive effect on core crystallinity of PCL-*b*-PEO, likely due to high shear rate.[21]

In this study, we want to compare these reactors with respect to block copolymer nanoparticle formation in order to gain a better understanding of flow-directed control of polymer nanoparticles in the two-phase reactor. Both reactors have fast mixing in common, although the two-phase reactor has a maximum shear rate many orders of magnitude higher than that of the single-phase reactor. PCL-*b*-PEO self-assembly was used to compare single-phase and two-phase microfluidic reactors under the same chemical conditions and at the same variable flow rates. Both reactors formed structures different from bulk-prepared nanoparticles; however, the two-phase reactor showed flow-dependent morphology and crystallinity, in contrast to the single-phase reactor which did not show significant flow dependencies of morphology and crystallinity. This suggests that high shear, and not fast mixing, is responsible for the flow-directed variability of multiscale nanoparticle structure in two-phase microfluidic reactors.

3.2. Experimental

Materials. Stannous octonate (95%), PEG methyl ether (MePEG-OH, MW~5000) and ε-caprolactone (97%) were all purchased from Sigma-Aldrich and used for synthesis of copolymers. Toluene (Caledon, 99.5%), dimethylformamide (DMF, Caledon, 99.8%)

were used as received without further purification. PCL_{105}-*b*-PEO_{114} (PCL-12k) was purchased from Advanced Polymer Materials Inc.

Synthesis of PCL_{44}-*b*-PEO_{114} Copolymer (PCL-5k). The copolymer was synthesized by Dr. Changhai Lu in the Moffitt lab via ring opening polymerization of ε-caprolactone (ε-CL) in the presence of MePEG-OH as the macroinitiator and stannous octonate ($Sn(Oct)_2$) as the catalyst. The polymerization was carried out under a nitrogen atmosphere in a flame-dried round-bottom flask. In brief, following azeotropic distillation in toluene, 5 g of MePEG-OH (1 mmol) was dissolved in a 75 ml volume of dried toluene and ε-CL (5 g, 43.85 mmol) and $Sn(Oct)_2$ were added to the reaction vessel. The polymerization was carried out at 110 °C for 24 hrs with continuous stirring. The copolymer was isolated by precipitation in cold ether and dried under vacuum, followed by characterization with ^{1}H NMR and GPC. Characteristics of the copolymers are tabulated in Table 3-1.

Critical Water Content (cwc) Determination. Critical water content was determined for copolymer solutions in DMF of an initial concentration of 0.33 wt % by dropwise water addition and static light intensity measurement. Sample preparations, instrument used and conditions were the same as described in Chapter 2 experimental. Titration curve is shown in Figure S3-1. Only PCL-5k is shown, because the cwc of PCL12k was determined by another group member. Results are tabulated in Table 3-1. Errors are the standard deviation of three separate solution preparations and measurements.

Table 3-1. Copolymer Characteristics and Critical Water Contents.

Copolymer	m[a]	n	PDI	cwc[b] / wt %
PCL-5k	44	114	2.0[c]	7.1 ± 0.2
PCL-12k	105	114	1.1	5.5 ± 0.1[21]

a) m and n are the number-average degrees of polymerization of the PCL and PEO blocks, respectively.

b) Critical water contents (cwc) were determined for the respective copolymer solutions in DMF at an initial polymer concentration of 0.33 wt %.

c) Calculated by M_n from NMR and M_w from GPC.

Bulk Preparation of PCL-*b*-PEO Nanoparticles. As a control experiment for comparison with on-chip nanoparticle formation, nanoparticles of each block copolymer were also formed by the conventional method of dropwise water addition. For these experiments, deionized water was added dropwise to 3 g of 0.33 wt % copolymer solution in DMF at a rate of 20 μL every 10 s up to a target water content of cwc + 10 wt % with moderate stirring.

NanoAssemblr™ Benchtop Instrument with Microfluidic Mixer (Single-Phase Reactor). Both the benchtop instrument and the single-phase reactor made of glass are products of NanoAssemblr™. The benchtop instrument is a syringe pump and controlled by a laptop. The channels are straight, 79 μm in depth and 200 μm in width. The herringbone pattern is raised from bottom of the channel by 31 μm and the width is 50 μm (Figure 3-1A). The length of channel is 22 mm.

Microfluidic Preparation of PCL-*b*-PEO Nanoparticles on Single-Phase Reactor. For microfluidic preparation of nanoparticles, the following fluid streams were combined within the reactor: (1) 0.66 wt % PEO-*b*-PCL solution in DMF, (2) water/DMF

mixtures. The flow rates of both streams are the same, yielding a final concentration of 0.33 wt % copolymer and either 17.1 or 15.5 wt % water, corresponding to 10.0 wt % above the cwc for PCL-5k and PCL-12k respectively. Experiments were conducted at a total flow rate of 20, 60 and 100 μL/min. For each condition, nanoparticles were collected into an empty vial.

Gas-Liquid Segmented (Two-Phase Reactor) Microfluidic Reactor Fabrication. The two-phase microfluidic reactor (Figure 3-1B) employed in this study is identical to the one discussed in Chapter 2, and the fabrication steps were the same. The resulting reactor has a set channel depth of 150 μm and consists of a sinusoidal mixing channel 100 μm wide and a sinusoidal processing channel 200 μm wide. Length of mixing channel is 161 mm while length of processing channel is 718 mm.

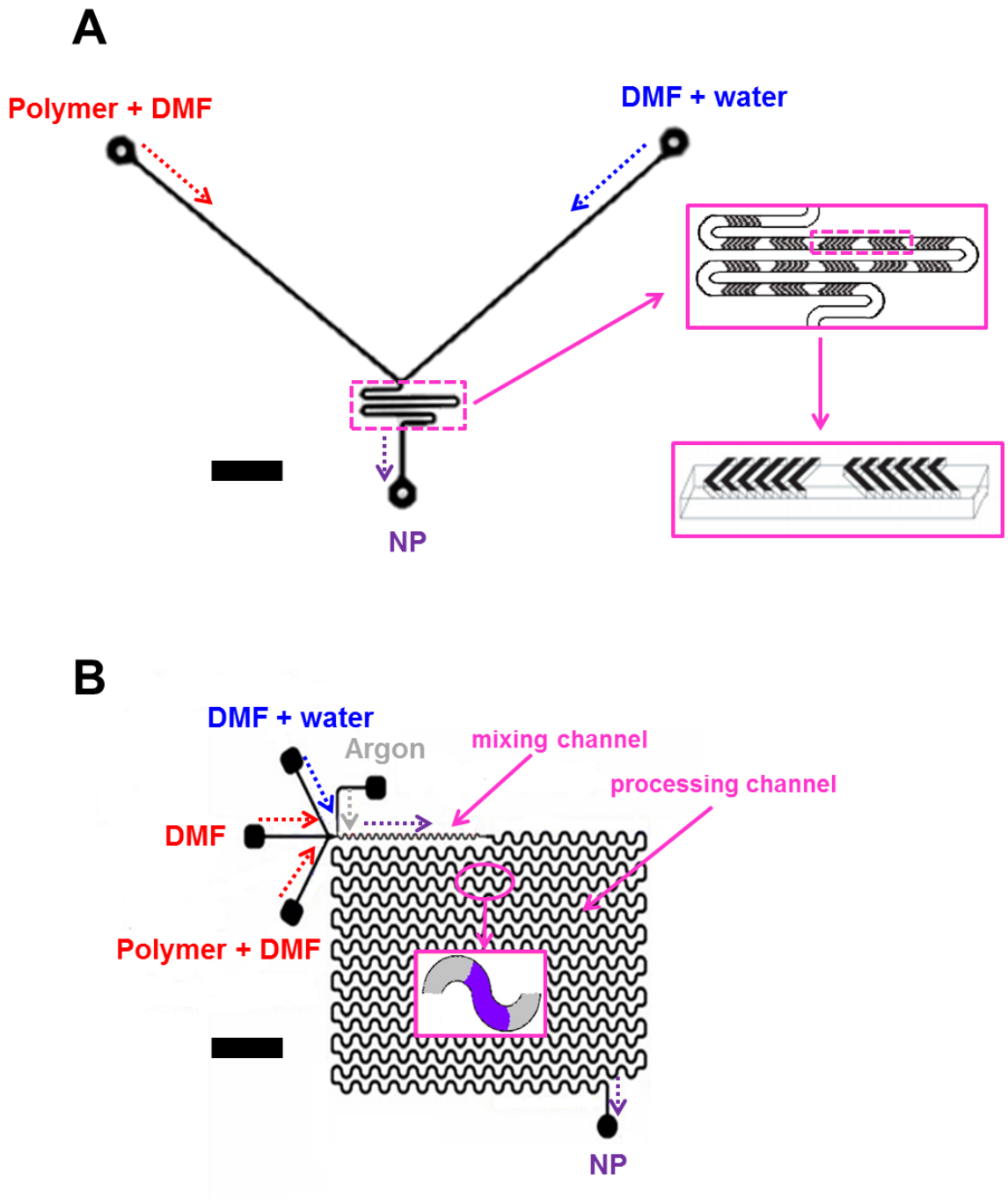

Figure 3-1. Schematic of single-phase (A) and two-phase (B) microfluidic reactors.

Flow Delivery and Control. Pressure-driven flow of liquids to the reactor inlet was provided using 1 mL gastight syringes (Hamilton, Reno, NV) mounted on syringe pumps (Harvard Apparatus, Holliston, MA). The microfluidic chip was connected to the

liquid syringes via 1/16th-inch (OD) Teflon tubing (Scientific Products and Equipment, ON). Gas flow was introduced to the chip via an Ar tank regulator and a downstream regulator (Johnston Controls) for fine adjustments. The chip was connected to the downstream regulator through a 1/16th-inch (OD) / 100-μm (ID) Teflon tube (Upchurch Scientific, Oak Harbor, WA). The liquid flow rate (Q_{liq}) was programmed via the syringe pumps and the gas flow rate (Q_{gas}) was fine-tuned via the downstream pressure regulator in order to set the nominal total flow rates of 20, 60 and 100 μL/min described in the main text. For all experiments, the relative gas-to-liquid flow ratio, Q_{gas}/Q_{liq} ~1.

Visualization of the gas bubbles and liquid plugs within the microfluidic reactor was achieved using an upright optical microscope (Omax) with a 10 × objective lens. Images were captured using a 2.07 megapixel PupilCam (Ken-A-Vision). Actual flow parameters pertaining to each microfluidic experiment described are listed in Table S3-1.

Microfluidic Preparation of PCL-*b*-PEO Nanoparticles on Two-Phase Reactor. For microfluidic preparation of nanoparticles, the following three fluid streams were combined to form gas-segmented liquid plugs within the reactor: (1) 1.0 wt % PEO-*b*-PCL solution in DMF, (2) pure DMF, and (3) water/DMF mixtures. The flow rates of the three liquid streams are the same, yielding steady-state on-chip concentrations of 0.33 wt % copolymer and either 17.1 or 15.5 wt % water, corresponding to 10.0 wt % above the cwc for PCL-5k and PCL-12k respectively. For each condition, nanoparticles were collected into an empty vial.

Transmission Electron Microscopy. Negatively-stained samples for TEM imaging were prepared by depositing a drop of block copolymer nanoparticle dispersion on a carbon-coated 300-mesh copper TEM grid followed by a drop of 1 wt % uranyl

acetate aqueous solution as a negative staining agent. Excess liquid was immediately removed using lens paper, followed by drying of the remaining liquid under ambient conditions. For unstained TEM samples, a drop of dispersion was deposited on the grid and then vitrified by flash freezing in liquid ethane followed by freeze-drying under vacuum. Imaging was performed on a JEOL JEM-1400 transmission electron microscope, operating at an accelerating voltage of 80 kV and equipped with a Gatan Orius SC1000 CCD camera. For each preparation, at least 5 images were taken in different regions of the grid.

For each copolymer and flow condition, morphology and size analysis was performed based on at least three images taken in different regions of the grid. Mean dimensions for each condition were determined from a total of 400 nanoparticles for spheres and 150 nanoparticles for cylinders or vesicles. Identified morphologies and mean dimensions for each copolymer and preparation condition are reported in Table 3-2. Averaging and statistical analysis of dimensions from TEM images were conducted using Image J software.

X-Ray Diffraction. For XRD sample preparation, solvent was removed from nanoparticles in water/DMF by rotary evaporation at 25 °C until solid films were obtained. The resulting films were then scraped as a powder onto the XRD specimen holder.

X-ray diffraction measurements were performed on a Rigaku Miniflex diffractometer with a Cr source (KR radiation, λ = 2.2890 Å) operating at 30 kV and 15 mA with a resolution of 0.05° (2θ) and a scan speed of 1°/min. X-ray diffraction profiles were collected for 2θ ranging from 10-50°.

Peak deconvolution was done using Origin Pro 2015. Two characteristic reflections for each of crystalline PCL and crystalline PEO were identified and used to fix the positions of four Lorentzian peak contributions to the fit;[26] another small Lorentzian peak contribution was used to account for a small shoulder on the more intense PCL peak in order to obtain a good fit. Thus, XRD data were fit to a sum of 6 Lorentzian functions: 3 peaks assigned to crystalline PCL (2θ = 32.5, 32.7, and 35.7), 2 peaks assigned to crystalline PEO (2θ = 29.2 and 35.2), and 1 peak (no fixed position) assigned to incoherent scattering from amorphous copolymer (amorphous halo). Areal peak contributions from the three components (crystalline PCL, crystalline PEO, and amorphous copolymer) were then determined by integration and percentages of crystalline PCL and PEO were calculated using:

$$\%\ \textit{Crystalline}\ \text{PCL} = A_{\text{PCL}}/A_{\text{total}} \qquad (3\text{-}1)$$

Reported *% Crystalline* PCL values from XRD are averages determined from triplicate nanoparticle preparations under the specified conditions.

3.3. Results and Discussion

3.3.1. Effect of PCL Block Length on the Structure of Bulk-Prepared Nanoparticles

Figure 3-2 shows the TEM images of PCL-5k and PCL-12k nanoparticles formed in the bulk by dropwise water addition. Size analysis results from TEM images are tabulated in Table 3-2. PCL-5k formed cylinders and some very small spheres with a mean diameter of 9.4 nm on the background (Figure 3-2A). PCL-12k formed spheres with a mean diameter of 26 nm (Figure 3-2B).

Spheres in PCL-5k sample were much smaller than that in PCL-12k sample (Table 3-2). For PCL-5k, fully stretched diameter is 77 nm and a random coil is about 3 nm. Spheres that are about 9 nm in diameter are likely to have a very low degree of chain stretching in the core. A study of PS-*b*-PAA nanoparticles showed that with an increasing PS block length, there was a decrease in curvature of structure and in the meantime an increase in size.[27] However, in this system, when we increased hydrophobic chain (PCL) length, smaller size and higher structural curvature were observed, which indicates an opposite trend to the PS-*b*-PAA system.

It was found by Eisenberg and coworkers that PCL-*b*-PEO that originally formed spheres by dropwise water addition slowly transformed into rods over a few days under ambient condition, and the process was driven by increasing crystallinity.[28] In our bulk experiments (Figure 3-2), as water content increased during nanoparticle preparation, crystallization drove chain rearrangement in favour of formation of cylinders or other low curvature morphologies. With a shorter PCL block, PCL-5k is more dynamic than PCL-12k. Therefore, PCL chains in PCL-5k nanoparticles could respond to the increase in crystallinity quickly and rearrange to form cylinders (Figure 3-2A). However, chain

kinetics of PCL-12k was so low that crystallization took place in the core but wasn't able to induce cylinder formation on the time scale of the experiment, so that only spheres were formed (Figure 3-2B). After quenching, nanoparticles were exposed to plenty of water and solvent was driven out of the core. Therefore, hydrophobic chain kinetics became even lower. Without chain mobility, the core was kinetically frozen.

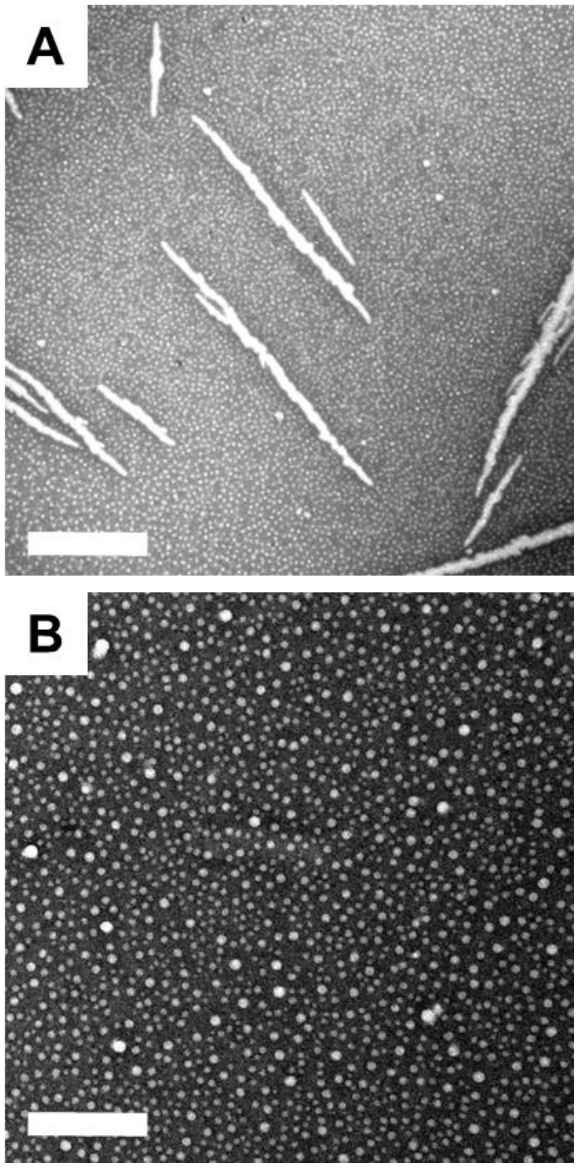

Figure 3-2. Effect of PCL block length on bulk-prepared PCL-5k (A) and PCL-12k (B) nanoparticle morphology through TEM. Scale bars are 400 nm.

Table 3-2. Morphologies[a] and Mean Dimensions[b] for PCL-*b*-PEO Nanoparticles Prepared in Single-Phase and Two-Phase Microfluidic Reactors at Various Flow Rates.

Copolymer, Reactor	Bulk	20 μL/min	60 μL/min	100 μL/min
PCL-5k				
Single-phase Reactor	SS (9.4 ± 0.3 nm) C (32 ± 3 nm)	C (15 ± 1 nm) L	C (17 ± 2 nm) L	C (18 ± 1 nm) L
Two-phase Reactor		SS (8.8 ± 0.1 nm) C (16.8 ± 0.2 nm) L	C (23 ± 2 nm) L	SS (8 ± 1 nm) S (38 ± 2 nm) C (21 ± 2 nm) L
PCL-12k				
Single-phase Reactor	S (26 ± 1 nm)	S (40 ± 2 nm) C (24 ± 2 nm) L	S (40 ± 5 nm) C (26 ± 5 nm) L	S (39 ± 2 nm) C (26 ± 2 nm) L
Two-phase Reactor		S (41 ± 7 nm) C (21 ± 3 nm) L	V (7 ± 2 nm)	S (32 ± 1 nm)

a) Morphologies are indicated as SS (small spheres), S (spheres), C (cylinders or rods), V (vesicles) and L (lamellae).

b) Numbers refer to sphere diameters, cylinder widths or vesicle wall thickness. Errors for samples are standard deviations of mean values determined for three images of the same preparation.

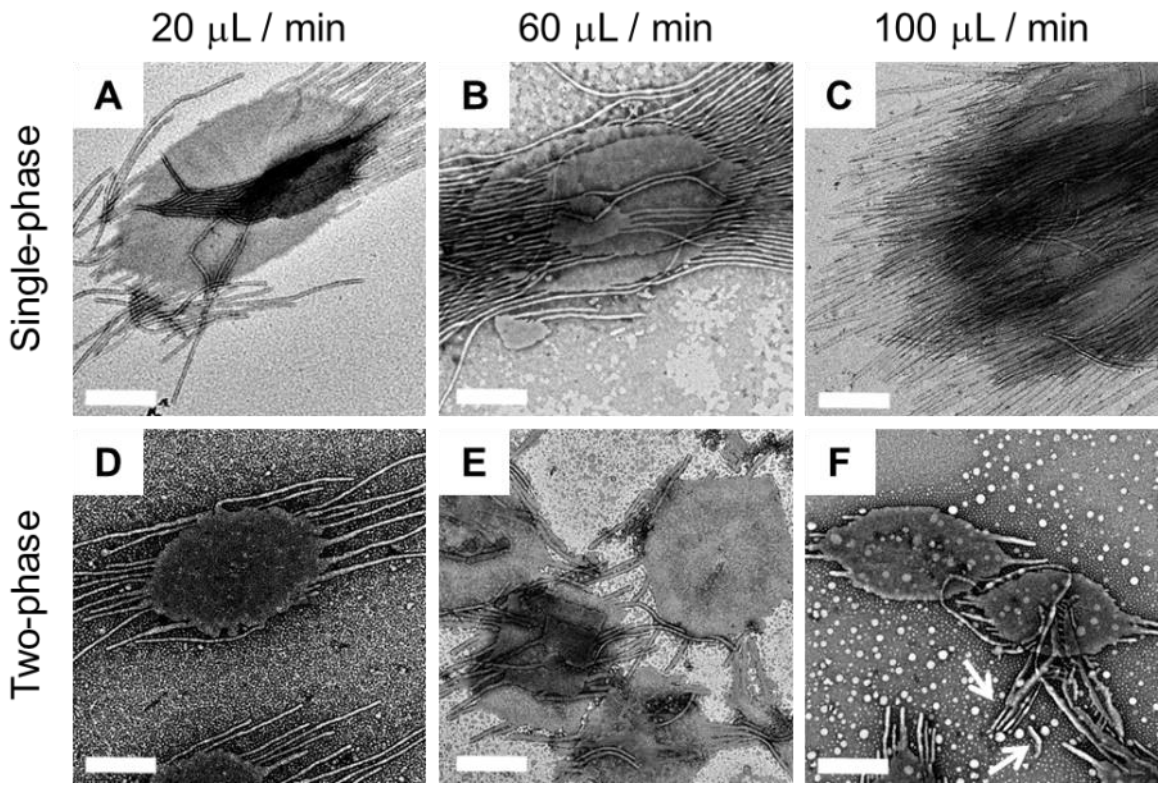

Figure 3-3. Effect of single-phase and two-phase microfluidic reactors on PCL-5k nanoparticle morphology through TEM. Scale bars are 400 nm. White arrows show individual cylinders.

3.3.2. Effect of Reactor Type and On-Chip Flow Rate on Nanoparticle Morphology

The effect of flow rate of both microfluidic reactors on nanoparticle structure was then evaluated. TEM images of PCL-5k nanoparticles formed in the two types of reactors at various flow rates are shown in Figure 3-3. In the single-phase reactor, nanoparticles formed at all flow rates had similar morphologies, which were lamellae with cylindrical tails (Figure 3-3, A-C). For the two-phase reactor, lamellae were also observed at all flow rates (Figure 3-3, D-F). Lamellae were absent in the bulk sample (Figure 3-2A), suggesting that rapid mixing on-chip has an effect on morphology. However, in the two-phase reactor, at 60 μL/min, shorter cylindrical tails on lamellae were seen (Figure 3-3E)

than at 20 μL/min (Figure 3-3D). Furthermore, at 100 μL/min, a second population of spheres with a diameter of 38 nm were formed (Figure 3-3F). These spheres were much bigger than the co-existing small spheres, and may be attributed to shear-induced breakup of larger aggregates at the highest flow rate. In Figure 3-3F, some individual cylinders were present (white arrows), which may represent broken lamellae turning into cylinders.

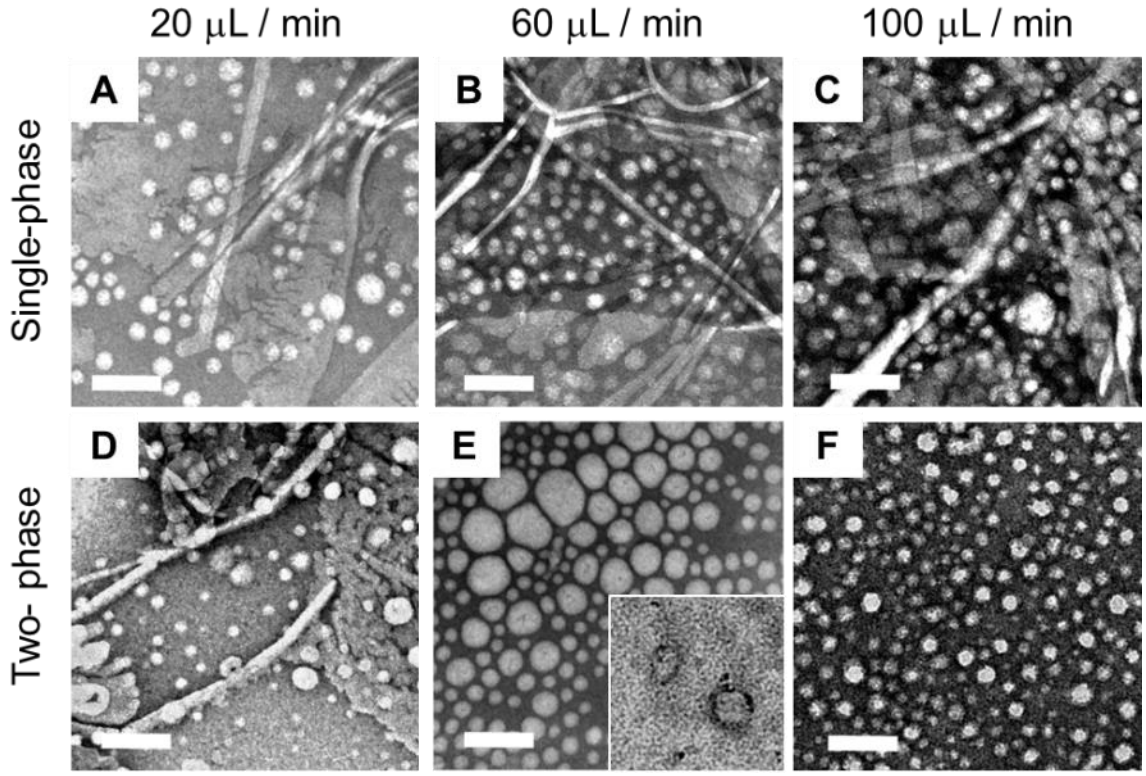

Figure 3-4. Effect of single-phase and two-phase microfluidic reactors on PCL-12k nanoparticle morphology through TEM. Inset to E shows unstained image of vesicles. Scale bars are 200 nm shared among main figures and inset.

TEM images of PCL-12k nanoparticles formed in the two types of reactors at various flow rates are shown in Figure 3-4. In the single-phase reactor, a mixture of spheres, cylinders and lamellae were obtained at all flow rates (Figure 3-4 A, B, C). Again, those morphologies were similar so it can be concluded that flow rate doesn't have an effect on morphologies of PCL-12k nanoparticles in the single-phase reactor. In

contrast, the two-phase reactor formed a mixture of morphologies at 20 μL/min (Figure 3-4D), while at 60 μL/min, only vesicles and spheres were formed (Figure 3-4E). Vesicular walls and lumens were seen from the unstained images, confirming the existence of vesicles. At 100 μL/min, pure sphere about 32 nm in diameter appeared. We notice that both reactors formed different morphologies of PCL-12 nanoparticles than those formed in the bulk (Figure 3-2B), suggesting the effect of rapid mixing.

The two-phase reactor can reach a maximum shear rate of 10^5 s^{-1} at "hot spots" in the channel. Shear rate has a linear relationship with flow rate.[24] For nanoparticles of both copolymers formed in the two-phase reactor, shear-induced coalescence was demonstrated at the lower flow rates that larger aggregates were formed by comparison with the bulk control. In the meantime, shear-induced breakup was supported by the formation of smaller aggregates at high flow rates. In contrast, the wall shear rate of 800 s^{-1} on a similar herringbone single-phase microfluidic reactor was reported in literature.[13] Accordingly, single-phase reactor didn't show any control of morphology by changing the flow rate. The different effect on morphology on these two reactors is mainly attributed to the great gap between shear rates. In the single-phase reactor, structures were still distinct from bulk control probably because of rapid mixing. However, the low shear rate on the single-phase chip was unable to further induce interparticle coalescence or break up of nanoparticles.

3.3.3. Effect of Reactor Type and On-Chip Flow Rate on Nanoparticle Crystallinity

The effect of flow rate on core crystallinity of PCL-12k on two-phase microfluidic reactor was previously reported.[21] PCL crystallinity is defined as weight of crystallized PCL over weight of polymer. The relative PCL crystallinities of PCL-5k and PCL-12k

nanoparticles formed in the bulk and in both reactors calculated from XRD are shown in Figure 3-5. The higher PCL content of PCL-12k led to a higher crystallinity than PCL-5k (Figure 3-5, A, B). For PCL-5k, an increase of crystallinity was observed in two-phase reactor and it appears to have a linear relationship with flow rate assuming the bulk preparation was zero flow (Figure 3-5A). PCL-5k Nanoparticles formed on single-phase reactor had the same PCL crystallinity in the bulk or at any flow rate (Figure 3-5A). In other word, core crystallinity is not dependent of flow rate in the single-phase reactor. The same trend was observed for PCL-12k (Figure 3-5B).

We have already discussed shear effect on bulk crystallization (melt state). On a microfluidic reactor, when nanoparticles moved to high shear region of the chip, shear initialized chain packing and enhanced nucleation. As the nanoparticles recirculate in the processing chip, nucleation is promoted by shear-induced deformation of nanoparticles resulting in a raised crystallinity. Moreover, the hydrophobic core is transferred to melt state by self-assembly, so the factors that affect crystallization are similar to that in melt state.[21] Since single-phase reactor doesn't provide such high shear regions, the nucleation process is comparable to that of bulk micellization, so a similar crystallinity to the bulk control was observed.

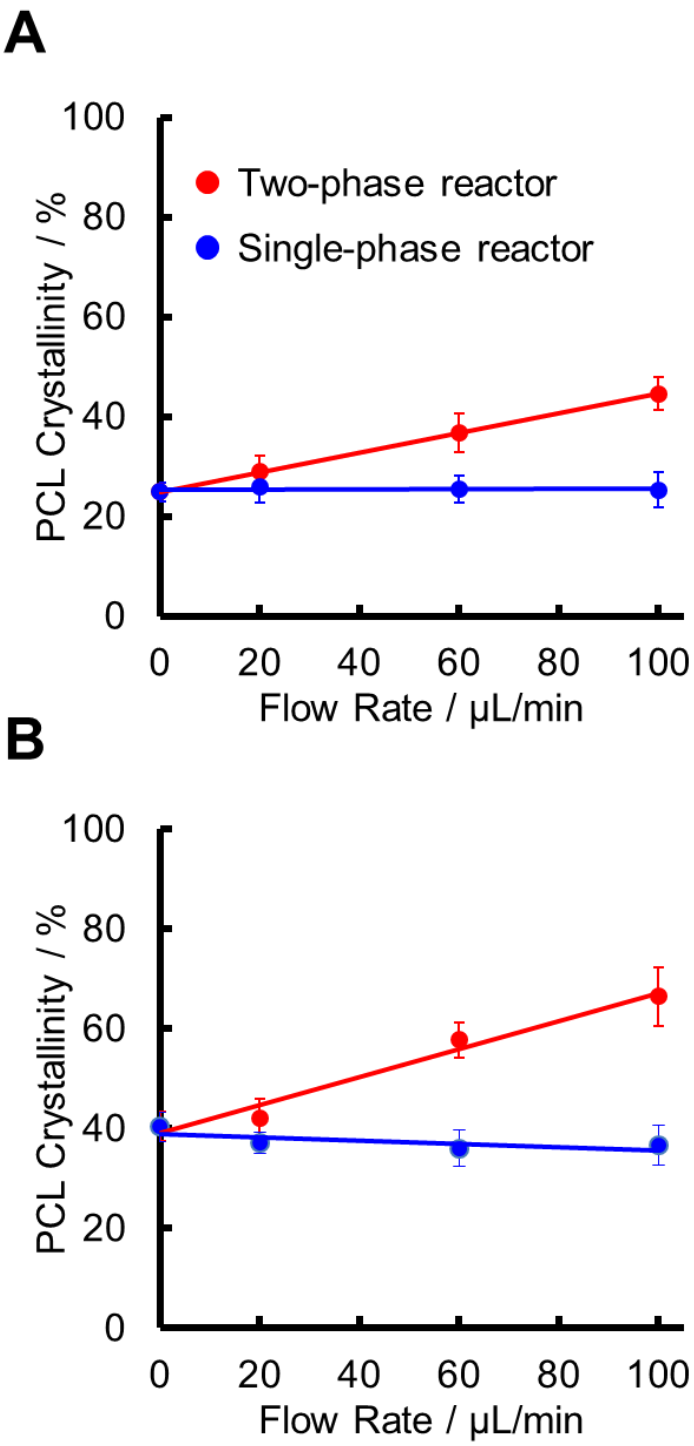

Figure 3-5. Effect of single-phase and two-phase microfluidic reactors on PCL crystallinity of PCL-5k (A) and PCL-12k (B) nanoparticle prepared in the bulk (flow rate = 0 data points) and in the single-phase and two-phase reactors at various flow rates. Errors are standard deviations of mean values determined for three separate preparations.

3.4. Conclusion

This chapter investigated the morphologies and core crystallinities of semicrystalline PCL-*b*-PEO nanoparticles synthesized on single-phase and two-phase microfluidic reactors. Two-phase reactor features flow-dependent high shear regions, which distinguishes it from the single-phase reactor. Maximum shear rate on-chip has a linear relationship with flow rate.

A more effective, precise and unique morphological control was achieved on the two-phase microfluidic reactor. No obvious dependence of flow rate on structure was observed for single-phase reactor, but lower curvature and polydispersed structures than the bulk were made. An increased PCL crystallinity with flow rate was observed for the nanoparticles processed through two-phase reactor, while various flow rates on single-phase chip weren't able to change crystallinity.

First of all, the fascinating and unique morphological control on the gas-liquid segmented microfluidic reactor is likely a shear effect, since it was not observed in low shear rate single-phase reactor. Core crystallinity of nanoparticles has a linear relationship with flow rate, so is maximum shear rate in the channels. Therefore increased crystallinity is dependent on shear rate. These results suggest the two-phase reactor offers some advantages in terms of flow control of nanoparticle multiscale structure despite similar rapid mixing effects in both reactor types.

3.5. Supporting Information

Please see Appendix B for supporting information: Data for cwc determination; Table of actual flow conditions.

3.6. References

1. Y. Song, H. Modrow, L. L. Henry, C. K. Saw, E. E. Doomes, V. Palshin, J. Hormes and C. S. S. R. Kumar Microfluidic Synthesis of Cobalt Nanoparticles. *Chemistry of Materials* **2006,** *18*, 2817.

2. K. S. Elvira, X. C. i Solvas, R. C. R. Wootton and A. J. deMello The Past, Present and Potential for Microfluidic Reactor Technology in Chemical Synthesis. *Nat Chem* **2013,** *5*, 905.

3. P. Y. Keng, S. Chen, H. Ding, S. Sadeghi, G. J. Shah, A. Dooraghi, M. E. Phelps, N. Satyamurthy, A. F. Chatziioannou, C.-J. C. Kim and R. M. van Dam Micro-Chemical Synthesis of Molecular Probes on an Electronic Microfluidic Device. *Proceedings of the National Academy of Sciences* **2012,** *109*, 690.

4. J.-M. Lim, N. Bertrand, P. M. Valencia, M. Rhee, R. Langer, S. Jon, O. C. Farokhzad and R. Karnik Parallel Microfluidic Synthesis of Size-Tunable Polymeric Nanoparticles Using 3d Flow Focusing Towards in Vivo Study. *Nanomedicine: Nanotechnology, Biology and Medicine* **2014,** *10*, 401.

5. S. Yang, F. Guo, B. Kiraly, X. Mao, M. Lu, K. W. Leong and T. J. Huang Microfluidic Synthesis of Multifunctional Janus Particles for Biomedical Applications. *Lab on a Chip* **2012,** *12*, 2097.

6. R. R. Hood, W. N. Vreeland and D. L. DeVoe Microfluidic Remote Loading for Rapid Single-Step Liposomal Drug Preparation. *Lab on a Chip* **2014,** *14*, 3359.

7. A. D. Stroock, S. K. Dertinger, G. M. Whitesides and A. Ajdari Patterning Flows Using Grooved Surfaces. *Analytical Chemistry* **2002,** *74*, 5306.

8. A. D. Stroock, S. K. W. Dertinger, A. Ajdari, I. Mezić, H. A. Stone and G. M. Whitesides Chaotic Mixer for Microchannels. *Science* **2002,** *295*, 647.

9. A. D. Stroock and G. J. McGraw Investigation of the Staggered Herringbone Mixer with a Simple Analytical Model. *Philosophical Transactions of the Royal Society of London A: Mathematical, Physical and Engineering Sciences* **2004,** *362*, 971.

10. C. F. Chen, C. F. Kung, H. C. Chen, C. C. Chu, C. C. Chang and F. G. Tseng A Microfluidic Nanoliter Mixer with Optimized Grooved Structures Driven by Capillary Pumping. *Journal of Micromechanics and Microengineering* **2006,** *16*, 1358.

11. W. Hengzi, I. Pio, H. Erol and M. Syed Numerical Investigation of Mixing in Microchannels with Patterned Grooves. *Journal of Micromechanics and Microengineering* **2003,** *13*, 801.

12. J. P. B. Howell, D. R. Mott, S. Fertig, C. R. Kaplan, J. P. Golden, E. S. Oran and F. S. Ligler A Microfluidic Mixer with Grooves Placed on the Top and Bottom of the Channel. *Lab on a Chip* **2005,** *5*, 524.

13. M. Lopez and M. D. Graham Enhancement of Mixing and Adsorption in Microfluidic Devices by Shear-Induced Diffusion and Topography-Induced Secondary Flow. *Physics of Fluids* **2008,** *20*, 053304.

14. I. V. Zhigaltsev, N. Belliveau, I. Hafez, A. K. K. Leung, J. Huft, C. Hansen and P. R. Cullis Bottom-up Design and Synthesis of Limit Size Lipid Nanoparticle Systems with Aqueous and Triglyceride Cores Using Millisecond Microfluidic Mixing. *Langmuir* **2012,** *28*, 3633.

15. N. M. Belliveau, J. Huft, P. J. C. Lin, S. Chen, A. K. K. Leung, T. J. Leaver, A. W. Wild, J. B. Lee, R. J. Taylor, Y. K. Tam, C. L. Hansen and P. R. Cullis Microfluidic Synthesis of Highly Potent Limit-Size Lipid Nanoparticles for in Vivo Delivery of Sirna. *Mol Ther Nucleic Acids* **2012,** *1*, e37.

16. E. Kastner, R. Kaur, D. Lowry, B. Moghaddam, A. Wilkinson and Y. Perrie High-Throughput Manufacturing of Size-Tuned Liposomes by a New Microfluidics Method Using Enhanced Statistical Tools for Characterization. *International Journal of Pharmaceutics* **2014,** *477*, 361.

17. H. Song, D. L. Chen and R. F. Ismagilov Reactions in Droplets in Microfluidic Channels. *Angewandte Chemie International Edition* **2006,** *45*, 7336.

18. A. Gunther, S. A. Khan, M. Thalmann, F. Trachsel and K. F. Jensen Transport and Reaction in Microscale Segmented Gas-Liquid Flow. *Lab on a Chip* **2004,** *4*, 278.

19. C.-W. Wang, D. Sinton and M. G. Moffitt Flow-Directed Block Copolymer Micelle Morphologies Via Microfluidic Self-Assembly. *Journal of the American Chemical Society* **2011,** *133*, 18853.

20. K. S. Krishna, Y. Li, S. Li and C. S. S. R. Kumar Lab-on-a-Chip Synthesis of Inorganic Nanomaterials and Quantum Dots for Biomedical Applications. *Advanced Drug Delivery Reviews* **2013,** *65*, 1470.

21. A. Bains, Y. Cao and M. G. Moffitt Multiscale Control of Hierarchical Structure in Crystalline Block Copolymer Nanoparticles Using Microfluidics. *Macromolecular Rapid Communications* **2015**, n/a.

22. C.-W. Wang, D. Sinton and M. G. Moffitt Morphological Control Via Chemical and Shear Forces in Block Copolymer Self-Assembly in the Lab-on-Chip. *ACS Nano* **2013,** *7*, 1424.

23. C.-W. Wang, A. Bains, D. Sinton and M. G. Moffitt Flow-Directed Assembly of Block Copolymer Vesicles in the Lab-on-a-Chip. *Langmuir* **2012,** *28*, 15756.

24. G. Schabas, C.-W. Wang, A. Oskooei, H. Yusuf, M. G. Moffitt and D. Sinton Formation and Shear-Induced Processing of Quantum Dot Colloidal Assemblies in a Multiphase Microfluidic Chip. *Langmuir* **2008,** *24*, 10596.

25. R. H. Somani, B. S. Hsiao, A. Nogales, S. Srinivas, A. H. Tsou, I. Sics, F. J. Balta-Calleja and T. A. Ezquerra Structure Development During Shear Flow-Induced Crystallization of I-Pp: In-Situ Small-Angle X-Ray Scattering Study. *Macromolecules* **2000,** *33*, 9385.

26. N.-V. Cuong, M.-F. Hsieh, Y.-T. Chen and I. Liau Synthesis and Characterization of Peg–Pcl–Peg Triblock Copolymers as Carriers of Doxorubicin for the Treatment of Breast Cancer. *Journal of Applied Polymer Science* **2010,** *117*, 3694.

27. T. Azzam and A. Eisenberg Control of Vesicular Morphologies through Hydrophobic Block Length. *Angewandte Chemie International Edition* **2006,** *45*, 7443.

28. G. Rizis, T. G. M. van de Ven and A. Eisenberg Crystallinity-Driven Morphological Ripening Processes for Poly(Ethylene Oxide)-Block-Polycaprolactone Micelles in Water. *Soft Matter* **2014,** *10*, 2825.

Chapter 4.

Paclitaxel-Loaded Block Copolymer Drug Delivery Nanoparticles Synthesized Using Microfluidics: Combining Chemical and Shear Control of Structure and Function

4.1. Introduction

As mentioned in previous chapters, there is tremendous interest in the application of polymeric nanoparticles for the encapsulation and delivery of hydrophobic compounds. The use of polymers for drug delivery has numerous benefits, such as enhanced drug solubilization,[1-3] controlled release of drug,[4-7] lower cytotoxicity,[8, 9] and targeting specific site by ligand modification.[10-12]

As discussed in Chapter 1, PCL-*b*-PEO nanoparticles, with the advantage of biocompatibility and biodegradability, have been studied extensively in this respect. A semicrystalline and hydrophobic core-forming block like PCL is considered to have higher kinetic stability.[13-15] Furthermore, enhanced pharmacokinetics[16, 17] was observed from *in vivo* studies compared to free drugs. Long blood circulation time[18, 19] without accumulation in kidney and liver was demonstrated for some formulations/morphologies,[18, 19] which enables passive targeting to cancer tissues through the enhanced permeation and retention (EPR) effect. EPR effect is that small nanoparticles, which are a few nanometers in diameter, tend to accumulate more in tumor tissues than in normal tissues.

Recent results from our group showed that shear effects using microfluidics offer control of PCL-*b*-PEO nanoparticle size, morphology and core crystallinity, in addition to the delivery function (loading and release of hydrophobic cargo) of the resulting

nanoparticles. For instance, loading efficiency of drugs in nanoparticles increased with flow rate. Due to the on-chip control of crystallinity, morphology and mixing, slower release compared to nanoparticles prepared using conventional bulk synthesis was achieved by increasing flow rate.[20]

In contrast to PCL, poly(methyl caprolactone) is an amorphous polymer, whose glass transition temperature is about -68 °C.[21] Due to the additional methyl group, it is also more hydrophobic than PCL. The synthesis of poly(4-methyl-ε-caprolactone) (4-PMCL) by ring-opening polymerization and its copolymerization has been studied by several groups,[21-23] but the synthesis of poly(6-methyl-ε-caprolactone) (6-PMCL) is less common.[24] The self-assembly of 4-PMCL-*b*-PEO by thin-film hydration was investigated by Zupancich and coworkers. Since PMCL is hydrophobic, addition of the hydrophilic PEO block makes the resulting copolymer amphiphilic. By increasing the PMCL:PEO ratio they were able to make morphologies from spheres to cylinders to vesicles.[22] However, copolymerization of MCL and CL within a diblock copolymer containing PEO has not yet been explored in the literature. Since PMCL is more hydrophobic than PCL, higher loading efficiency of hydrophobic drug is expected. The decrease in crystallinity also allows faster diffusion of drug into nanoparticles.

The hydrophobic drug employed in this study is paclitaxel (PAX). PAX is an anticancer drug, which has very low solubility in water (0.30 μg/mL).[25] PAX is commercially formulated as Taxol™ using Cremophor® EL as vehicle in ethanol at a concentration of 6 mg/mL. However, Cremophor® EL is associated with anaphylactoid hypersensitivity reactions.[26] Minor reactions occur in more than 40% of all patients and

major reaction in 1.5-3% of patients.[27, 28] Therefore, there have been lots of efforts in the drug delivery area to find a safe, efficient vehicle for PAX.

In this study, we used block copolymers synthesized by Dr. Changhai Lu in the Moffitt group, consisting of PEO as the hydrophilic block and a random copolymer of MCL and CL with different MCL:CL ratios as the hydrophobic block, P(MCL-*co*-CL)-*b*-PEO. The introduction of controlled amounts of methylation in the hydrophobic block provides a chemical handle on the crystallinity of the core, which we combine with the top-down handle of flow-directed control through microfluidic self-assembly. We find that copolymerization of CL with MCL affected morphology of nanoparticles and provided higher loading efficiencies and slower release of PAX. Although on-chip shear rate did not have a strong effect on the structure of P(MCL-*co*-CL)-*b*-PEO nanoparticles, we do find slower PAX release for nanoparticles formed on-chip compared to nanoparticles formed in the bulk; we attribute this to more homogeneous distribution of PAX in the core due to faster mixing in the microfluidic environment.

4.2. Experimental

Materials. 2-Methylcyclohexanon (99.0%), $KHSO_5$, sodium bicarbonate (99.0%), calcium hydride (95%), stannous octonate (95%), PEG methyl ether (MePEG-OH, MW~5000) and ε-caprolactone (97%) were all purchased from Sigma-Aldrich and used for synthesis of copolymers. NaCl (Bio Basic Canada, 99.9%), KCl (Caledon, 99.0%), Na_2HPO_4 (Bio Basic Canada, 98.0%) and KH_2PO_4 (Caledon, 99.0%) were used to prepare phosphate buffered saline (PBS, pH=7.4). Methanol (Fisher Chemical, 99.9%), methylene chloride (Fisher Chemical, 99.9%), toluene (Caledon, 99.5%), ethyl ether (VWR, 99%), dimethylformamide (DMF, Caledon, 99.8%), acetonitrile (ACN, Caledon,

HPLC grade), *t*-butyl methyl ether (Sigma-Aldrich, HPLC grade) and dichloromethane (DCM, EMD, HPLC grade) were used as received without further purification. Paclitaxel (99.0%) was purchased from Polymed Inc.

Synthesis of 6-methyl-*ε*-caprolactone (MCL). To a 100 mL round-bottom flask 2-methylcyclohexanone (0.721 g), methanol (20 mL), water (20 mL), and sodium bicarbonate (3 g) were added. The vessel was vigorously stirred with a Teflon-coated magnetic stir bar. Oxone (4 g) was added in two portions—the second added 10 min after the first. After the addition of Oxone (ca. 2 equiv of $KHSO_5$) vigorous gas evolution occurred over 20 min, abated, and ceased after ~1 h. The reaction was allowed to stir for 6 h followed by filtration and was then extracted with methylene chloride. The organic phase was concentrated under vacuum. A total of 0.82 g was recovered for a quantitative yield. The monomer was purified by fractional vacuum distillation (the distillate temperature was 55 °C at 0.98 Torr) from calcium hydride and stored over 3Å-activated molecular sieves. Additional purification of 6-methyl-ε-caprolactone was needed to produce monomodal high molecular weight PMCL by passing the distilled monomer through a column of activated alumina under nitrogen.

Synthesis of P(MCL-*co*-CL)-*b*-PEO Copolymers. The copolymers of P(MCL-*co*-CL)-*b*-PEO with different ratios of *ε*-caprolactone (CL) and 6-methyl-*ε*-caprolactone (MCL) were synthesized *via* ring opening polymerization of *ε*-CL and *ε*-MCL in the presence of MePEG-OH as the macroinitiator and stannous octonate ($Sn(Oct)_2$) as the catalyst. The polymerization was carried out under a nitrogen atmosphere in a flame-dried round-bottom flask equipped with a magnetic stir bar. In brief, following azeotropic distillation in toluene, MePEG-OH (5 g, 1 mmol) was dissolved in a 75 ml volume of

dried toluene, CL (3.63 g, 31.8 mmol) and MCL (1.36 g, 10.63 mmol) and the determined mass of $Sn(Oct)_2$ were added to the reaction vessel. The polymerization was carried out at 110 °C for 24 hrs with continuous stirring. The copolymers were isolated by precipitation in cold ether and dried under vacuum. The copolymers were then characterized by ^{1}H-NMR and GPC. By changing the feed ratio of MCL and CL, copolymers with different MCL:CL ratios were synthesized. The molecular weight and MCL fraction, defined as number-averaged weight of MCL in a copolymer chain over number averaged weight of hydrophobic block, was calculated from ^{1}H-NMR spectra. GPC characterization was done by Advanced Polymer Materials Inc. with chloroform as eluent and a series of PEO as standards. GPC traces are shown in Figure S4-1. PDI was calculated by M_n from NMR and M_w from GPC. Copolymers are named as PMCL-0, PMCL-25, PMCL-50, PMCL-75, PMCL-100 and tabulated in Table 4-1.

Critical Water Content (cwc) Determination. Critical water contents were determined for solutions of the various copolymers in DMF at an initial copolymer concentration of 0.33 wt %, by dropwise water addition and static light intensity measurement. Methods and conditions were the same as those described in Chapter 2 for cwc determinations. Titration curves are shown in Figure S4-2. Results are tabulated in Table 4-1, errors were determined from the standard deviation of three separate solution preparations and measurements.

Bulk Preparation of PAX-Loaded P(MCL-*co*-CL)-*b*-PEO Nanoparticles. Nanoparticles of each block copolymer containing various quantities of PAX were formed by the conventional method of dropwise water addition. For these experiments, 3 g of 0.33 wt % copolymer solutions in DMF with various PAX/polymer (w/w) loading

ratio *r* (*r* = 0, 0.10, 0.25 and 0.50) were prepared and equilibrated overnight. Deionized water was added dropwise at a rate of 80 µL/min to a target water content of cwc + 10 wt % using syringe pump with moderate stirring. After reaching the target water content, nanoparticles were immediately quenched into a 10 × excess (by volume) of deionized water, followed by 12-hour dialysis (6-8 kD MWCO dialysis membrane, Spectrum Laboratories) against deionized water.

Microfluidic Reactor Fabrication. Negative masters were fabricated on silicon wafers (Silicon Materials) using the negative photoresist SU-8 100 (Microchem). A 150 µm-thick SU-8 film was spin-coated at 2000 rpm onto the silicon wafer and heated at 65 °C for 12 min and then at 95 °C for 50 min. After the wafer was cooled, a photomask was placed directly above and the wafer was exposed to UV light for 100 s. Then, the UV-treated film was heated at 65 °C for 1 min and then 95 °C for 20 min. Finally, the silicon wafer was submerged in SU-8 developer (Microchem) and rinsed with isopropanol until all unexposed photoresist was removed.

Microfluidics chips were fabricated from poly(dimethyl siloxane) (PDMS) using a SYLGARD 184 silicon elastomer kit (Dow Corning). For fabrication of all PDMS chips, the elastomer and curing agent were mixed at a 7:1 ratio and degassed under vacuum. The resulting mixture was poured over a clean negative master chip in a Petri dish and further degassed until all remaining air bubbles were removed. The PDMS was heated at 85 °C until cured (~20 min), and then peeled from the negative master; holes were punched through the reservoirs of the resulting PDMS chip to allow for the insertion of tubing. A thin PDMS film (substrate layer) was also made on a glass slide by spin-coating a 20:1 elastomer / curing agent mixture followed by curing. The substrate layer

was then permanently bonded to the base of the microfluidic reactor (channel layer) after both components were exposed to oxygen plasma for 45 s. The resulting reactor has a set channel depth of 150 μm and consists of a sinusoidal mixing channel 100 μm wide and a sinusoidal processing channel 200 μm wide, exactly the same as the one used previously in Chapter 2 and 3.

Flow Delivery and Control. Pressure-driven flow of liquids to the reactor inlet was provided using 1 mL gastight syringes (Hamilton, Reno, NV) mounted on syringe pumps (Harvard Apparatus, Holliston, MA). The microfluidic chip was connected to the liquid syringes via 1/16th-inch (OD) Teflon tubing (Scientific Products and Equipment, ON). Gas flow was introduced to the chip via an Ar tank regulator and a downstream regulator (Johnston Controls) for fine adjustments. The chip was connected to the downstream regulator through a 1/16th-inch (OD) / 100-μm (ID) Teflon tube (Upchurch Scientific, Oak Harbor, WA). The liquid flow rate (Q_{liq}) was programmed via the syringe pumps and the gas flow rate (Q_{gas}) was fine-tuned via the downstream pressure regulator in order to set the nominal total flow rates of 50, 100 and 200 μL/min described in the main text. For all experiments, the relative gas-to-liquid flow ratio, Q_{gas}/Q_{liq} ~1.

Microfluidic Preparation of PAX-Loaded P(MCL-*co*-CL)-*b*-PEO Nanoparticles. For microfluidic preparation of nanoparticles, the following three fluid streams were combined to form gas-segmented liquid plugs within the reactor: (1) 1.0 wt % P(MCL-*co*-CL)-*b*-PEO solution in DMF with PAX/polymer loading ratio r = 0.25, (2) pure DMF, and (3) DMF/water. The flow rates of the three liquid streams were equal for all runs and the water content of the DMF/water stream was selected to yield a steady

state on-chip copolymer concentrations of 0.33 wt % and a steady-state water content of cwc + 10.0 wt % for each copolymer.

For each nanoparticle preparation, sample was collected from the chip into empty vials; the resulting nanoparticles in DMF/water were designated “unquenched” and were analyzed immediately by TEM. In addition, sample was collected into a vial containing a 10 × excess by volume of deionized water, followed by 12-hour dialysis (6-8 kD MWCO dialysis membrane, Spectrum Laboratories) against deionized water; the resulting nanoparticles were designated “dialyzed”.

Transmission Electron Microscopy. The instrumentation and methods were the same as those described in Chapter 2. Negatively-stained samples for TEM imaging were prepared by depositing a drop of block copolymer nanoparticle dispersion on a carbon-coated 300-mesh copper TEM grid followed by a drop of 1 wt % uranyl acetate aqueous solution as a negative staining agent. Excess liquid was immediately removed using lens paper, followed by drying of the remaining liquid under ambient conditions.

For each copolymer and flow condition, morphologies and mean nanoparticle sizes were determined based on triplicate preparations; for each preparation, morphology and size analysis was carried out using at least three images taken in different regions of the grid. Mean dimensions for each condition were determined from a total of 450 spheres and/or 150 cylinders. Identified morphologies and mean dimensions for each copolymer and preparation condition are reported in Table 4-2 for bulk preparations and Table 4-7 for on-chip preparations. Averaging and statistical analysis of dimensions from TEM images were conducted using Image J software.

Dynamic Light Scattering. Effective hydrodynamic diameters of PAX-loaded nanoparticles were determined using dynamic light scattering (DLS). DLS measurements were carried out using a Brookhaven Instruments Zeta-Pals Analyzer equipped with a solid state Laser (660 nm) with a maximum power output of 35 mW. All DLS measurements of PAX-loaded nanoparticles were performed in pure water and an experimental temperature of 25˚C and at a scattering angle of 90˚.

After overnight dialysis against deionized water to remove residual DMF and unencapsulated PAX, PAX-loaded nanoparticles were transferred to pre-cleaned polystyrene cuvettes, and then diluted with deionized water filtered through two nylon syringe filters in series with nominal pore sizes of 0.2 μm (National Scientific Company) if necessary. Results are tabulated in Table 4-2 for bulk preparations and Table 4-6 for on-chip preparations. For each nanoparticle preparation, mean effective hydrodynamic sizes were determined from three measurements of the autocorrelation function using cumulent analysis.

X-Ray Diffraction. For XRD sample preparation, solvent was removed from dialyzed nanoparticles in water by rotary evaporation at 25 °C until solid films were obtained. The resulting films were then scraped as a powder onto the XRD specimen holder. Instrumentation setting and peak deconvolution were the same as those described in Chapter 3.

Paclitaxel Loading Efficiency Determination. PAX loading efficiencies of PAX-loaded nanoparticles were determined by high performance liquid chromatography- mass spectromethy (HPLC-MS). First, precipitate of unencapsulated drug in dialyzed samples was removed by centrifuging at 16000 g for 10 minutes. Then, water was removed from

~2 g of a gravimetrically-determined mass of dialyzed PAX-loaded nanoparticles by rotary evaporation at 25 °C; then ~0.2 g of a gravimetrically determined mass of ACN was added to the resulting solid and the mixture was vortexed for 2 min to ensure complete dissolution of drug. HPLC-MS (Ultimate 3000, Thermo Scientific) with a C18 column (Phenomenex Luna 5u C18), a constant eluent composition of 65/35 acetonitrile/water (v/v) with 1 v % formic acid, and a diode array detector (DAD) set at 227 nm, was then used to quantify the concentration of drug in the resulting solutions. Sample injection volumes were 50 μL and the flow rate was 1 mL/min. A calibration curve (Figure S4-3) for the DAD was generated by analysis of 7 standards containing different known PAX concentrations in ACN. Quantities of PAX in the various dissolved nanoparticle solutions were determined and loading efficiencies and loading levels were calculated for each sample using the following equations:

$$loading\ efficiency\ (\%) = \frac{mass\ of\ encapsulated\ PAX\ (g)}{total\ PAX\ used\ (g)} \times 100\% \quad (4\text{-}1)$$

$$loading\ level\ \left(\frac{w}{w}\right) = \frac{mass\ of\ encapsulated\ PAX\ (g)}{mass\ of\ copolymer\ (g)} \quad (4\text{-}2)$$

$$loading\ level\left(\frac{w}{w}\right) = loading\ efficiency\ (\%) \times loading\ ratio\ (r, w/w) \quad (4\text{-}3)$$

***In Vitro* PAX Release Kinetics.** Experiments were carried out to monitor the *in vitro* release of PAX from PAX-loaded nanoparticles using HPLC-MS. In a typical experiment, after centrifugation to remove precipitated drug, 2 g of dialyzed PAX-loaded nanoparticles were transferred to a 5 mL Float-A-Lyzer tube (SpectrumLabs, MWCO 100 kDa) for each predetermined time. These tubes were then placed in a 5 L-beaker of the release medium, consisting of ~4 L of PBS; throughout release experiments, the release medium was constantly stirred using magnetic stirring and maintained at

physiological temperature (37 °C), and was changed every 2 days. At each predetermined time (*t* = 1, 2, 4, 8, 24, 72 and 96 h), the solution of a tube was transferred to a vial and then dried by rotary evaporation at 25 °C. After that 0.2 g ACN was added. The resulting solution was decanted into a vial and injected into the HPLC-MS and PAX was detected by DAD. Percentages of PAX released were calculated relative to the determined mass of PAX in nanoparticles at the *t* = 0 release time. Reported release percentages at each release time are averages determined from triplicate preparations under the specified conditions. To better highlight differences between the release profiles of the different nanoparticles, only release times up to 8 hours are shown in the Figure 4-5, although the full release profiles, collected over 5 days of PAX release are shown in Appendix C (Figure S4-4).

Monitoring Hydrolytic Degradation of PAX-loaded P(MCL-*co*-CL)-*b*-PEO Nanoparticles during *In Vitro* Release. During the *in vitro* release of PAX into PBS (pH = 7.4, 37°C), aliquots of PAX-loaded nanoparticles were removed at four different release times (*t* = 3, 6, 12, and 24 h) for analysis by DLS, in order to monitor hydrolytic degradation of the nanoparticles.

4.3. Results and Discussion

4.3.1. Characterization of Copolymers

From the ^{1}H NMR spectra (Figure 4-1), number-average molecular weights were determined by measuring the relative intensities of the CL and MCL peaks using the PEO peak (3.65 ppm) as a reference, because the number-average molecular weight of PEO is known (5000 g/mol). When ε-caprolactone and 6-methyl-ε-caprolactone are copolymerized, a decrease in the CL methylene peak at 4.06 ppm, and the appearance of the peak at 1.20 ppm and 4.90 ppm, which correspond to the MCL methyl and the methylene, is observed. The weight fraction of MCL is defined as the weight of MCL over the sum of weight of MCL and CL. The determined fraction of MCL is the same as the feed ratio in synthesis described in experimental. Equations and sample calculation for PMCL-25 are shown below:

$$weight\ of\ CL = \frac{integration\ at\ 4.06\ ppm \times 4 \times M_n(CL) \times M_n(PEO)}{integration\ at\ 3.65\ ppm \times 2 \times M_n(EO)} =$$

$$\frac{63 \times 4 \times 114 g/mol \times 5000 g/mol}{452 \times 2 \times 44 g/mol} = 3830 g/mol \quad (4\text{-}4)$$

$$weight\ of\ MCL = \frac{integration\ at\ 1.20\ ppm \times 4 \times M_n(MCL) \times M_n(PEO)}{integration\ at\ 3.65\ ppm \times 3 \times M_n(EO)} =$$

$$\frac{32 \times 4 \times 128 g/mol \times 5000 g/mol}{452 \times 3 \times 44 g/mol} = 1340 g/mol \quad (4\text{-}5)$$

$$weight\ of\ hydrophobic\ block = weight\ of\ CL + weight\ of\ MCL =$$

$$3830 \frac{g}{mol} + 1340 \frac{g}{mol} = 5170 g/mol \quad (4\text{-}6)$$

$$f_{MCL} = \frac{weight\ of\ MCL}{weight\ of\ hydrophobic\ block} = \frac{1340 g}{mol} \Big/ \frac{5170 g}{mol} = 0.259 \quad (4\text{-}7)$$

The cwc values of the various copolymers are tabulated in Table 4-1, based on titration curves shown in Figure S4-2. PMCL-0 has a cwc lower than all of the MCL

containing copolymers, with the cwc increasing as the MCL content of the copolymer increases. With the additional methyl group, PMCL is more hydrophobic than PCL and so on the basis of thermodynamics alone we would expect the cwc to decrease as the MCL content increases, whereas the opposite trend is observed in Table 4-1. This implies that the kinetic effect of decreased rate of crystallization with increase in MCL content is dominant over the thermodynamic driving force to decrease the cwc. This further implies that crystallization is a prominent driving force in the micellization of CL-containing block copolymers.

Table 4-1. Copolymer Characteristics and Critical Water Contents (cwc).

Copolymer	M_n **P(MCL-*co*-CL)-*b*-PEO**[a]	M_n **P(MCL-*co*-CL)**	f_{MCL}	**PDI**[b]	**cwc / wt %**[c]
PMCL-0	9600	4600	0	1.96	7.1 ± 0.1
PMCL-25	10170	5170	0.259	2.55	8.6 ± 0.2
PMCL-50	10100	5100	0.510	1.95	8.8 ± 0.1
PMCL-75	9570	4570	0.734	1.77	9.4 ± 0.3
PMCL-100	9800	4800	1	2.34	9.3 ± 0.2

a) M_n(PEO) = 5000 g/mol.

b) PDI=M_w(GPC)/M_n(NMR)

c) Errors are standard deviation of mean values determined from three separate preparations.

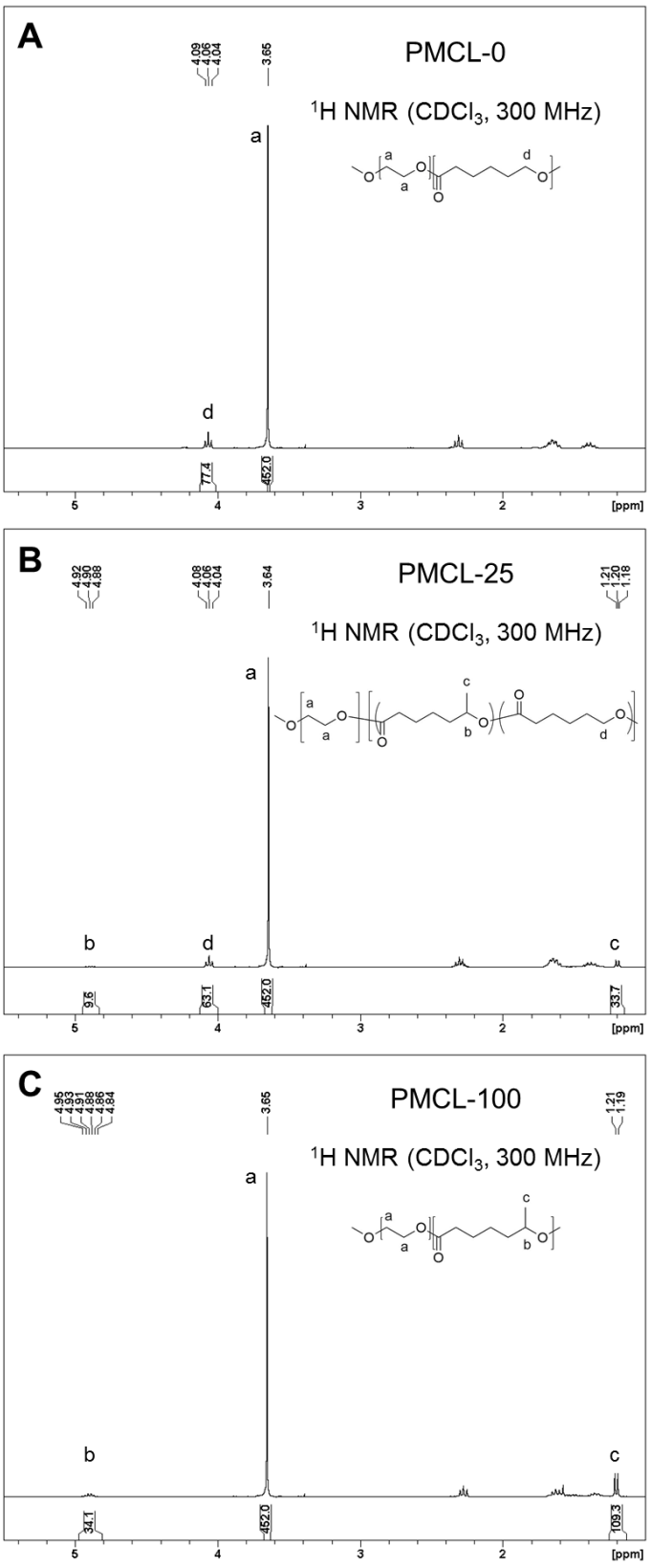

Figure 4-1. ^{1}H NMR spectra of PMCL-0 (A), PMCL-25 (B) and PMCL-100 (C).

4.3.2. Effect of MCL content on the Morphology of Bulk-Prepared Nanoparticles

Nanoparticles of all five copolymers (without PAX) with different MCL contents were first synthesized using the conventional bulk method. The TEM images of bulk-prepared nanoparticles of the five different copolymers are shown in Figure 4-2. The morphologies and characteristic dimensions from TEM and hydrodynamic diameters from DLS are tabulated in Table 4-2.

In the PMCL-0 sample (Figure 4-2A), cylinders were observed along with some small spheres, very similar to its unquenched counterpart described in Chapter 3, indicating that the PCL-*b*-PEO nanoparticles (PMCL-0) are quite stable to quenching, probably due to crystallites in the core acting as physical cross-links. As the MCL content increased to 25 wt % (PMCL-25), we saw a decrease in the size and number of cylinders, as well as an increase in sphere sizes (Figure 4-2B). With a further increase in MCL content (PMCL-50 and PMCL-75) cylinders were no longer formed and we observed pure spheres in these samples (Figure 4-2, C and D, respectively). Finally, in the PMCL-*co*-PEO copolymer sample (MCL-100), a few short rods are once again observed. The initial trend of decreasing number of cylinders with increasing MCL content can be explained by the expected decrease in crystallinity. Winnik group investigated the morphologies prepared from poly(ferrocenylsilane-*b*-dimethylsiloxane) (PFDMS-b-PDMS) by addition of hexane into THF solution, both below and above the PFDMS's T_m. PFDMS is the core-forming block and it is semicrystalline. In addition, crystallization occurred upon micellization under T_m, but not above T_m. They show that cylindrical morphology was observed below T_m, while spheres were observed above T_m, showing that crystallization favours formation of lower curvature morphologies, since these

morphologies allow more efficient packing of polymer chains.[29] However, in the present study, the cause of formation of cylinders in the PMCL-100 sample cannot be associated with core crystallinity. Therefore cylinders in MCL-100 are most likely associated with in increased interfacial tension due to increased hydrophobicity in this sample, and the associated decrease in curvature to relax chain stretching of the core-forming block. This is supported by the fact that the more prominent spheres coexisting with cylinders in PMCL-100 are the largest spheres of all five copolymers and therefore contain the most highly stretched hydrophobic chains (Table 4-2), since the overall degrees of polymerization of the hydrophobic blocks in the five copolymers are about the same (Table 4-1).

Table 4-2. Morphologies[a], Mean Dimensions[b] and Hydrodynamic Diameters for P(MCL-*co*-CL)-*b*-PEO Nanoparticles Prepared in the Bulk

Copolymer	Drug: Polymer Loading Ratio (w/w)	Morphologies and Mean Dimensions (nm)	Hydrodynamic Diameter (nm)
PMCL-0	**0**	S (13 ± 2) C (24 ± 2)	1300 ± 100
	0.10	S (16 ± 1) C (20 ± 3)	1110 ± 90
	0.25	S (13 ± 1) C (23 ± 2)	1080 ± 90
	0.50	S (13 ± 3) C (20 ± 3)	1100 ± 100
PMCL-25	**0**	S (22 ± 2) C (17 ± 2)	230 ± 50
	0.10	S (23 ± 2)	60 ± 10
	0.25	S (24 ± 1)	63 ± 6
	0.50	S (25 ± 4)	65 ± 5

PMCL-50	**0**	S (20 ± 1)	62 ± 9
	0.10	S (21 ± 3)	60 ± 10
	0.25	S (24 ± 2)	60 ± 10
	0.50	S (23 ± 1)	61 ± 8
PMCL-75	**0**	S (23 ± 5)	60 ± 10
	0.10	S (25 ± 3)	60 ± 10
	0.25	S (26 ± 1)	60 ± 10
	0.50	S (23 ± 2)	60 ± 9
PMCL-100	**0**	S (25 ± 1) C (21 ± 4)	210 ± 30
	0.10	S (19 ± 2)	60 ± 10
	0.25	S (22 ± 2)	60 ± 10
	0.50	S (25 ± 3)	61 ± 6

a) Morphologies are indicated as S (spheres) and C (cylinders or rods).

b) Numbers refer to sphere diameters or cylinder widths. Errors for mean dimensions and hydrodynamic diameters are standard deviations of mean values determined for three separate preparations.

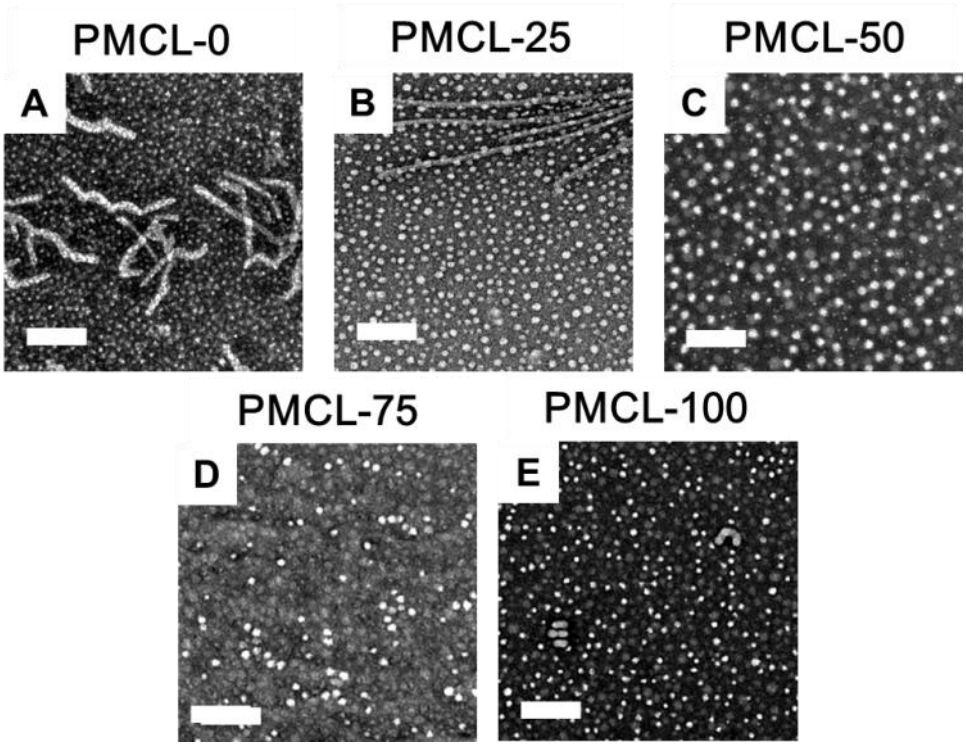

Figure 4-2. Effect of MCL content on P(MCL-*co*-CL)-*b*-PEO nanoparticle morphology through TEM. Scale bars are 200 nm.

4.3.3. Effect of MCL Content on the Crystallinity of Bulk-Prepared Nanoparticles

XRD was then used to probe the internal crystallinity of the nanoparticles shown in Figure 4-2 and these data are presented in Figure 4-3. The XRD pattern for the PCL-*b*-PEO copolymer containing no MCL (PMCL-0, Figure 4-3A) provides a baseline for comparison with the MCL containing copolymers, as the hydrophobic block of this sample is expected to be semicrystalline. In Figure 4-3A, blue line shows PEO peaks and red line shows PCL peaks, while pink line shows the amorphous halo. In contrast, the XRD pattern and the associated peak deconvolution of PMCL-25 (Figure 4-3B) indicates that even with the minimum MCL content in this series, the disappearance of the crystalline PCL peak (2θ=~32°) is observed. In fact, we find no significant difference between the XRD patterns of PMCL-25 (Figure 4-3B) and PMCL-100 (Figure 4-3C). Since the latter nanoparticles are expected to have amorphous cores, this suggest that cores with only 25 wt % MCL are also amorphous, likely due to the disruption of chain packing by methyl groups statistically distributed along the hydrophobic blocks. The resulting trend in core crystallinity versus MCL content is plotted in Figure 4-3D. We note that the absence of crystallinity in all nanoparticle samples containing MCL is further supported by the qualitative mechanical properties of the associated nanoparticle solids (after removal of water) which are sticky at room temperature, compared to the PMCL-0 nanoparticles which were less sticky and more brittle solids.

In a relevant literature, 4-P(MCL-*co*-CL) was synthesized at different ratios.[21] The authors presented DSC heating scans, which show a decrease in melting enthalpy with increasing MCL content. With 25 mol % MCL, the melting range is 10-35 °C, much lower and broader than 50-65 °C for pure PCL. The corresponding wide angle X-ray

diffraction (WAXD) results show a weak PCL peak for 25 mol % MCL but not for any higher MCL contents.

Since PMCL-25 (25 wt % MCL) is similar to 25 mol % MCL in the study discussed above, we can assume PMCL-25 has a similar melting range. For the zero crystallinity we observed in our results, temperature might have played an important role since all experiments and measurements were carried out at room temperature (25 °C), which might be in melting range of the hydrophobic block.

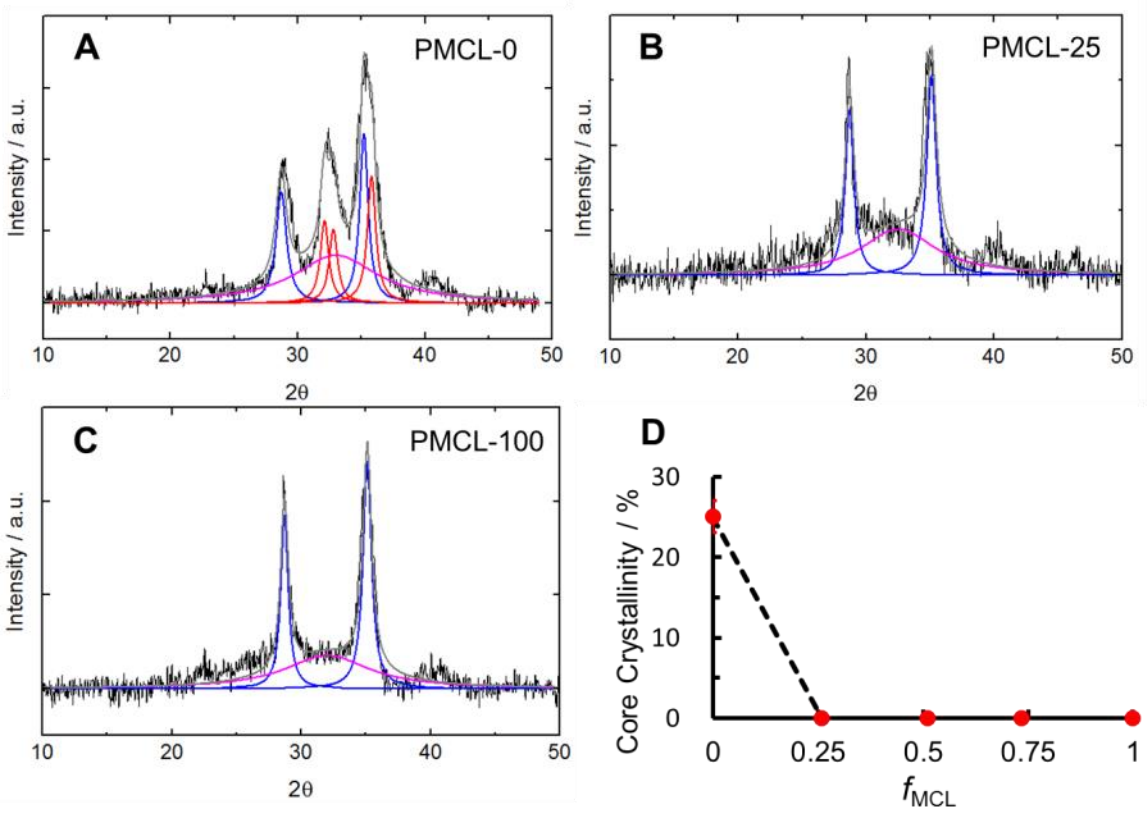

Figure 4-3. XRD patterns and fitting for PMCL-0 (A), PMCL-25 (B) and PMCL-100 (C) nanoparticles prepared in the bulk without paclitaxel encapsulation. Effect of MCL content on crystallinity of core (D). Blue line shows PEO peaks. Red line shows PCL peaks. Pink line shows amorphous region. Errors are standard deviations of mean values determined for three separate preparations.

4.3.4. Effect of PAX Loading on the Morphology of Bulk-Prepared Nanoparticles with Different MCL Contents

Figure 4-4 shows nanoparticle morphologies for the five copolymers (different MCL content) each with various PAX/polymer loading ratios, r = 0, 0.1, 0.25, 0.50. Note that the r = 0 cases are included for comparison and correspond to the nanoparticle samples described in previous sections without loaded PAX. From Figure 4-4, we find that the morphological effect of PAX loading ratio (r) is negligible for the PMCL-0 copolymer, where all loading ratios formed cylinders and spheres (Figure 4-4, A-D) and the characteristic dimensions of both morphologies (w = 20-24 nm for cylinders and d = 13-16 nm for spheres) were constant within experimental error (Table 4-2). However, loading of small amounts of PAX appears to have a more significant morphological effect on nanoparticles in which the hydrophobic cores contain MCL repeat units. For example, as discussed previously, PMCL-25 and PMCL-100 nanoparticle sample both contained small numbers of cylinders in the absence of PAX (r = 0, Figure 4-4, E and Q) but contained only spheres once a small amount of PAX was added (r = 0.1, Figure 4-4, F and R). It seems that loading of PAX prevents the formation of cylinders in MCL-containing copolymers. This may be due to morphological effects of PAX on the interfacial tension and chain stretching within the amorphous cores of MCL-containing nanoparticles which are not observed in the PMCL-0 nanoparticles due to the dominant effects of chain crystallization in that copolymer. Similar to the PMCL-0 nanoparticles, the sphere sizes of the PMCL-25, PMCL-50, PMCL-75, and PMCL-100 nanoparticles were constant with increasing PAX loading ratio within experimental error, although the spheres were larger in the MCL-containing cases, in the range of 20-25 nm compared to

13-16 nm for MCL-0 (Table 4-2). The constant core sizes with increase loading ratio suggests that a significant amount of added PAX at high loading ratios was not successfully encapsulated in the nanoparticles, as discussed in following sections.

Hydrodynamic diameters measured by DLS agree with what is shown by TEM and associated size analysis. All samples containing cylinders had a much higher size, especially for PMCL-0, where cylinders were the major morphology. For samples with pure spheres, the sizes were all around 60 nm. The hydrodynamic diameter was larger than the sphere diameter determined from TEM because TEM analysis includes only the nanoparticle cores, while hydrodynamic diameter includes the swollen PEO coronal chains.

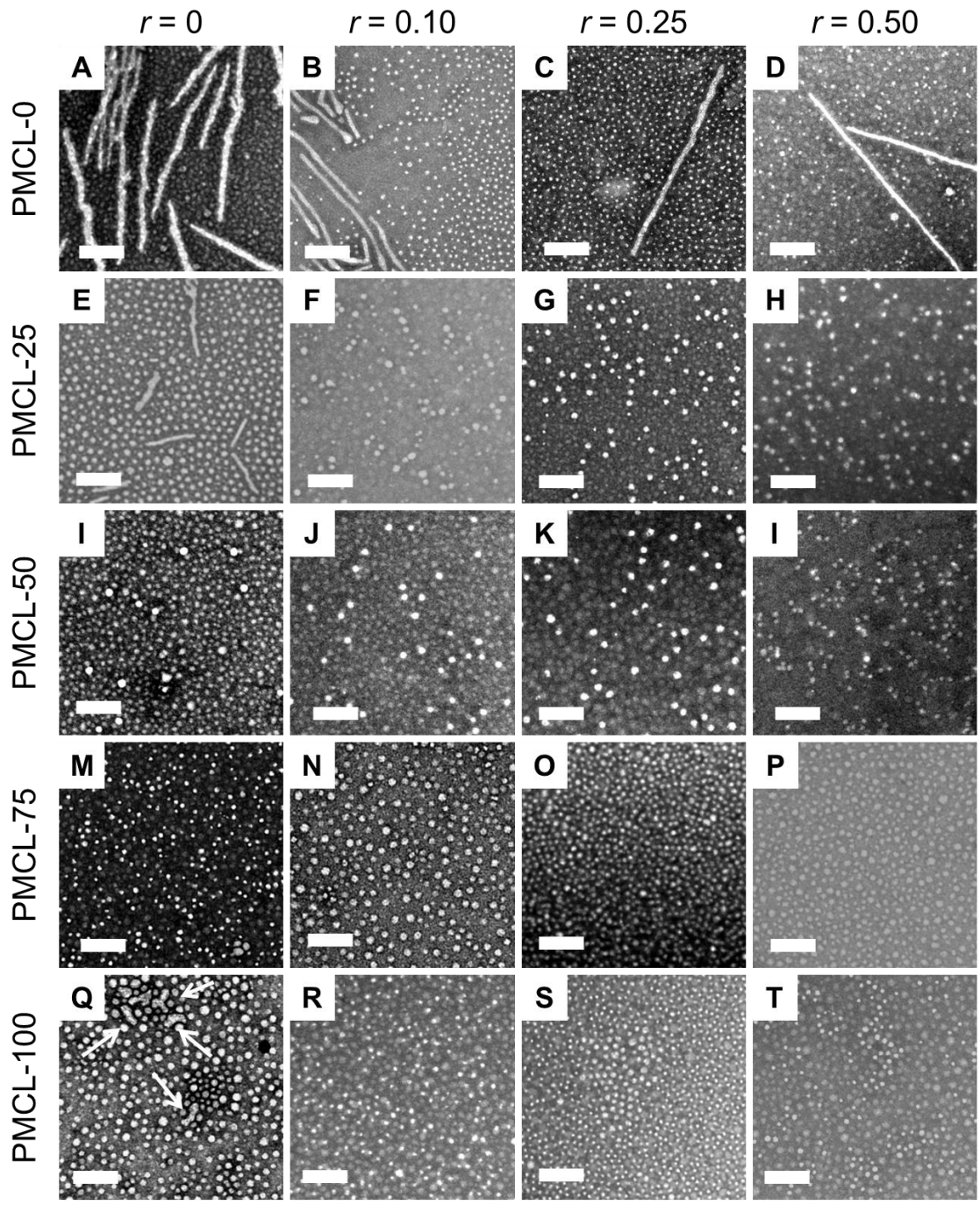

Figure 4-4. Effect of loading ratio (*r*) on P(MCL-*co*-CL)-*b*-PEO nanoparticle morphology through TEM. Scale bars are 200 nm. White arrows point to short cylinders.

4.3.5. Effect of MCL Content on PAX Loading Efficiency of Bulk-Prepared Nanoparticles

PAX loading efficiencies and corresponding loading levels determined with HPLC were determined for the bulk-prepared nanoparticles of the five copolymers (PMCL-0, PMCL-25, PMCL-50, PMCL-75, PMCL-100) at three different loading ratios (r = 0.1, 0.25, 0.50) and are tabulated in Table 4-3. It is evident that for all five copolymers, loading efficiencies decrease with increasing loading ratio, such that the resulting loading levels are constant regardless of loading ratio. A similar loading level of PCL-*b*-PEO of similar molecular weight and composition was found in literature.[30] A possible reason is that the nanoparticle cores are saturated with PAX even when r = 0.1, so further addition of drug does not increase the loading level.

Based on the measured saturated loading levels, we determined that the mole ratio of paclitaxel molecules to copolymer chains within the nanoparticles is ~0.4 for PMCL-0 and ~0.5 for all MCL-containing copolymers. Therefore the saturated loading level of PMCL-0 is lower than that of the MCL-containing copolymers. This difference may in part be attributed to the higher hydrophobicity of the MCL-containing copolymers, leading to a higher solubility of PAX within the nanoparticle cores. However, we note that although PAX solubility is expected to increase monotonically with MCL content, the most hydrophobic copolymer, PMCL-100, did not load any more drug than the least hydrophobic among the MCL-containing copolymers, PMCL-25 (both showed loading levels of ~0.005). This suggests that if the core hydrophobicity effect on loading levels is present, it is not a strong effect. Rather, we note that the step-wise increase in PAX loading level between PMCL-0 and PMCL-25, with no further increase in loading level

between PMCL-25 and PMCL-100, tracks with the corresponding step-wise decrease in core crystallinity from semicrystalline to amorphous. This suggests that the increase in loading level from 0.004 to 0.005 between PMCL-0 and PMCL-25 is mainly due to the corresponding loss of crystallite regions within the core which will exclude PAX due to a combination of thermodynamic and kinetic factors. On one hand, strong favourable interchain interactions compete with the interactions between drug and polymer, thus lowering the solubility of the core of nanoparticles. On the other hand, crystallites make the core more viscous, so diffusion of PAX, which is a large molecule, into the core of nanoparticles becomes slow.

Table 4-3. Loading Efficiencies[a] and Loading Levels of Paclitaxel-Loaded P(MCL-*co*-CL)-*b*-PEO Nanoparticles Prepared in the Bulk.

Copolymer	Drug: Polymer Loading Ratio (w/w)	Loading Efficiency (%)	Loading Level (w/w)
PMCL-0	**0.10**	37 ± 3	0.037 ± 0.003
	0.25	14 ± 1	0.035 ± 0.003
	0.50	7 ± 1	0.035 ± 0.004
PMCL-25	**0.10**	47 ± 4	0.047 ± 0.002
	0.25	19 ± 2	0.048 ± 0.006
	0.50	9 ± 1	0.045 ± 0.005
PMCL-50	**0.10**	46 ± 4	0.047 ± 0.003
	0.25	19 ± 1	0.048 ± 0.001
	0.50	9 ± 1	0.045 ± 0.004
PMCL-75	**0.10**	48 ± 2	0.049 ± 0.002
	0.25	18 ± 1	0.047 ± 0.002
	0.50	9 ± 1	0.046 ± 0.006
PMCL-100	**0.10**	48 ± 4	0.049 ± 0.005
	0.25	19 ± 1	0.047 ± 0.002
	0.50	9 ± 1	0.047 ± 0.005

a) Errors for loading efficiencies and loading levels are standard deviations of mean values determined for three separate preparations.

4.3.6. Effect of MCL Content on PAX Release Rates of Bulk-Prepared Nanoparticles

For *in vitro* release experiments, bulk-prepared nanoparticles of all five copolymers at a single loading ratio (r = 0.25) were assessed and the resulting release profiles are shown in Figure 4-5. Release half times, $t_{1/2}$, for each release profiles are plotted in Figure 4-7. Corresponding decreases in hydrodynamic diameter of nanoparticles during PAX release, due to hydrolytic degradation, are shown in Figure 4-6.

The release profiles in Figure 4-5 show a clear effect of MCL content on release rate, with PMCL-0 showing the fastest release and release rates decreasing with increasing MCL content. These differences can be shown by determining $t_{1/2}$ from each profile and plotting $t_{1/2}$ versus MCL content (Figure 4-7). This plot shows a sharp increase in release half time from ~50 min to ~60 min as the MCL content increases from 0 to 25 wt %, with a more gradual increase to ~70 min as the MCL content increases to 100 wt %.

To account for the sharp decrease in release rate between PMCL-0 and PMCL-25, we consider that an important mechanism of PAX release is hydrolytic degradation of nanoparticles at physiological temperature and pH and high ionic strength. To track hydrolytic degradation of the nanoparticles during the first 24 h of release, we follow the hydrodynamic diameters by DLS as a function of release time (Figure 4-6). We see that over this time period the sizes of PMCL-0 nanoparticles drop from ~1100 nm to ~200 nm, (i.e. by about 500%) attributed to the hydrolytic breakdown of the original cylinders (discussed previously) into spheres, whereas the sizes of all of the other copolymer nanoparticles (shown previously to be spheres) drop from ~70 to ~50 nm (i.e. by about

40%), attributed to a gradual degradation of spheres. Thus the dramatic increase in surface area of the originally-cylindrical PMCL-0 nanoparticles over the first 24 h of release, compared to the other MCL-containing spherical nanoparticles, explains the associated differences in release rates.

Among the MCL-containing nanoparticles, the release profiles (Figure 4-5) and $t_{1/2}$ value (Figure 4-7) are similar within the associated error bars. However, we do note a small but consistent monotonic trend of decreasing release rate or increasing $t_{1/2}$ with increasing MCL content between PMCL-25 and PMCL-100. This trend may be due to the expected increase in PAX solubility and viscosity of the amorphous phase as the MCL content increases. In theory, hydrophobicity increases with increasing MCL content, owing to the non-polar methyl group. More hydrophobic core results in more stable nanoparticles and hence slow release rate.[13] According to the literature, methyl as a main chain side group increases the T_g of many common polymers, e.g. poly(methyl acrylate) (T_g =10°C) vs. poly(methyl methacrylate) (atactic, T_g =105°C)[31] and polyethylene (T_g =-125°C) vs. polypropylene (atactic, T_g =-13°C)[32], which increases their viscosity due to an increase in bond rotational energy and therefore chain stiffness.[33] Thus an increase in viscosity of the amorphous cores is expected from PMCL-25 to PMCL-100 as the number of methyl groups increases, leading to slower diffusion of the drug and thus slower release.

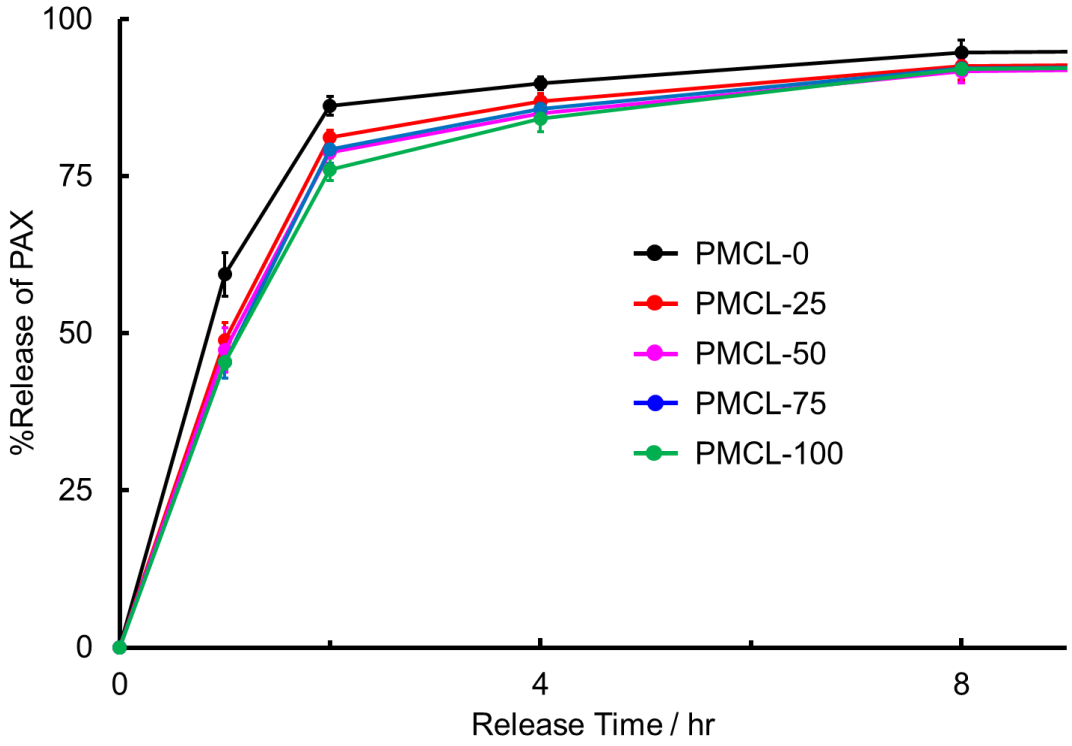

Figure 4-5. Effect of MCL content on *in vitro* release profile of paclitaxel-loaded P(MCL-*co*-CL)-*b*-PEO nanoparticles (r = 0.25) prepared in the bulk. Errors are standard deviations of mean values determined for three separate preparations.

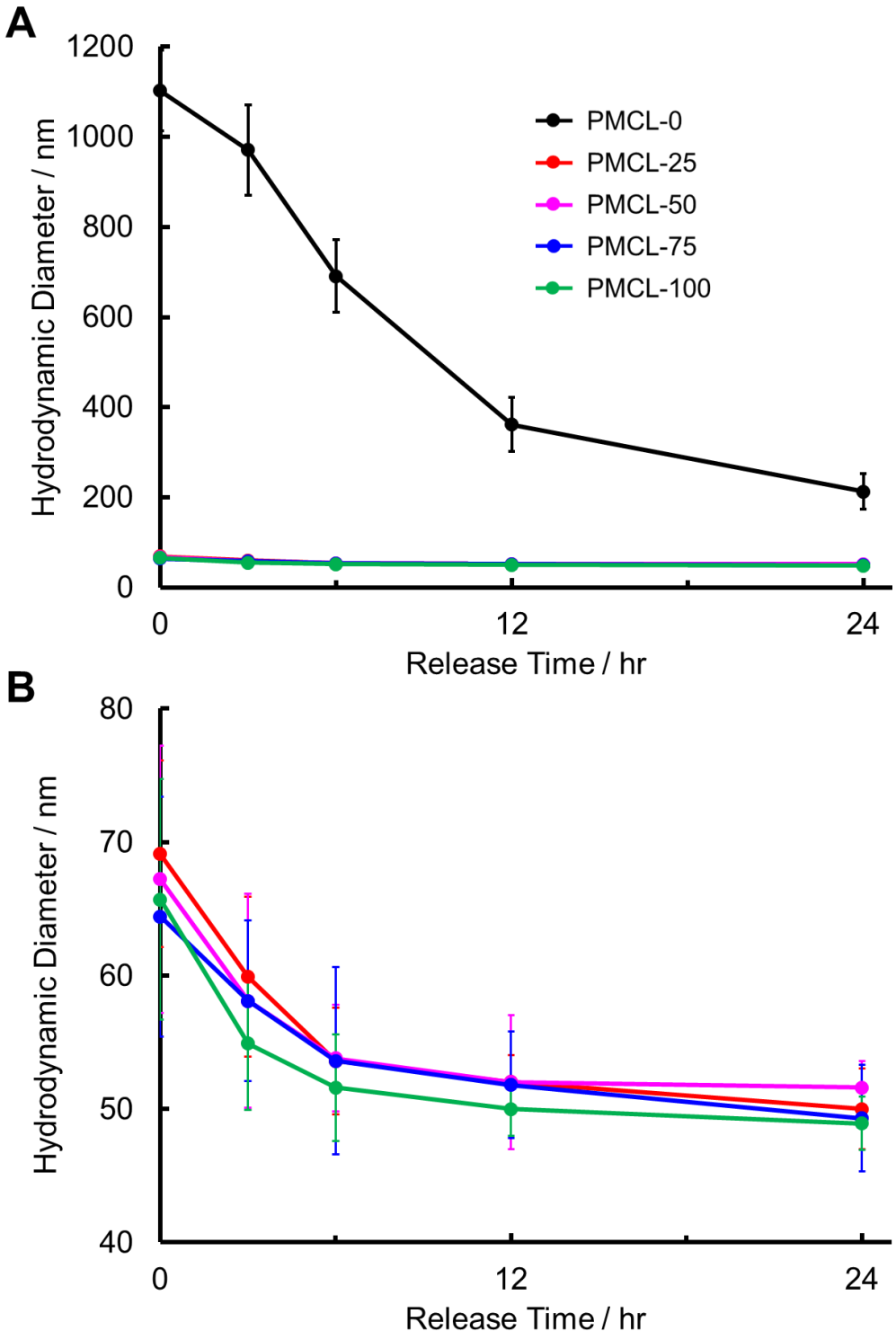

Figure 4-6. Hydrolytic degradation during *in vitro* release of paclitaxel-loaded P(MCL-*co*-CL)-*b*-PEO nanoparticles (r = 0.25) prepared in the bulk. Errors are standard deviations of mean values determined for three measurements of the same preparation.

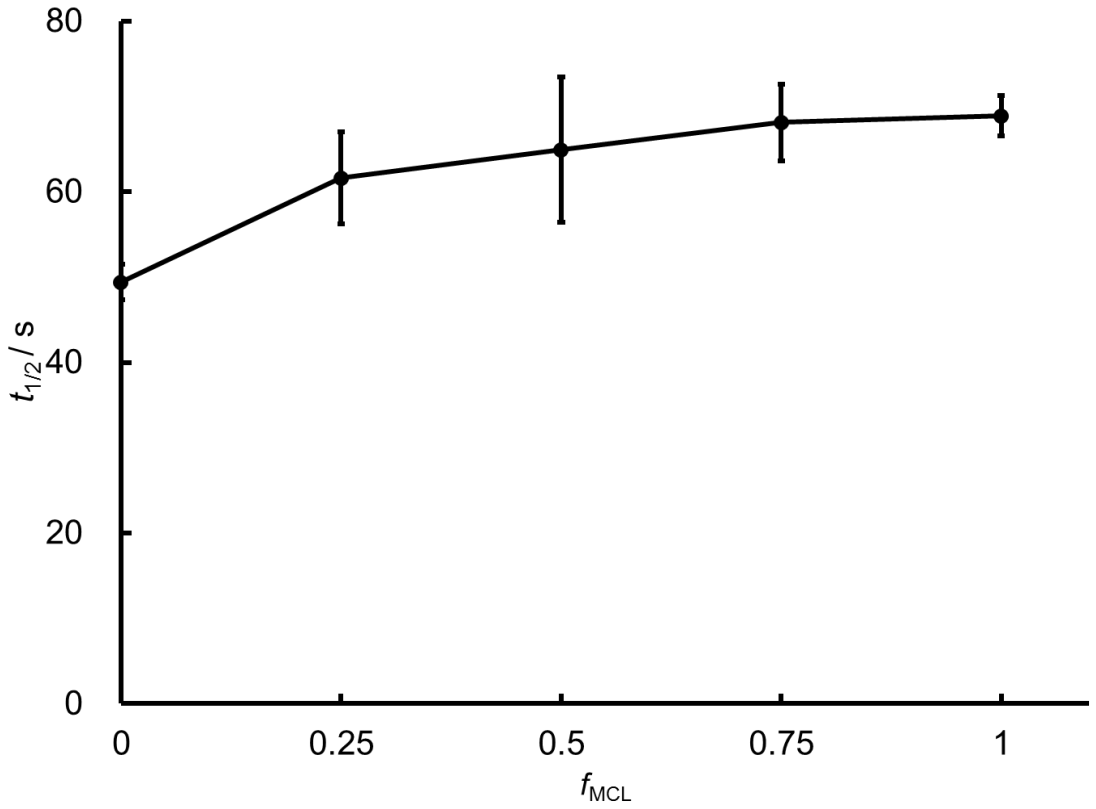

Figure 4-7. Effect of MCL content on $t_{1/2}$ during in vitro release profile of paclitaxel-loaded P(MCL-*co*-CL)-*b*-PEO nanoparticles (r = 0.25) prepared in the bulk. Errors are standard deviations of mean values determined for three separate preparations.

4.3.7. Effect of Flow Rate on Nanoparticle Structure

The above off-chip results prove that MCL-containing copolymers have different sizes, morphologies, loading levels and release profiles from PMCL-0. Copolymerization of MCL and CL offers a successful structural and functional control over paclitaxel loaded nanoparticles. In the following part, shear is introduced to these MCL-containing polymers, namely PMCL-25, PMCL50 and PMCL-75, and the effects are explored.

Similar to my previous study in Chapter 2,[34] PMCL also has a low T_g core. We suspect it is dynamic in room temperature. Therefore, unquenched and quenched morphologies of PMCL-50 nanoparticles were examined.

Figure 4-8 shows the TEM images of unquenched and quenched PMCL-50 nanoparticles formed at various flow rates without PAX encapsulation. In the unquenched samples, compared to the spheres formed in the bulk (Figure 4-8A), some larger spheres were observed at 50 μL/min (Figure 4-8B). Instead of even larger spheres, short rods were visible at 100 μL/min (Figure 4-8C). These morphological changes are likely due to shear-induced coalescence. At 200 μL/min, pure spheres were obtained, proving shear-induced break up at higher flow rate (Figure 4-8D).

Upon quenching and dialysis, all shear effects in morphologies were erased (Figure 4-8 E-H), in agreement with the previous results in Chapter 2. Pure, monodispersed spheres were observed in the bulk and at all flow rates investigated.

Moreover, core crystallinity of PMCL-25 nanoparticles prepared in the bulk and prepared at 50 μL/min without drug was analyzed. XRD patterns and fitting are shown in Figure S4-5. There was no apparent difference in crystallinity between these two samples.

These preliminary results demonstrate that MCL repeat units in the core are indeed dynamic, but in the meantime, the shear effect on morphology is not significant even in the unquenched samples. The core of nanoparticles is amorphous regardless of the preparation method.

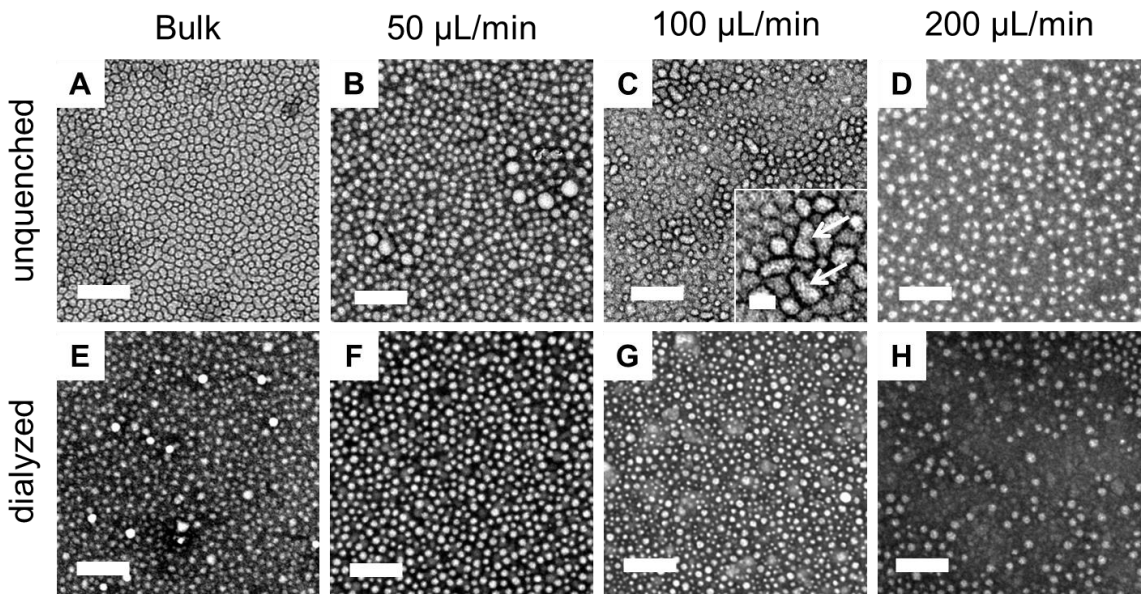

Figure 4-8. Effect of flow rate on PMCL-50 nanoparticle morphology without paclitaxel encapsulation through TEM. Scale bars are 200 nm in main figures and 50 nm in insets.

For the following experiments, only dialyzed nanoparticles were analyzed. With the aim of drug loading and delivery, nanoparticles in water are of practical applications. TEM images of paclitaxel-loaded PMCL-25, PMCL-50, PMCL-75 formed in the bulk and at three different flow rates are shown in Figure 4-9. All conditions formed pure spheres except for PMCL-50 and PMCL-75 formed at 100 μL/min. In the PMCL-50 nanoparticles formed at 100 μL/min, cylinders were observed. This is the same copolymer studied in the last experiment, but cylinders were not seen in the dialyzed sample in that experiment. Since this cylinder forming sample is drug-loaded, and the encapsulation of drug generates more free volume within the core. The increased free volume enhances diffusion of polymer chains.[35] Therefore the drug-loaded nanoparticles respond to shear effect differently. The mechanism for PMCL-75 to form short rods is similar. At 200 μL/min, the shear is so high that only pure spheres could be formed.

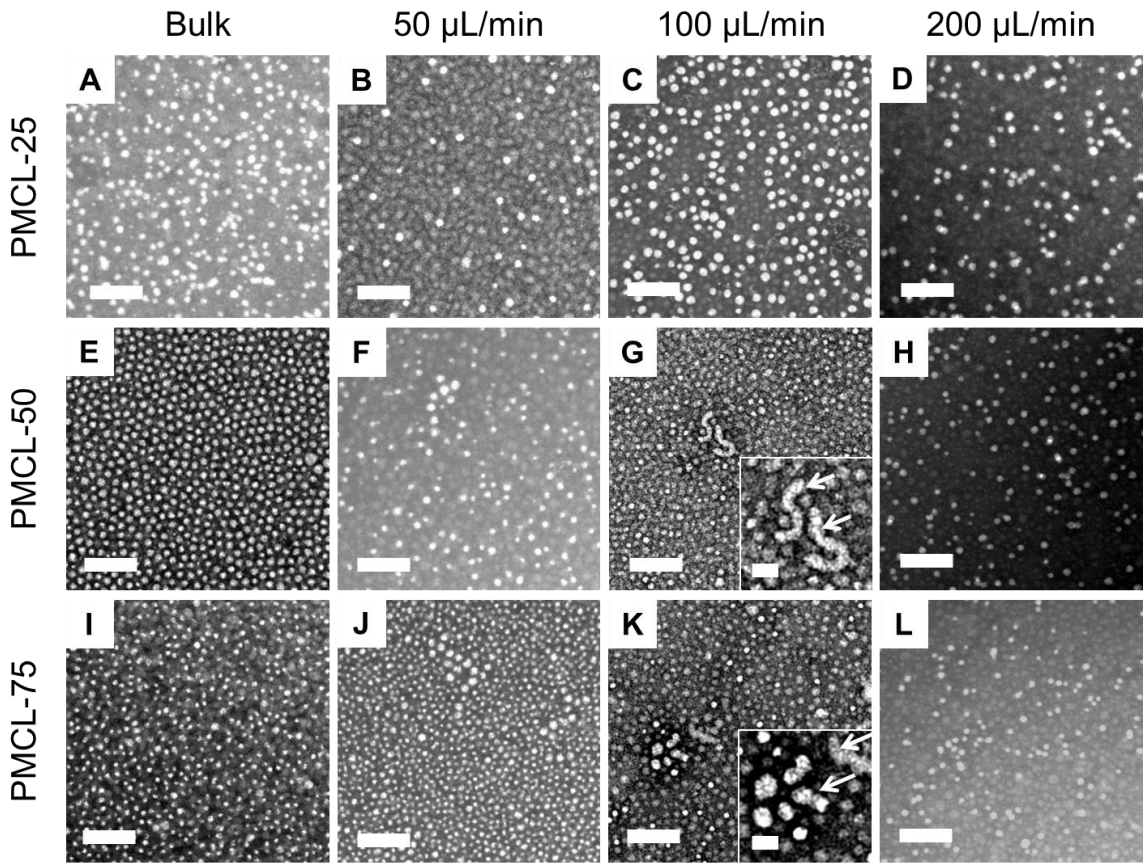

Figure 4-9. Effect of flow rate on paclitaxel-loaded P(MCL-*co*-CL)-*b*-PEO nanoparticle (r = 0.25) morphology through TEM. Scale bars are 200 nm in main figures and 50 nm in insets.

Table 4-4. Morphologies[a], Mean Dimensions[b] and Hydrodynamic Diameter for Paclitaxel-Loaded P(MCL-*co*-CL)-*b*-PEO Nanoparticles (*r* = 0.25) Prepared in the Bulk and in the Gas-Liquid Segmented Microfluidic Reactor at Various Flow Rates.

Copolymer, Flow Rate	Morphologies and Mean Dimensions (nm)	Hydrodynamic Diameter (nm)
PMCL-25		
Bulk	S (24 ± 1)	63 ± 6
50 μL/min	S (25 ± 2)	61 ± 6
100 μL/min	S (23 ± 1)	50 ± 6
200 μL/min	S (24 ± 3)	48 ± 6
PMCL-50		
Bulk	S (24 ± 2)	60 ± 10
50 μL/min	S (21 ± 1)	54 ± 1
100 μL/min	S (20 ± 3) C (19 ± 1)	170 ± 40
200 μL/min	S (22 ± 1)	46 ± 5
PMCL-75		
Bulk	S (26 ± 1)	60 ± 10
50 μL/min	S (22 ± 2)	53 ± 9
100 μL/min	S (23 ± 1) C (24 ± 2)	140 ± 20
200 μL/min	S (20 ± 1)	44 ± 1

a) Morphologies are indicated as S (spheres) and C (cylinders or rods).

b) Numbers refer to sphere diameters or cylinder widths. Errors for mean dimensions and hydrodynamic diameters are standard deviations of mean values determined for three separate preparations.

The mean dimensions from TEM and the hydrodynamic diameters from DLS are tabulated in Table 4-4. The size analysis suggests a slight decrease in core dimension for PMCL-50 and PMCL-75, while that for PMCL-25 remain constant. In contrast, except for the cases where cylinders were formed, DLS results consistently demonstrates a decrease in sphere diameter as flow rate increased.

Because the core of MCL-containing nanoparticles is amorphous and dynamic, even though depositing sample on grid from water has largely reduce chain rearrangement kinetics, it is still possible that the size may change owing to drying artefact. However, hydrodynamic diameter represents the real size of the nanoparticles in solution, thus is more trustworthy.

The effect of flow rate on hydrodynamic diameter is also shown in Figure 4-10. This further proves the decrease in sphere size with flow rate. The effect is attributed to shear-induced break up at high shear rates.

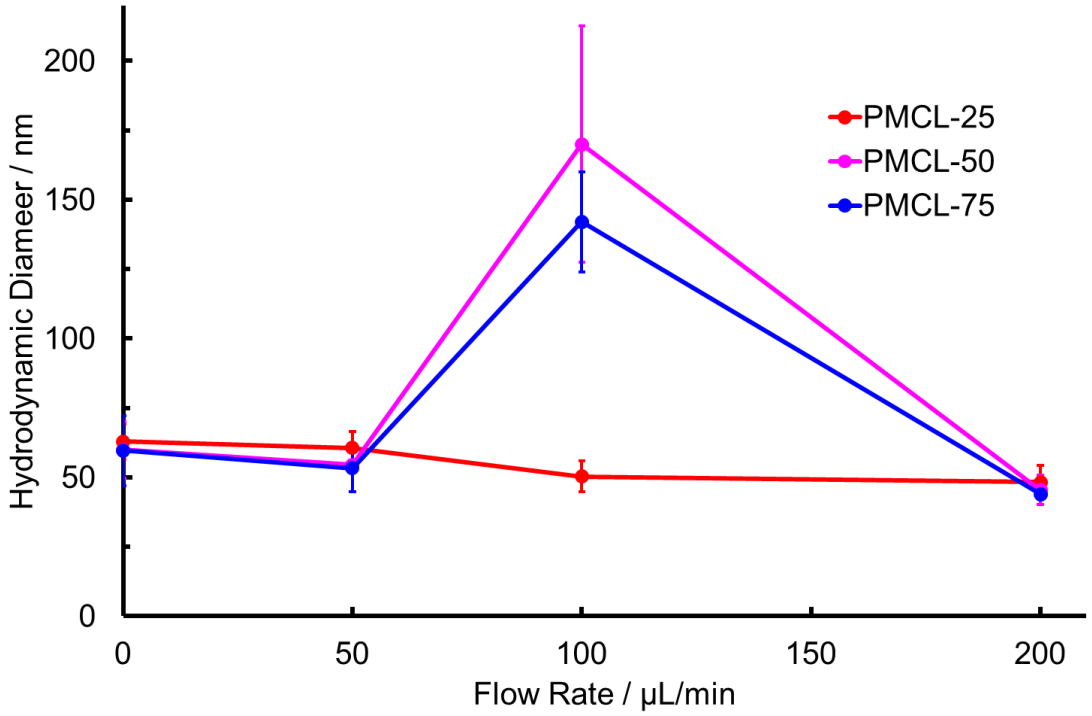

Figure 4-10. Effect of flow rate on hydrodynamic diameters of paclitaxel-loaded P(MCL-*co*-CL)-*b*-PEO nanoparticles (r = 0.25) prepared in the bulk (flow rate = 0 data points) and in the gas-liquid segmented microfluidic reactor at various flow rates. Errors are standard deviations of mean values determined for three separate preparations.

4.3.8. Effect of Flow Rate on Loading Efficiency and Loading Level

Table 4-5. Loading Efficiencies[a] and Loading Levels of Paclitaxel-Loaded P(MCL-*co*-CL)-*b*-PEO Nanoparticles (*r* = 0.25) Prepared in the Bulk and in the Gas-Liquid Segmented Microfluidic Reactor at Various Flow Rates.

Copolymer, Flow Rate	Loading Efficiency (%)	Loading Level (w/w)
PMCL-25		
Bulk	19 ± 2	0.048 ± 0.006
50 μL/min	11 ± 1	0.029 ± 0.003
100 μL/min	10 ± 1	0.026 ± 0.002
200 μL/min	10 ± 1	0.026 ± 0.001
PMCL-50		
Bulk	19 ± 1	0.048 ± 0.001
50 μL/min	11 ± 1	0.028 ± 0.001
100 μL/min	11 ± 1	0.027 ± 0.001
200 μL/min	10 ± 1	0.025 ± 0.003
PMCL-75		
Bulk	18 ± 1	0.047 ± 0.002
50 μL/min	12 ± 1	0.030 ± 0.003
100 μL/min	10 ± 1	0.026 ± 0.002
200 μL/min	10 ± 1	0.026 ± 0.001

a) Errors for loading efficiencies and loading levels are standard deviations of mean values determined for three separate preparations.

Next, loading efficiencies and loading levels were determined using similar methodology to the bulk experiments, and the results for PMCL-25, PMCL-50 and PMCL-75 nanoparticles formed on-chip at various flow rates are tabulated in Table 4-5. It is evident that on-chip loading levels are much lower than their counterparts in the bulk, but is quite constant regardless of flow rate. Likewise, the loading levels of nanoparticles of the three copolymers under the same conditions are almost the same. The mole ratio of paclitaxel and polymer chains is calculated to be ~0.3 for on-chip prepared MCL-containing nanoparticles.

This is the first time our group has observed a decrease in loading level on-chip compared to the chemically-equivalent off-chip preparation. Previous results from our group of paclitaxel-loaded PCL-*b*-PEO (using 25 times-lower loading levels than in the current study) showed an increased loading efficiency on-chip. In this work, better mixing was thought the be the reason for higher loading.[20] However, in my system, better mixing does not contribute to higher loading. In terms of mechanism of on-chip manipulation of loading level, there is still a lot for us to explore. The cause of a lower loading could be a result of drug-PDMS interaction, lower residence time or rapid increase in water content. Without experience of more systems, it is hard to generalize the shear effect on drug loading.

4.3.9. Effect of Flow Rate on *In Vitro* Release

Figure 4-11A shows the release profiles of PMCL-50 nanoparticles form in the bulk, at 50 and 200 μL/min. Figure 4-11B shows the hydrodynamic size change during release and Figure 4-12 shows the effect of flow rate on release half time. The reason to choose these conditions is that all of them formed spheres, and the core of nanoparticles

is amorphous. If there is any effect on the release profile, it is neither a morphological effect nor a crystallinity effect. In other words, we wanted to know whether a change in morphology and crystallinity is required to achieve slower release.

In Figure 4-9A, it could be observed that on-chip formed nanoparticles had a slower release than bulk-prepared nanoparticles, and nanoparticles formed at highest flow rate had an even slower release. The difference was distinct in the first 24 hours and was visible up to 3 days. After 5 days, all three samples reach a similar %release close to complete release. The $t_{1/2}$ results demonstrate a significantly longer $t_{1/2}$ as flow rate increased (Figure 4-12).

In Figure 4-9B, the change in the hydrodynamic diameter during release is not very profound since all three samples were pure spheres and were not subject to any substantial change in size like cylinders and platelets. The bulk-prepared nanoparticles started from a bigger size, and therefore the change in the first few hours were more than that of the on-chip prepared nanoparticles. Additionally, the bulk-prepared nanoparticles ended up having a bigger size after levelling off. The decrease in hydrodynamic diameter for the two on-chip prepared samples was basically the same.

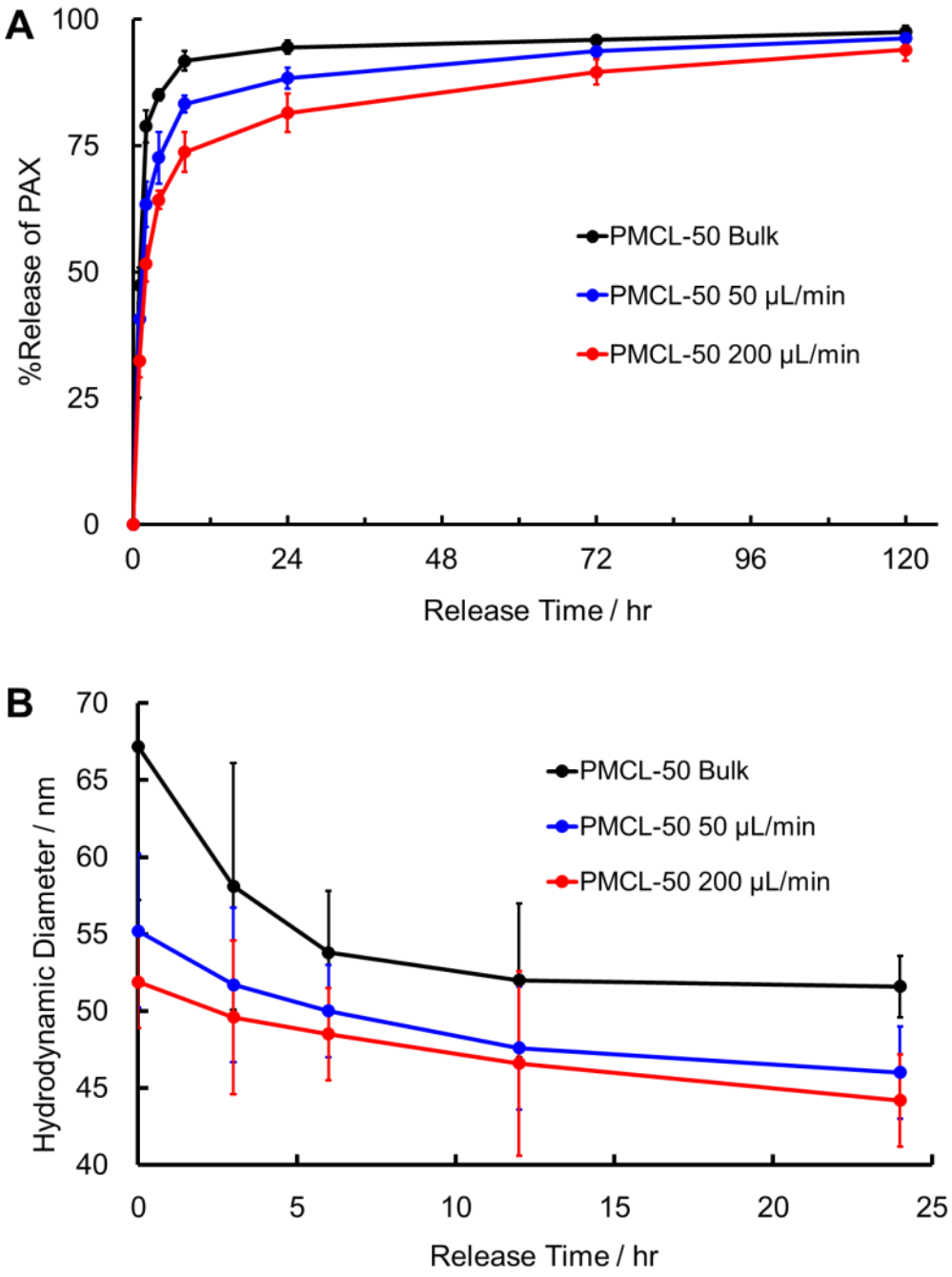

Figure 4-11. *In vitro* release of paclitaxel-loaded PMCL-50 nanoparticles (r = 0.25) prepared in the bulk and in the gas-liquid segmented microfluidic reactor at various flow rates. (A) Effect of flow rate on *in vitro* release profile. Errors are standard deviations of mean values determined for three separate preparations. (B) Hydrolytic degradation during *in vitro* release. Errors are standard deviations of mean values determined for three measurements of the same preparation.

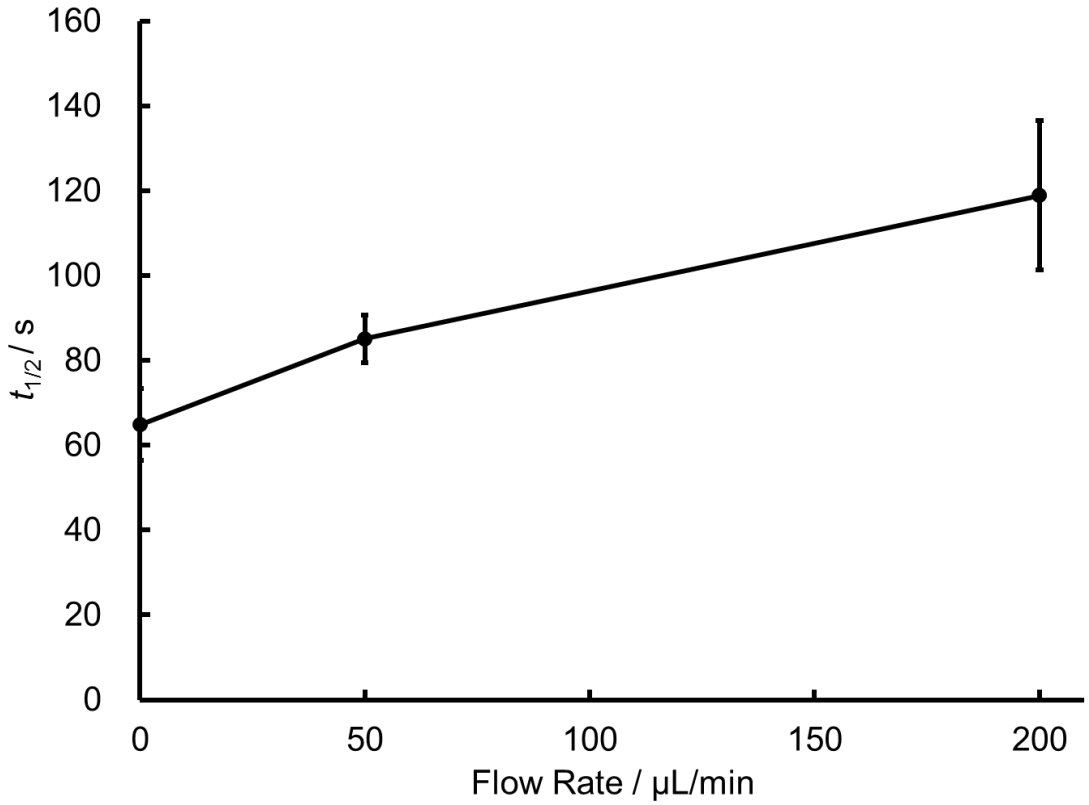

Figure 4-12. Effect of flow rate on $t_{1/2}$ during *in vitro* release profile of paclitaxel-loaded P(MCL-*co*-CL)-*b*-PEO nanoparticles (r = 0.25) prepared in the bulk (flow rate = 0 data point) and in the gas-liquid segmented microfluidic reactor at various flow rates. Errors are standard deviations of mean values determined for three separate preparations.

These results are promising, because they suggest that based on enhanced mixing on-chip we could control the release rate for this system. Although the hydrolytic degradation is a bit different among the three conditions, it is not enough to cause the difference in release rate. As is put forward before by our group, mixing on-chip induce a more homogeneous distribution of paclitaxel in the core.[20] Normally, most of drug stays in the corona or core-corona interface. The release rate of the drug depends on its localization within the nanoparticles. Release from the outer corona region is rapid. The release of drug localized in the corona or at the core-corona interface accounts for ‘burst

release' within the first few hours.[36] With a more homogeneous distribution of drug deeper in the core, it takes more time for the drug to diffuse to the core-corona interface and finally escape from the nanoparticle. In this way, burst release is reduced. In Figure 4-9A, after 2 hours, nanoparticles formed in the bulk already released more than 80% of drug, while nanoparticles formed in the microfluidic reactor at 200 μL/min only released 65% of drug. The major distinction in release rate is cause by the different burst release. After that all three curves reached a plateau and gradually released the rest of the encapsulated drug in a similar manner.

4.4. Conclusion

In the first part of this chapter, chemical control by copolymerization of MCL and CL was evaluated. Although the attempt to tune crystallinity failed and we ended up getting a series of amorphous copolymers with different chemical compositions, structural and functional control was a success. The MCL-containing copolymers tend to form spheres, compared with the cylindrical morphology of PMCL-0, and the sizes were around 20 nm. Loading efficiency and loading level of paclitaxel increased by increasing MCL content. Slow release was achieved due to slow hydrolytic degradation.

In the second part of this chapter, shear control by on-chip micellization of MCL-containing copolymers was studied. Morphological change with flow rate was observed but not significant, and the loading level decreased through synthesis on-chip. However, even though neither morphological nor crystallinity change was observed, reduced in release rate was demonstrated. A mechanism of mixing-induced homogeneous distribution of drug in the core is the explanation.

Changing chemical composition has control over a lot of properties of nanoparticles for drug delivery applications. In the meantime, microfluidics also offers a convenient top-down handle on release rate. Next step forward will be cell line study to explore the cytotoxicity of these nanoparticles.

4.5. Supporting Information

Please see Appendix C for supporting information: Data for cwc determination; Calibration curve for HPLC; Full release profile of PAX-loaded nanoparticles; Bulk and on-chip XRD patterns and fitting for PMCL-25.

4.6. References

1. V. P. Torchilin Structure and Design of Polymeric Surfactant-Based Drug Delivery Systems. *Journal of Controlled Release* **2001,** *73*, 137.

2. B. G. Yu, T. Okano, K. Kataoka and G. Kwon Polymeric Micelles for Drug Delivery: Solubilization and Haemolytic Activity of Amphotericin B. *Journal of Controlled Release* **1998,** *53*, 131.

3. Z. Sezgin, N. Yüksel and T. Baykara Preparation and Characterization of Polymeric Micelles for Solubilization of Poorly Soluble Anticancer Drugs. *European Journal of Pharmaceutics and Biopharmaceutics* **2006,** *64*, 261.

4. J. Heller Biodegradable Polymers in Controlled Drug Delivery. *Crit Rev Ther Drug Carrier Syst* **1984,** *1*, 39.

5. J.-H. Park, M. Allen and M. Prausnitz Polymer Microneedles for Controlled-Release Drug Delivery. *Pharm Res* **2006,** *23*, 1008.

6. S. Freiberg and X. X. Zhu Polymer Microspheres for Controlled Drug Release. *International Journal of Pharmaceutics* **2004,** *282*, 1.

7. K. E. Uhrich, S. M. Cannizzaro, R. S. Langer and K. M. Shakesheff Polymeric Systems for Controlled Drug Release. *Chemical Reviews* **1999,** *99*, 3181.

8. F. M. Veronese, O. Schiavon, G. Pasut, R. Mendichi, L. Andersson, A. Tsirk, J. Ford, G. Wu, S. Kneller, J. Davies and R. Duncan Peg−Doxorubicin Conjugates: Influence of Polymer Structure on Drug Release, in Vitro Cytotoxicity, Biodistribution, and Antitumor Activity. *Bioconjugate Chemistry* **2005,** *16*, 775.

9. H.-T. Chen, M. F. Neerman, A. R. Parrish and E. E. Simanek Cytotoxicity, Hemolysis, and Acute in Vivo Toxicity of Dendrimers Based on Melamine, Candidate Vehicles for Drug Delivery. *Journal of the American Chemical Society* **2004,** *126*, 10044.

10. T. M. Allen Ligand-Targeted Therapeutics in Anticancer Therapy. *Nat Rev Cancer* **2002,** *2*, 750.

11. R. M. Schiffelers, A. Ansari, J. Xu, Q. Zhou, Q. Tang, G. Storm, G. Molema, P. Y. Lu, P. V. Scaria and M. C. Woodle Cancer Sirna Therapy by Tumor Selective Delivery with Ligand-Targeted Sterically Stabilized Nanoparticle. *Nucleic Acids Research* **2004,** *32*, e149.

12. N. Nasongkla, X. Shuai, H. Ai, B. D. Weinberg, J. Pink, D. A. Boothman and J. Gao Crgd - Functionalized Polymer Micelles for Targeted Doxorubicin Delivery. *Angewandte Chemie* **2004,** *116*, 6483.

13. C. Allen, D. Maysinger and A. Eisenberg Nano-Engineering Block Copolymer Aggregates for Drug Delivery. *Colloids and Surfaces B: Biointerfaces* **1999,** *16*, 3.

14. J. Liu, F. Zeng and C. Allen In Vivo Fate of Unimers and Micelles of a Poly(Ethylene Glycol)-Block-Poly(Caprolactone) Copolymer in Mice Following Intravenous Administration. *European Journal of Pharmaceutics and Biopharmaceutics* **2007,** *65*, 309.

15. S. Creutz, J. van Stam, F. C. De Schryver and R. Jérôme Dynamics of Poly((Dimethylamino)Alkyl Methacrylate-Block-Sodium Methacrylate) Micelles. Influence of Hydrophobicity and Molecular Architecture on the Exchange Rate of Copolymer Molecules. *Macromolecules* **1998,** *31*, 681.

16. M. P. Xiong, J. A. Yáñez, C. M. Remsberg, Y. Ohgami, G. S. Kwon, N. M. Davies and M. L. Forrest Formulation of a Geldanamycin Prodrug in Mpeg-B-Pcl Micelles Greatly Enhances Tolerability and Pharmacokinetics in Rats. *Journal of Controlled Release* **2008,** *129*, 33.

17. B. Shi, C. Fang, M. You, Y. Zhang, S. Fu and Y. Pei Stealth Mepeg-Pcl Micelles: Effects of Polymer Composition on Micelle Physicochemical Characteristics, in Vitro Drug Release, in Vivo Pharmacokinetics in Rats and Biodistribution in S180 Tumor Bearing Mice. *Colloid Polym Sci* **2005,** *283*, 954.

18. D. A. Christian, S. Cai, O. B. Garbuzenko, T. Harada, A. L. Zajac, T. Minko and D. E. Discher Flexible Filaments for in Vivo Imaging and Delivery: Persistent Circulation of Filomicelles Opens the Dosage Window for Sustained Tumor Shrinkage. *Molecular Pharmaceutics* **2009,** *6*, 1343.

19. H. Montazeri Aliabadi, D. R. Brocks and A. Lavasanifar Polymeric Micelles for the Solubilization and Delivery of Cyclosporine A: Pharmacokinetics and Biodistribution. *Biomaterials* **2005,** *26*, 7251.

20. A. Bains, Y. Cao and M. G. Moffitt Multiscale Control of Hierarchical Structure in Crystalline Block Copolymer Nanoparticles Using Microfluidics. *Macromolecular Rapid Communications* **2015**, n/a.

21. C. Wang, Y. Xiao, A. Heise and M. Lang Organometallic and Enzymatic Catalysis for Ring Opening Copolymerization of E-Caprolactone and 4-Methyl-E-Caprolactone. *Journal of Polymer Science Part A: Polymer Chemistry* **2011,** *49*, 5293.

22. J. A. Zupancich, F. S. Bates and M. A. Hillmyer Aqueous Dispersions of Poly(Ethylene Oxide)-B-Poly(Γ-Methyl-E-Caprolactone) Block Copolymers. *Macromolecules* **2006,** *39*, 4286.

23. P. Vangeyte and R. Jérôme Amphiphilic Block Copolymers of High ‐ Molecular ‐ Weight Poly (Ethylene Oxide) and Either Ε ‐ Caprolactone or Γ ‐ Methyl ‐ Ε ‐

Caprolactone: Synthesis and Characterization. *Journal of Polymer Science Part A: Polymer Chemistry* **2004,** *42*, 1132.

24. M. T. Martello and M. A. Hillmyer Polylactide–Poly(6-Methyl-E-Caprolactone)–Polylactide Thermoplastic Elastomers. *Macromolecules* **2011,** *44*, 8537.

25. L. Huynh, J. Grant, J.-C. Leroux, P. Delmas and C. Allen Predicting the Solubility of the Anti-Cancer Agent Docetaxel in Small Molecule Excipients Using Computational Methods. *Pharm Res* **2008,** *25*, 147.

26. H. Gelderblom, J. Verweij, K. Nooter and A. Sparreboom Cremophor El: The Drawbacks and Advantages of Vehicle Selection for Drug Formulation. *European Journal of Cancer* **2001,** *37*, 1590.

27. R. B. Weiss, R. C. Donehower, P. H. Wiernik, T. Ohnuma, R. J. Gralla, D. L. Trump, J. R. Baker, D. A. Van Echo, D. D. Von Hoff and B. Leyland-Jones Hypersensitivity Reactions from Taxol. *Journal of Clinical Oncology* **1990,** *8*, 1263.

28. E. A. Eisenhauer, W. W. ten Bokkel Huinink, K. D. Swenerton, L. Gianni, J. Myles, M. E. van der Burg, I. Kerr, J. B. Vermorken, K. Buser and N. Colombo European-Canadian Randomized Trial of Paclitaxel in Relapsed Ovarian Cancer: High-Dose Versus Low-Dose and Long Versus Short Infusion. *Journal of Clinical Oncology* **1994,** *12*, 2654.

29. J. A. Massey, K. Temple, L. Cao, Y. Rharbi, J. Raez, M. A. Winnik and I. Manners Self-Assembly of Organometallic Block Copolymers: The Role of Crystallinity of the Core-Forming Polyferrocene Block in the Micellar Morphologies Formed by Poly(Ferrocenylsilane-B-Dimethylsiloxane) in N-Alkane Solvents. *Journal of the American Chemical Society* **2000,** *122*, 11577.

30. Y. Geng and D. E. Discher Visualization of Degradable Worm Micelle Breakdown in Relation to Drug Release. *Polymer* **2006,** *47*, 2519.

31. J. L. Eguiburu, J. J. Iruin, M. J. Fernandez-Berridi and J. San Román Blends of Amorphous and Crystalline Polylactides with Poly(Methyl Methacrylate) and Poly(Methyl Acrylate): A Miscibility Study. *Polymer* **1998,** *39*, 6891.

32. J. M. G. Cowie and V. Arrighi, *Polymers: Chemistry and Physics of Modern Materials*. 3 ed.; CRC Press: Boca Raton, 2007.

33. T. Sato and A. Teramoto, Concentrated Solutions of Liquid-Crystalline Polymers. In *Biopolymers Liquid Crystalline Polymers Phase Emulsion*, Springer Berlin Heidelberg: 1996; Vol. 126, pp 85-161.

34. Z. Xu, B. Yan, J. Riordon, Y. Zhao, D. Sinton and M. G. Moffitt Microfluidic Synthesis of Photoresponsive Spool-Like Block Copolymer Nanoparticles: Flow-

Directed Formation and Light-Triggered Dissociation. *Chemistry of Materials* **2015,** *27*, 8094.

35. J. S. Vrentas and C. M. Vrentas Evaluation of the Free-Volume Theory of Diffusion. *Journal of Polymer Science Part B: Polymer Physics* **2003,** *41*, 501.

36. Y. Teng, M. E. Morrison, P. Munk, S. E. Webber and K. Procházka Release Kinetics Studies of Aromatic Molecules into Water from Block Polymer Micelles. *Macromolecules* **1998,** *31*, 3578.

Chapter 5.

General Conclusions and Future Work

5.1. General Conclusions

In this thesis, we have shown that the process of block copolymer self-assembly in solution is significantly influenced by shear and rapid mixing in a gas-liquid segmented microfluidic reactor. Structural and functional controls of block copolymer nanoparticles formed in the microfluidic reactor were demonstrated by analyzing structures, size distributions, crystallinity and functions.

In the past, our group has studied copolymers that have a glassy core at room temperature such as PS-*b*-PAA or a semicrystalline core such as PCL-*b*-PEO. However, in the thesis, copolymers that have an amorphous core with a T_g much lower than or close to room temperature were investigated (PNBA-*b*-PDMA and P(MCL-*co*-CL)-*b*-PEO). Although many of these nanoparticles formed on-chip were not stable to quenching into large excess water, shear memory can be maintained for a few hours. These findings enlarge our understanding of block copolymer self-assembly under high shear rate.

Structural control of nanoparticles by gas-liquid segmented microfluidic reactor were explored using PNBA-*b*-PDMA, PCL-*b*-PEO and P(MCL-*co*-CL)-*b*-PEO. Morphologies, sizes and core crystallinity were controlled by changing flow rate, i.e. shear rate, on-chip. In general, lower curvature morphologies (cylinders, vesicles, lamellae, LCMs, spooled cylinders) were formed on-chip compared to the bulk control (spheres). Increase in size was observed in the meantime. This can be explained by shear-induced coalescence. For some copolymers, PCL-*b*-PEO in this case, formation of

smaller aggregated at high flow rate compared to those formed in medium flow rates was observed. We believed that they were products from shear-induced break-up of large aggregates. For PNBA-*b*-PDMA, a new morphology, spooled cylinders were observed on-chip at medium-high flow rates. They might result from the rotating vortices in liquid plugs. Moreover, the comparison study showed that the structural control on gas-liquid segmented microfluidic reactor (two-phase reactor) is unique. In a single-phase reactor featuring fast mixing, flow rate wasn't able to control structures of nanoparticle. Core crystallinity can also be controlled on-chip. In Chapter 3, PCL crystallinity in nanoparticles showed a linear positive relationship to flow rate, while in the single-phase reactor PCL crystallinity remained the same as the bulk.

Functional control of nanoparticles formed on gas-liquid segment microfluidic reactors were also studied with photoresponsive PNBA-*b*-PDMA and drug-loaded P(MCL-*co*-CL)-*b*-PEO. The photodissociation kinetics of PNBA-*b*-PDMA nanoparticles was found to be faster than the bulk control when formed on-chip. We noted that shear-induced morphologies (cylinders, LCMS, spooled cylinders) were further from equilibrium structures formed in the bulk (spheres). Therefore the slower kinetics can be explained by the faster dissociation of non-equilibrium structures. The paclitaxel loading and release of P(MCL-*co*-CL)-*b*-PEO nanoparticles were also investigated. Lower loading efficiencies and loading levels were obtained, although we are not sure about the mechanism behind it. Slower release was achieved by increasing flow rate. This is likely to be the effect of fast mixing on-chip that generated a more homogenous distribution of drug in the core of nanoparticles.

In conclusion, by applying various copolymers to on-chip self-assembly, we demonstrated that the structures of most nanoparticles can be controlled by shear. Functions of nanoparticles can also be controlled by microfluidics under different mechanisms depending on the functions of nanoparticles.

Apart from top-down control by shear on-chip, bottom-up control by changing copolymer composition was investigated in Chapter 4. Five copolymers of different MCL contents were synthesized. The effect of MCL content on morphology, size, loading and release was studied and discussed. Increasing MCL content tend to decrease crystallinity, increase curvature of structure, increase loading efficiencies and levels, and lower release rates. Bottom-up control is a less convenient but reliable method. By combining bottom-up (chemical) and top-down control (shear) we can fine tune the structures and functions of block copolymer nanoparticles.

5.2. Future Work

The current design of chip has three liquid inlets for water/solvent, pure solvent and polymer/drug/solvent, respectively. We use pure solvent as a separation stream. If there could be another inlet for drug/solvent, we can inject drug and polymer in different streams. In this way, we don’t have to make numerous stock solutions when working with various drug loading ratios. Different polymer concentrations, drug to polymer ratios and water contents are easily accessible just by dialing in flow rates. This is convenient especially when it comes to scale-up synthesis of drug-loaded nanoparticles.

Another work on chip design is to map the change of morphologies on-chip. Insert outlets at several locations of the chip, or design chips that have different channel lengths.

Studying the morphologies of nanoparticles at various channel lengths might be able to help us to visualize the shear-induced coalescence or shear-induced break-up process.

We can extend the responsive copolymer work to dye/drug loading, for the reason that responsive materials are excellent candidates for drug delivery as their release of cargo can be triggered rather than relying on diffusion. The unstable morphologies in water were not optimal for drug delivery, so we might have to find another responsive copolymer that has a glassy or semicrystalline core which makes it stable in water.

Appendix

Appendix A

Supporting Information for Chapter 2

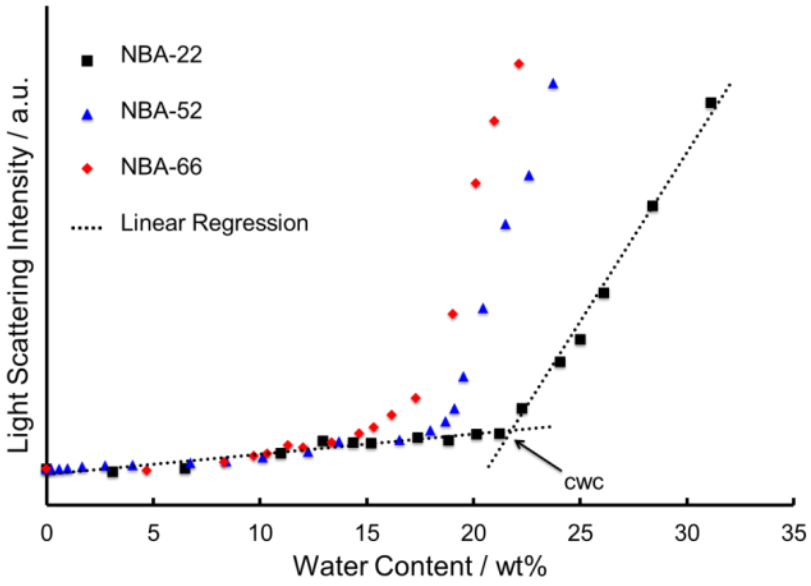

Figure S2-1. Critical water concentration (cwc) determination of 0.33 wt % NBA-22, NBA-52 and NBA-66 in 1,4-dioxane using static light scattering. Cwc values were determined from linear regression as shown for NBA-22 data.

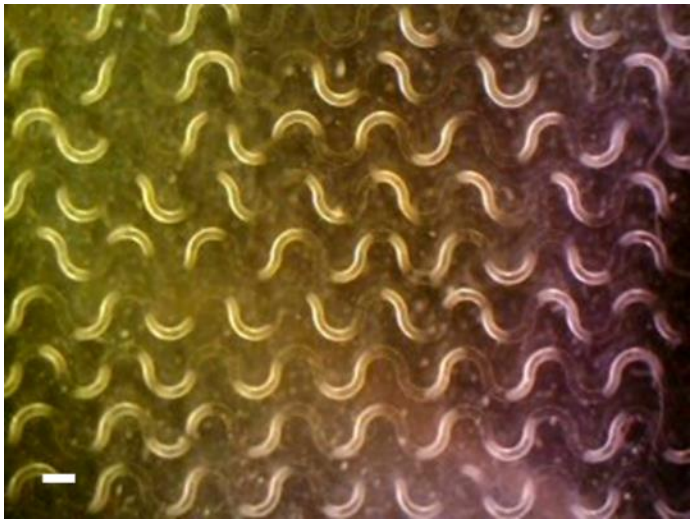

Figure S2-2. Sample optical microscopy image of stable two-phase flow in the microfluidic reactor. Bright regions are Ar bubbles. Scale bar is 500 μm.

Table S2-1. Content and Flow Rates of Three Liquid Streams for Various Microfluidic Nanoparticle Preparations

Nominal Flow Rate	Q_{liq} (μL/min)	PNBA-*b*-PDMA Stream, Q_{liq1} (μL/min)[a]	Pure Dioxane Stream, Q_{liq2} (μL/min)	Water/Dioxane Stream, Q_{liq3} (μL/min)	Water Content, Stream #3 (wt %)	Steady-State Water Content (wt %)[b]
NBA-22						
25 μL/min	12.5	6.25	2.37	3.88	100	31.0
50 μL/min	25.0	12.50	4.75	7.75	100	31.0
100 μL/min	50.0	25.00	9.50	15.50	100	31.0
NBA-52						
25 μL/min	12.5	6.25	2.37	3.88	91.9	28.5
50 μL/min	25.0	12.50	4.75	7.75	91.9	28.5
100 μL/min	50.0	25.00	9.50	15.50	91.9	28.5
NBA-66						
25 μL/min	12.5	6.25	2.37	3.88	90.3	28.0
50 μL/min	25.0	12.50	4.75	7.75	90.3	28.0
100 μL/min	50.0	25.00	9.50	15.50	90.3	28.0

a) Copolymer concentration in Stream #1 = 0.66 wt % for all preparations.

b) Steady-state water content = cwc + 10 wt % for each copolymer.

Table S2-2. Actual Flow Rates for Various Microfluidic Nanoparticle Preparations

Nominal Flow Rate	L_{gas} (mm)	L_{liq} (mm)	Q_{gas} (µL/min)	Q_{liq} (µL/min)	Q_{gas}/Q_{liq}	Q_{total} (µL/min)
NBA-22						
25 µL/min						
Prep #1	0.9	1.0	10.5	12.5	0.84	23.0
Prep #2	2.2	2.0	14.1	12.5	1.13	26.6
Prep #3	1.5	1.3	13.7	12.5	1.10	26.2
50 µL/min						
Prep #1	1.3	1.2	28.9	25.0	1.16	53.9
Prep #2	1.4	1.2	28.3	25.0	1.13	53.3
Prep #3	1.0	1.2	21.1	25.0	0.84	46.1
100 µL/min						
Prep #1	1.3	1.2	54.9	50.0	1.10	104.9
Prep #2	1.0	1.1	44.2	50.0	0.88	94.2
Prep #3	1.0	1.1	45.8	50.0	0.92	95.8
NBA-52						
25 µL/min						
Prep #1	2.0	1.8	14.1	12.5	1.13	26.6
Prep #2	0.8	0.9	11.0	12.5	0.88	23.5
Prep #3	0.7	0.8	10.2	12.5	0.82	22.7
50 µL/min						
Prep #1	1.0	1.0	24.1	25.0	0.96	49.1
Prep #2	1.1	1.0	27.2	25.0	1.09	52.2
Prep #3	1.7	1.6	27.7	25.0	1.11	52.7
100 µL/min						
Prep #1	2.1	2.0	54.1	50.0	1.08	104.1
Prep #2	0.9	1.0	46.1	50.0	0.92	96.1
Prep #3	1.3	1.5	46.2	50.0	0.92	96.2
NBA-66						
25 µL/min						
Prep #1	0.8	0.9	10.5	12.5	0.84	23.0
Prep #2	1.1	1.2	12.1	12.5	0.97	24.6
Prep #3	1.6	1.4	13.5	12.5	1.08	26.0
50 µL/min						
Prep #1	1.7	1.6	27.7	25.0	1.11	52.7
Prep #2	1.7	1.9	22.9	25.0	0.92	47.9
Prep #3	2.3	2.3	25.7	25.0	1.03	50.7
100 µL/min						
Prep #1	1.2	1.2	53.5	50.0	1.07	103.5
Prep #2	0.8	0.9	42.9	50.0	0.86	92.9
Prep #3	2.0	1.8	56.5	50.0	1.13	106.5

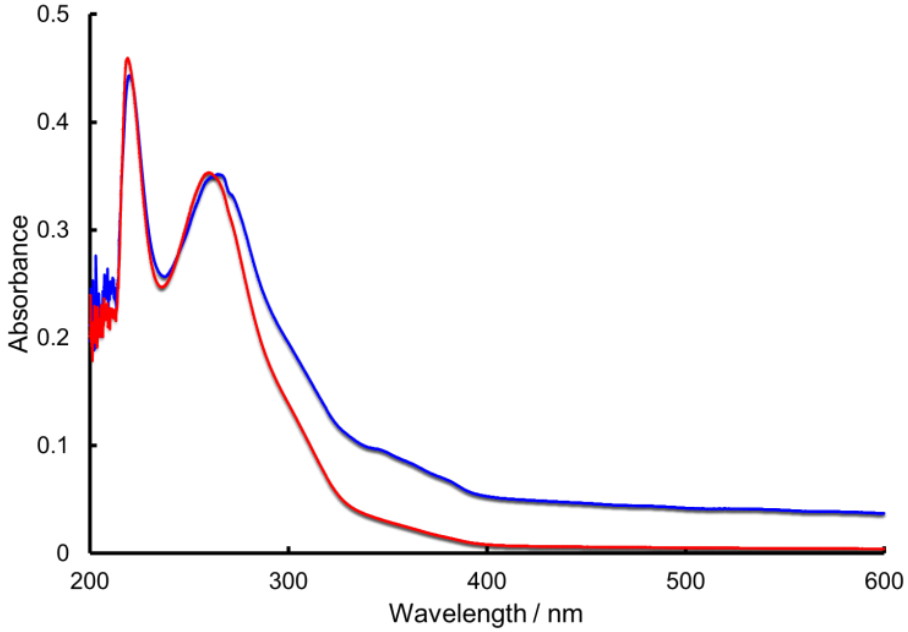

Figure S2-3. UV-Vis absorbance spectra of aqueous dialyzed NBA-66 nanoparticles prepared by the bulk method (blue) and the constituent NBA-66 copolymer dissolved in dioxane (red).

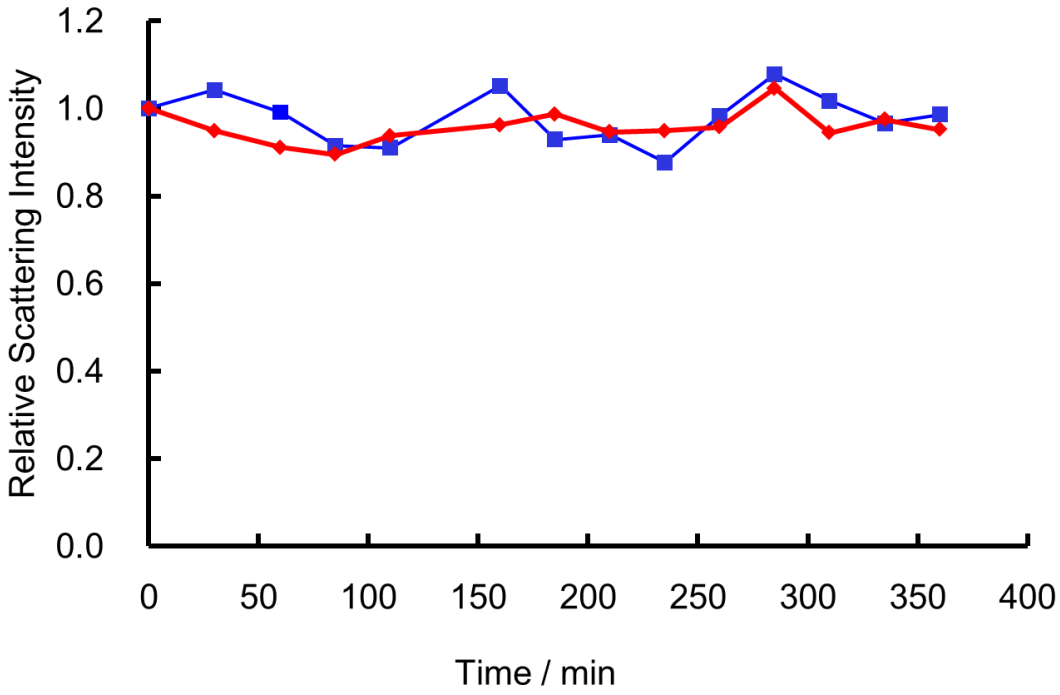

Figure S2-4. Relative light scattering intensity of NBA-22 nanoparticles formed at 25 μL/min (blue squares) and 100 μL/min (red diamonds) on-chip relative to time (no irradiation).

Table S2-3. Percentage of LCMs[a] Relative to Total Number of Unquenched PNBA-*b*-PDMA Nanoparticles Prepared in the Microfluidic Reactor

Sample	25 µL/min	50 µL/min	100 µL/min
NBA-22	0 %	15 ± 4 %	25 ± 2 %
NBA-52	9 ± 2 %	15 ± 3 %	23 ± 5 %
NBA-66	17 ± 4 %	23 ± 4 %	25 ± 4 %

a) Reported errors are standard deviations from three separate preparations.

Table S2-4. Morphologies[a] and Mean Dimensions[b] of Dialyzed PNBA-*b*-PDMA Nanoparticles

Sample	bulk	25 µL/min	50 µL/min	100 µL/min
NBA-22	S (24 ± 1 nm)	S (24 ± 3 nm)	S (28 ± 1 nm)	S (29 ± 2 nm)
NBA-52	S (25 ± 2 nm)	S (25 ± 1 nm)	S (23 ± 1 nm)	S (25 ± 4 nm)
NBA-66	S (27 ± 1 nm)	S (22 ± 3 nm)	S (24 ± 1 nm) C (27 ± 2 nm)	S (25 ± 1 nm) C (31 ± 4 nm)

a) Morphologies are indicated as S (spheres), and C (cylinders).

b) Reported mean dimensions refer to sphere diameters or cylinder widths. Reported errors for microfluidic-prepared nanoparticles are standard deviations of three separate preparations. Reported errors for bulk-prepared nanoparticles are standard deviations of mean values from three images of a single preparation.

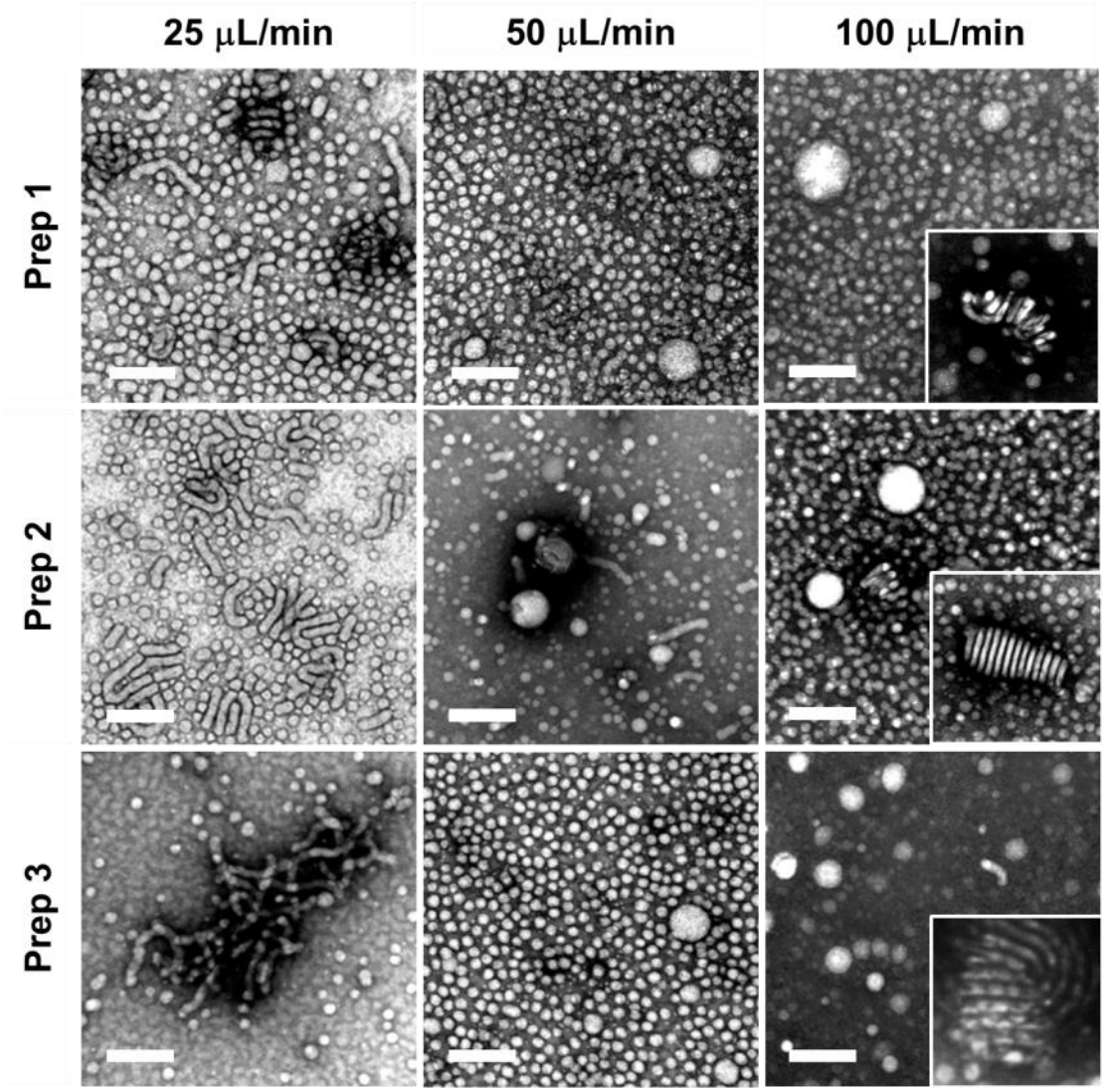

Figure S2-5. Additional TEM images from three separate microfluidic preparations of NBA-22 nanoparticles under various flow conditions. Scale bars are 200 nm.

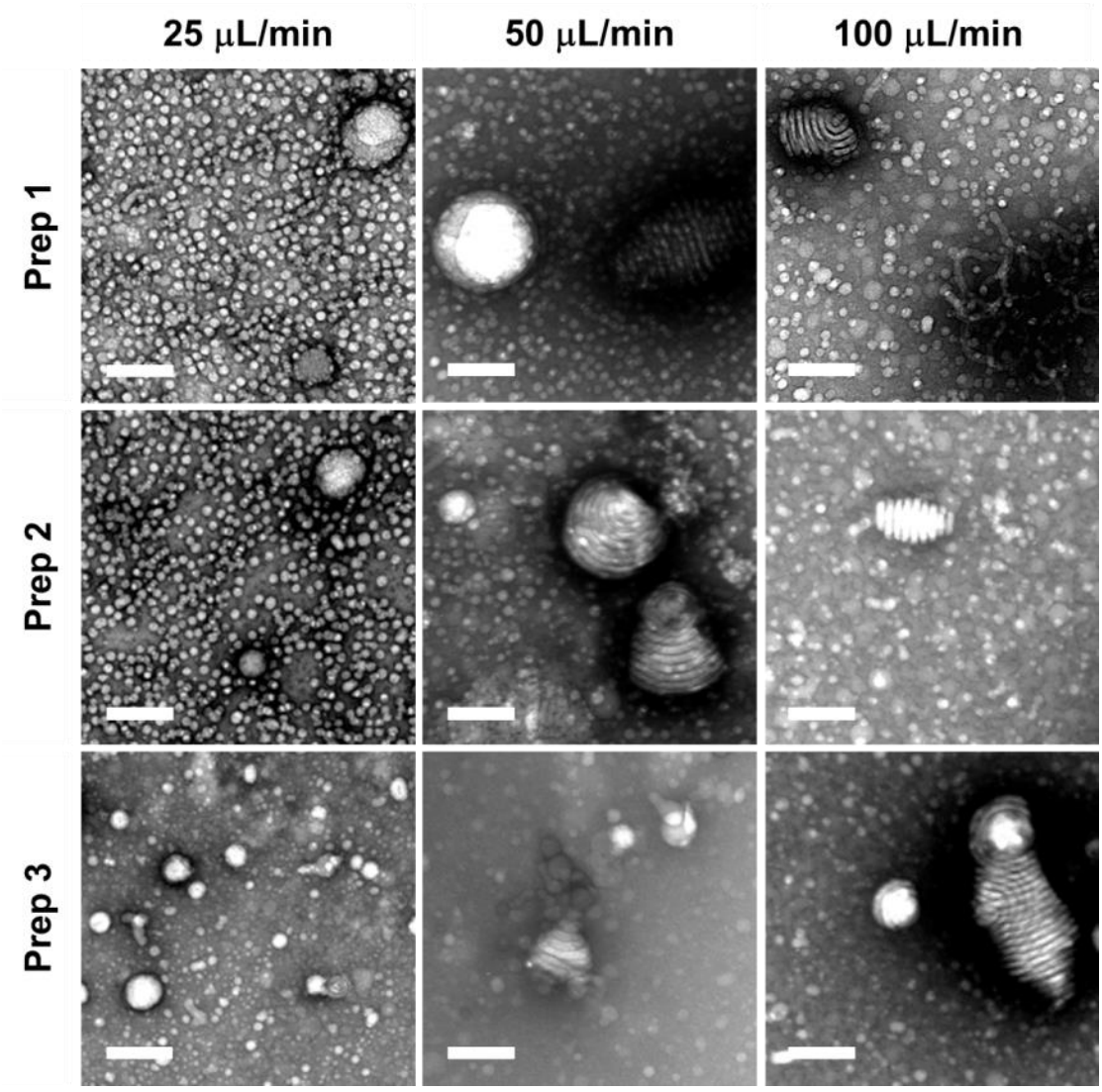

Figure S2-6. Additional TEM images from three separate microfluidic preparations of NBA-52 nanoparticles under various flow conditions. Scale bars are 200 nm.

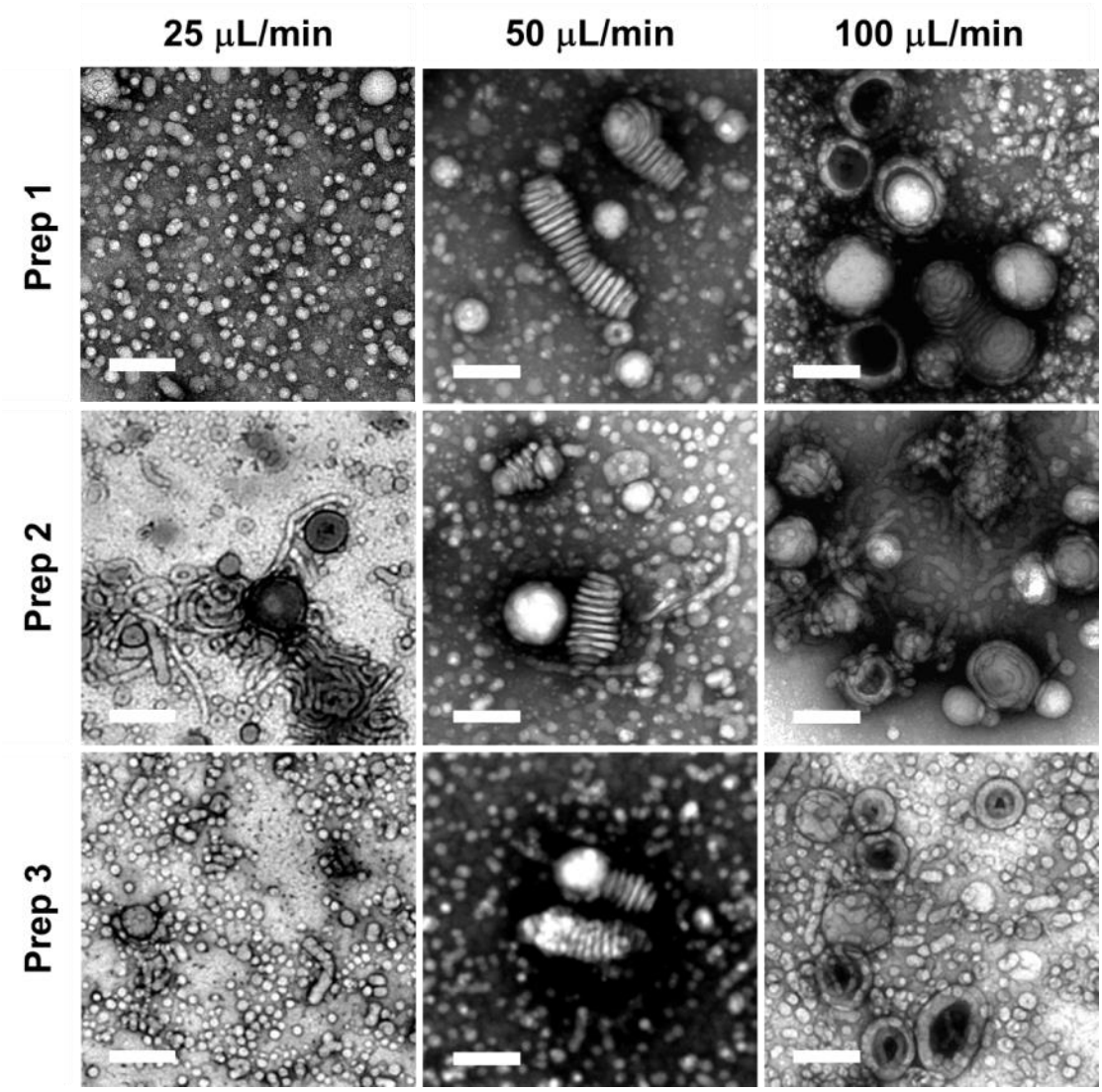

Figure S2-7. Additional TEM images from three separate microfluidic preparations of NBA-66 nanoparticles under various flow conditions. Scale bars are 200 nm.

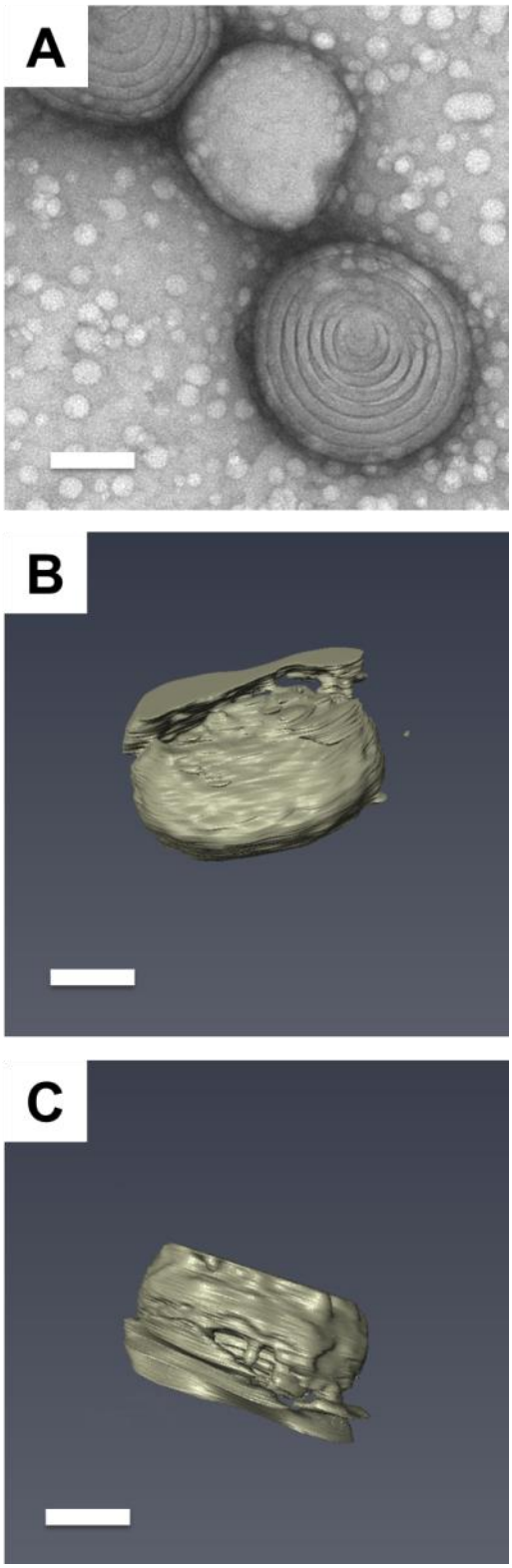

Figure S2-8. 2D TEM image of a compressed spooled cylinder of NBA-66 formed in the microfluidic reactor at 50 μL/min (A) and 3D TEM tomography images of the same nanoparticle taken from two different directions (B and C). Scale bars are 100 nm.

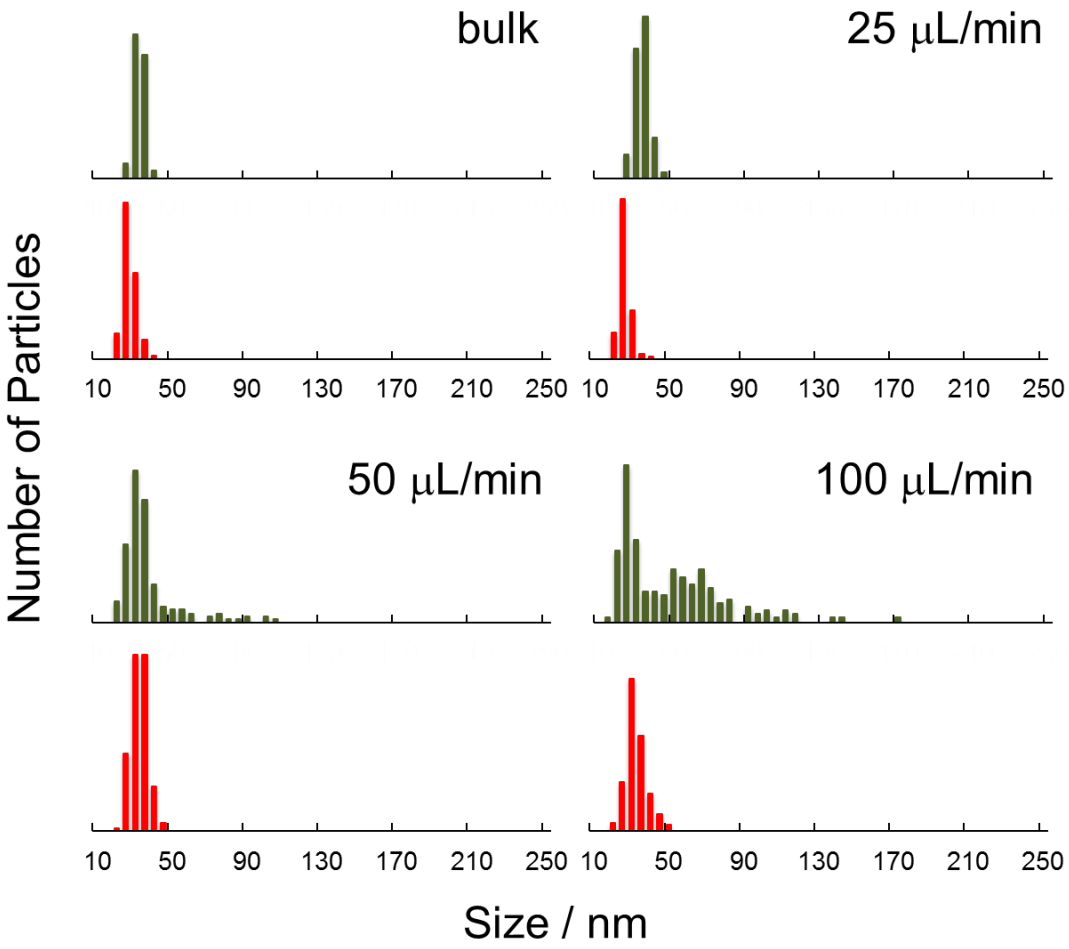

Figure S2-9. Size histograms of unquenched (green) and dialyzed (red) spherical nanoparticles (spheres and LCMs only) for a single preparation of NBA-22 nanoparticles under various flow conditions.

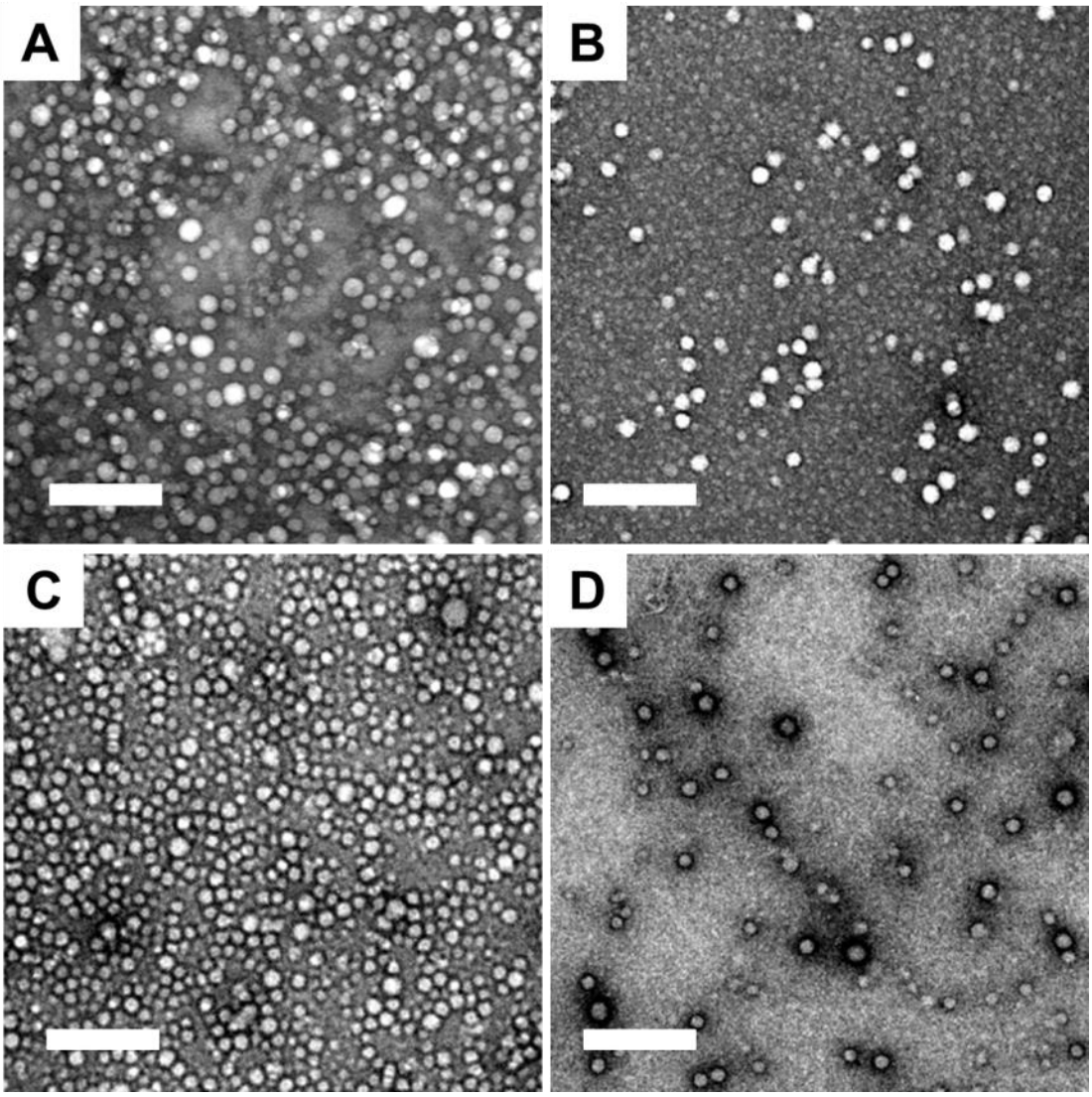

Figure S2-10. TEM images of dialyzed NBA-52 nanoparticles formed in the bulk (A) and in the microfluidic reactor at various flow rates: 25 μL/min (B), 50 μL/min (C), and 100 μL/min (D). Scale bars are 200 nm.

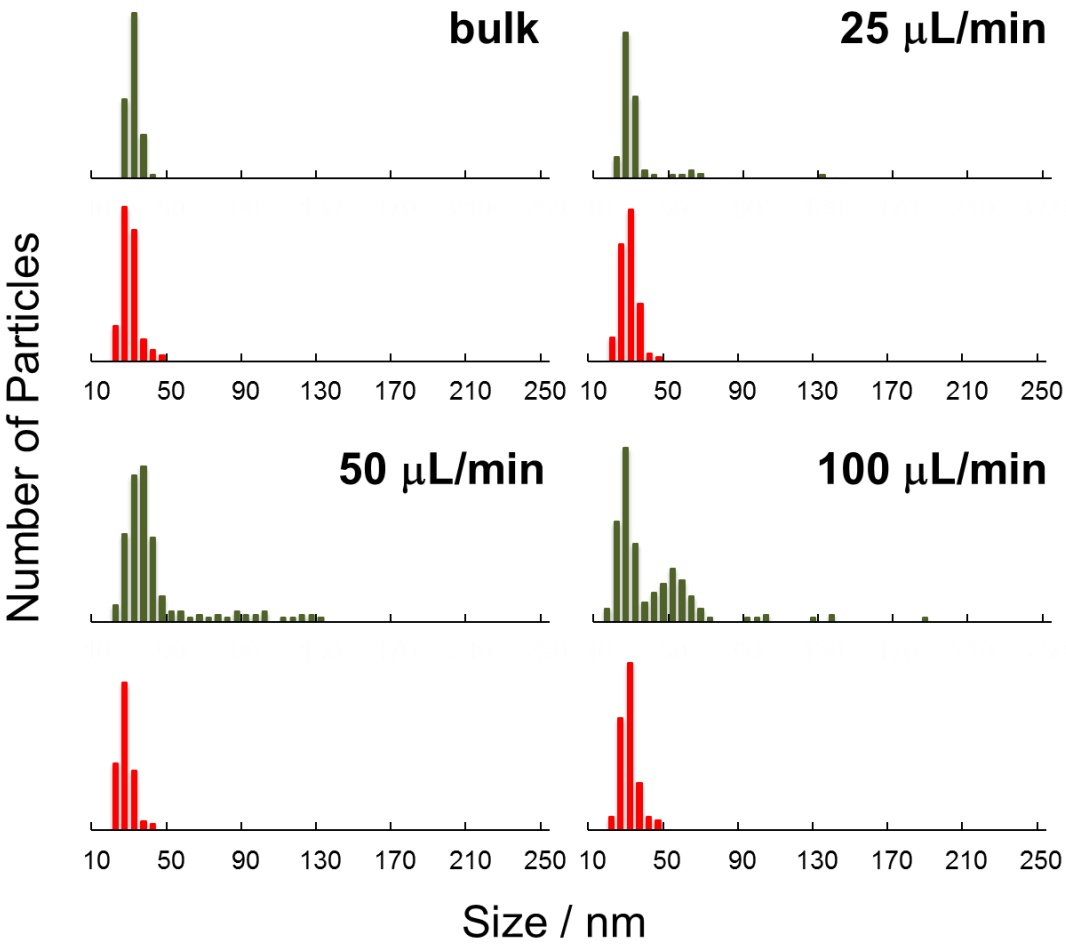

Figure S2-11. Size histograms of unquenched (green) and dialyzed (red) spherical nanoparticles (spheres and LCMs only) for a single preparation of NBA-52 nanoparticles under various flow conditions.

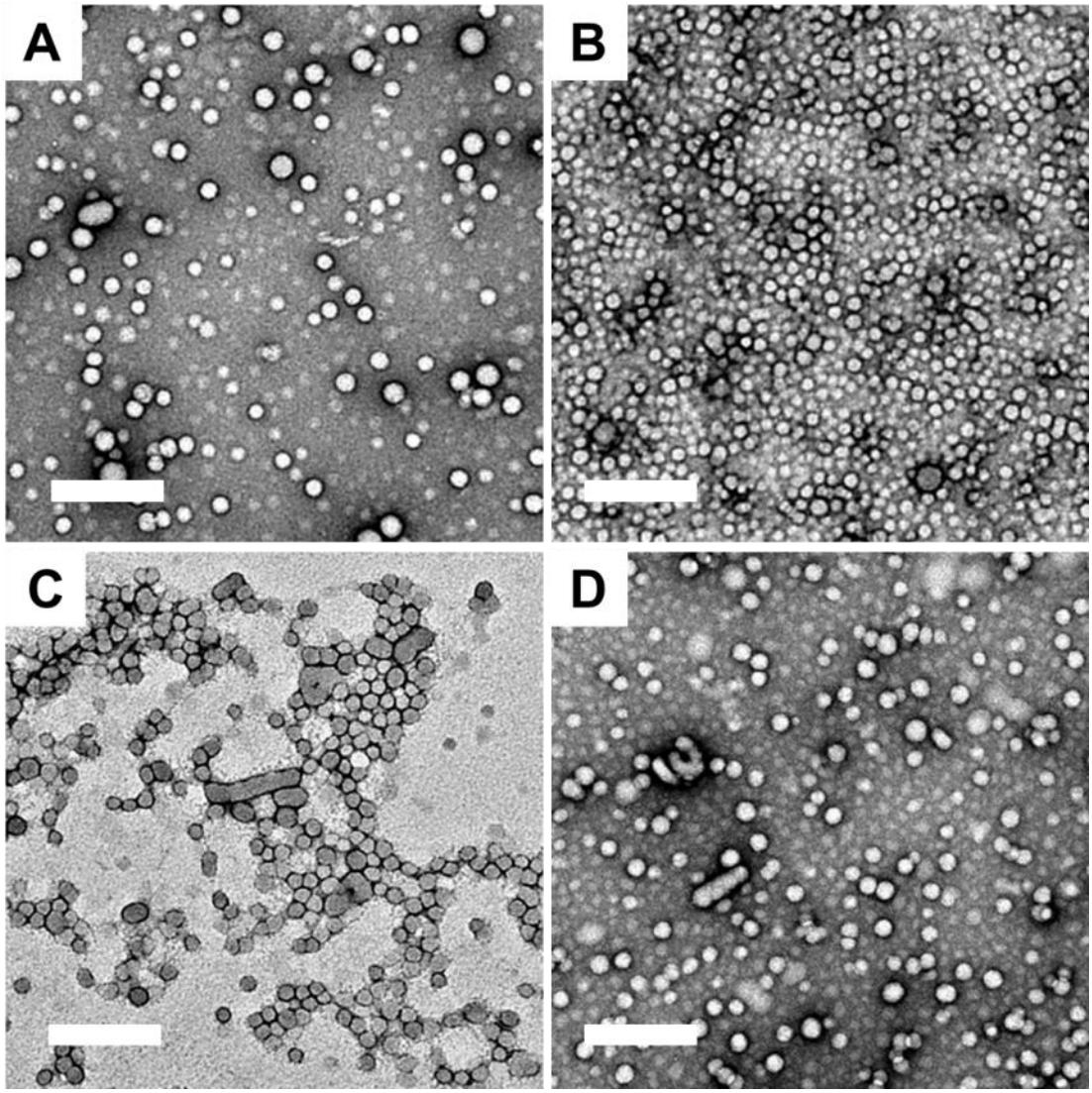

Figure S2-12. TEM images of dialyzed NBA-66 nanoparticles formed in the bulk (A) and in the microfluidic reactor at various flow rates: 25 μL/min (B), 50 μL/min (C), and 100 μL/min (D). Scale bars are 200 nm.

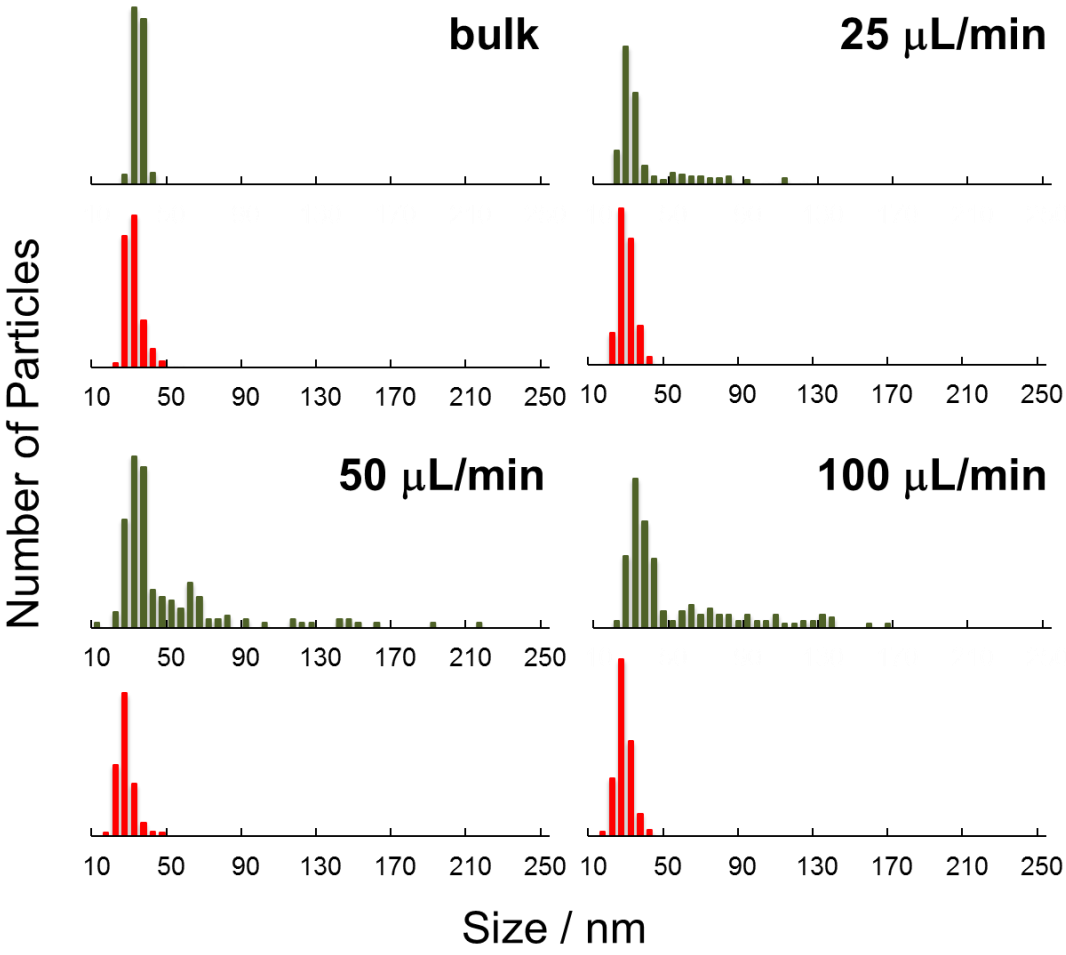

Figure S2-13. Size histograms of unquenched (green) and dialyzed (red) spherical nanoparticles (spheres and LCMs only) for a single preparation of NBA-66 nanoparticles under various flow conditions.

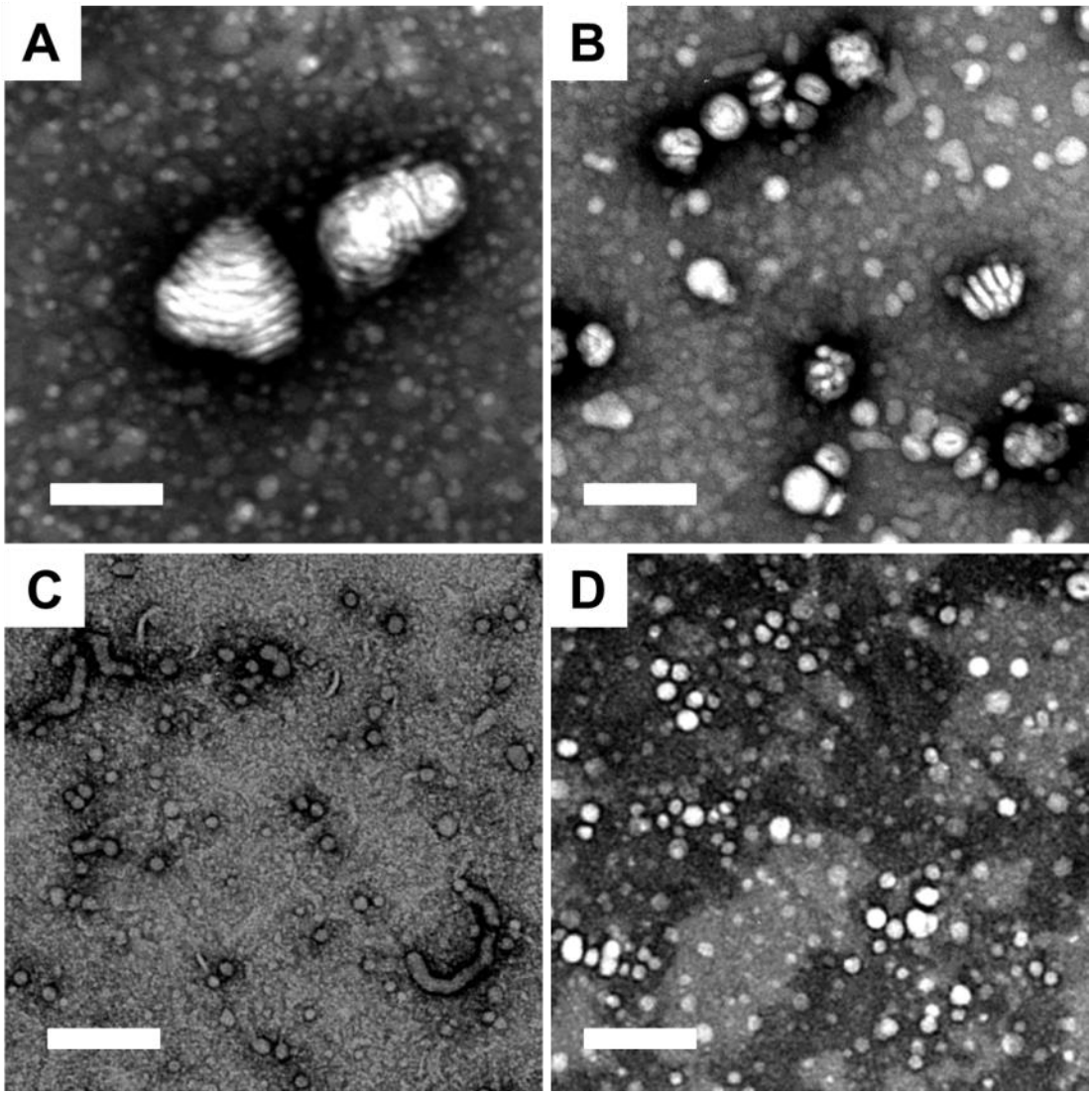

Figure S2-14. TEM images of unquenched NBA-52 nanoparticles formed in the microfluidic reactor at 100 μL/min and imaged immediately (A), and corresponding aged nanoparticles after 1 day (B), 3 days (C) and 7 days (D). Scale bars are 200 nm.

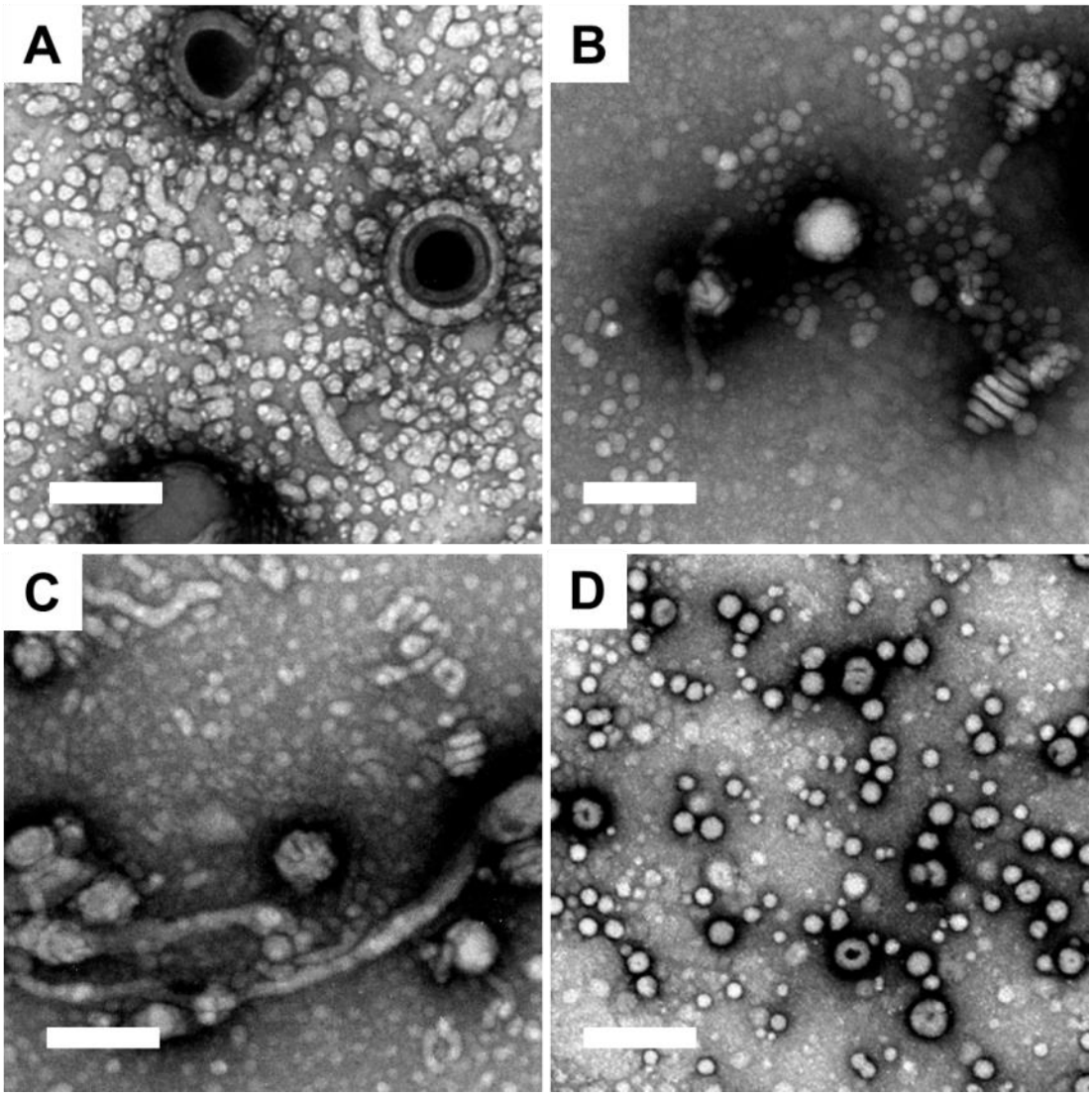

Figure S2-15. TEM images of unquenched NBA-66 nanoparticles formed in the microfluidic reactor at 100 μL/min and imaged immediately (A), and corresponding aged nanoparticles after 1 day (B), 3 days (C) and 7 days (D). Scale bars are 200 nm.

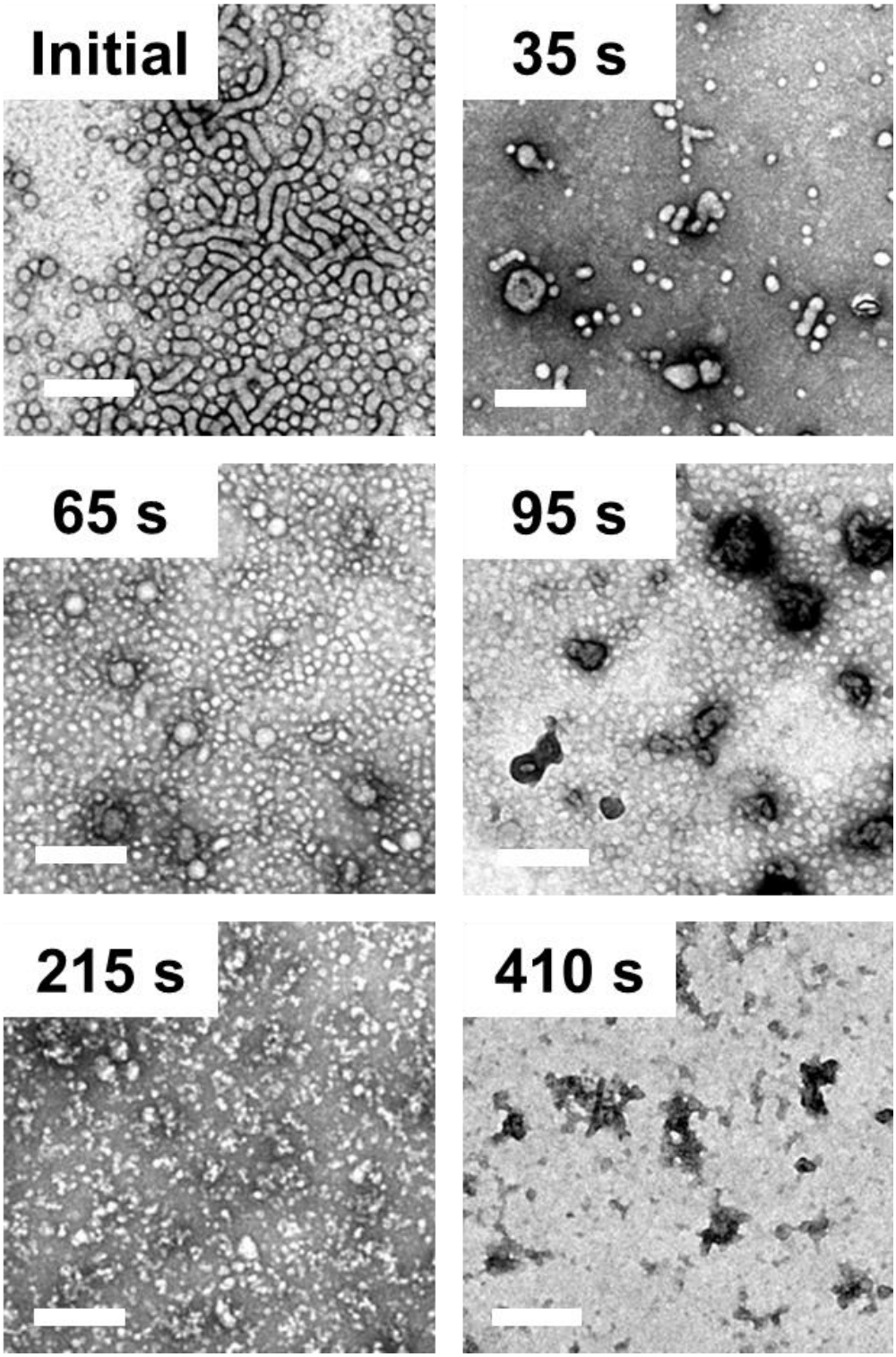

Figure S2-16. Larger version of TEM images (from Figure 8) of irradiated NBA-22 nanoparticles formed in the microfluidic reactor at 25 μL/min for different irradiation times. Scale bars are 200 nm.

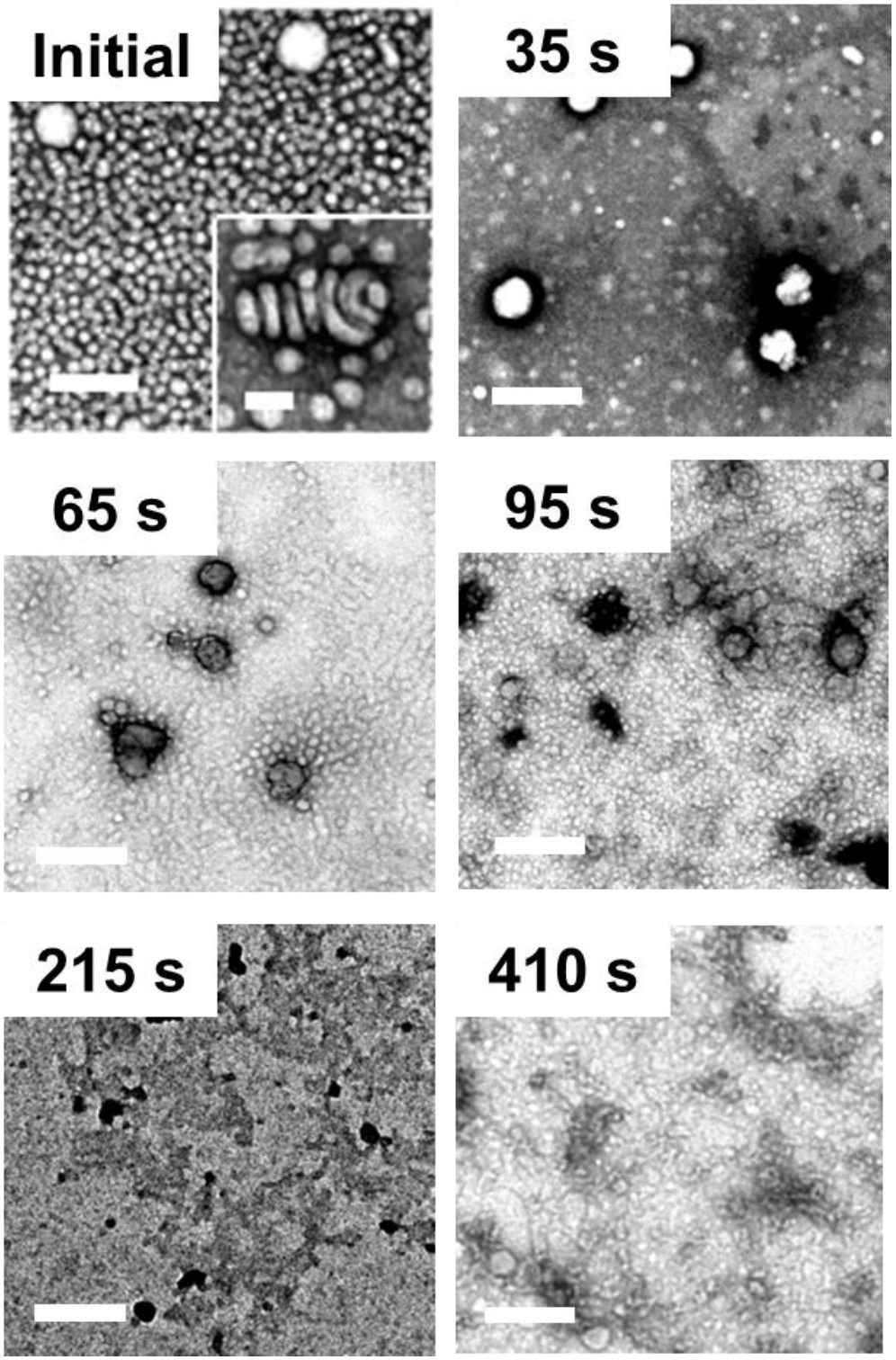

Figure S2-17. Larger version of TEM images (from Figure 8) of irradiated NBA-22 nanoparticles formed in the microfluidic reactor at 100 μL/min for different irradiation times. Inset to "Initial" shows a spooled cylinder found in a different region of the same sample. Scale bars are 200 nm (main images) and 50 nm (inset to "Initial").

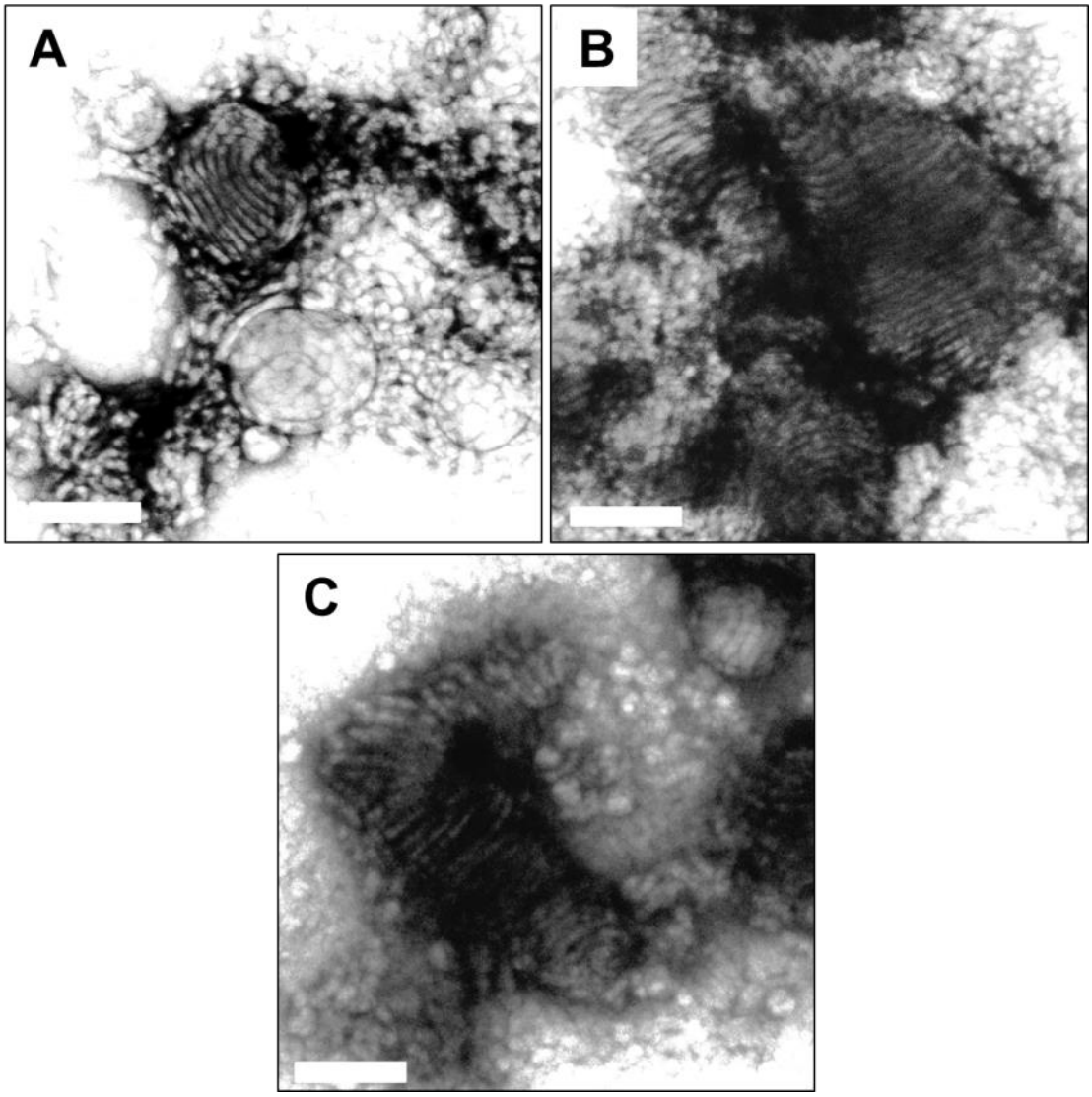

Figure S2-18. TEM images of unquenched NBA-66 nanoparticles prepared in the microfluidic reactor at 50 μL/min. TEM grids were prepared by freeze drying with negative staining. Similar spooled cylinders to TEM grids of the same sample prepared by drop deposition are observed. This indicates that these morphologies are present in solution and do not form during drying on the TEM grid. Scale bars are 200 nm.

Appendix B

Supporting Information for Chapter 3

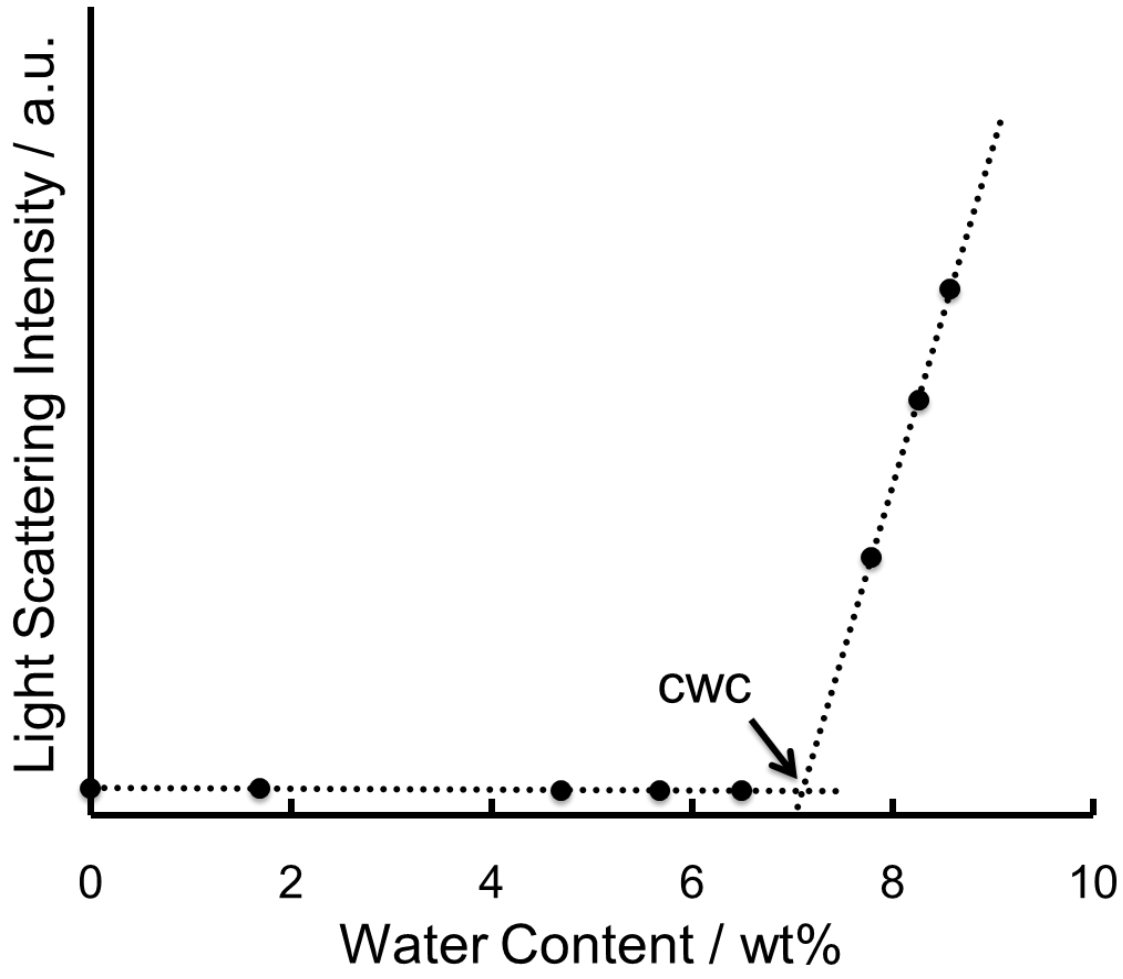

Figure S3-1. Titration curve of critical water content determination of PCL-5k.

Table S3-1: Actual Gas and Liquid Flow Rates for PCL-*b*-PEO Nanoparticles Prepared on Segmented Microfluidic Reactor.

Copolymer, Nominal Flow Rate	L_{gas} (mm)	L_{liq} (mm)	Q_{gas} (µL/min)	Q_{liq} (µL/min)	Q_{gas}/Q_{liq}	Q_{total} (µL/min)
PCL-5k						
20 µL/min	1.1	1.0	11.8	10	1.18	21.8
60 µL/min	2.5	2.3	31.7	30	1.06	61.7
100 µL/min	1.7	1.6	52.4	50	1.05	102.4
PCL-12k						
20 µL/min	0.8	0.9	8.7	10	0.87	18.7
60 µL/min	1.9	1.8	32.1	30	1.07	62.1
100 µL/min	1.7	1.8	46.6	50	0.93	96.6

Appendix C

Supporting Information for Chapter 4

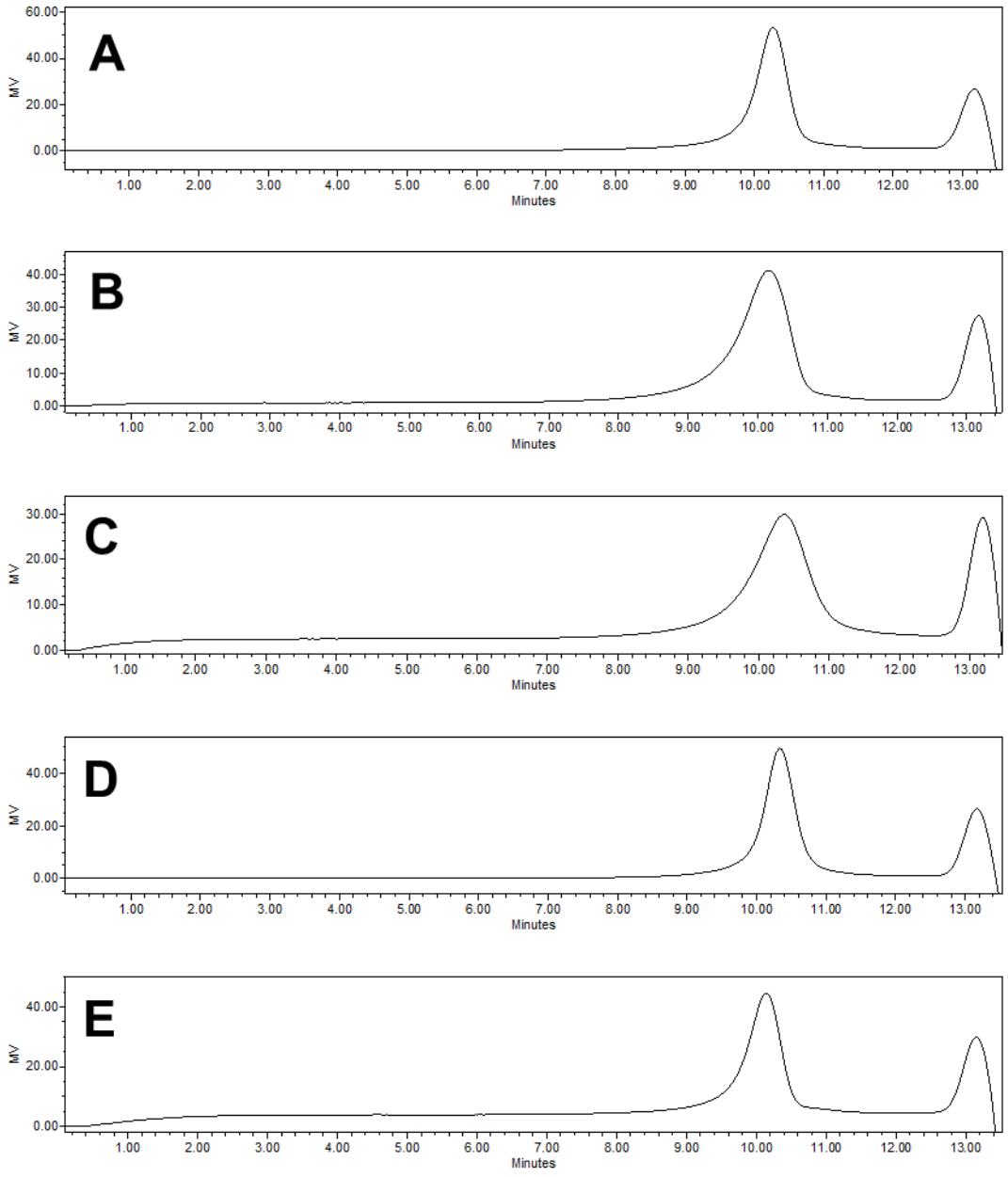

Figure S4-1. GPC traces of P(MCL-*co*-CL)-*b*-PEO. (A) PMCL-0. (B) PMCL-25. (C) PMCL-50. (D) PMCL-75. (E) PMCL-100.

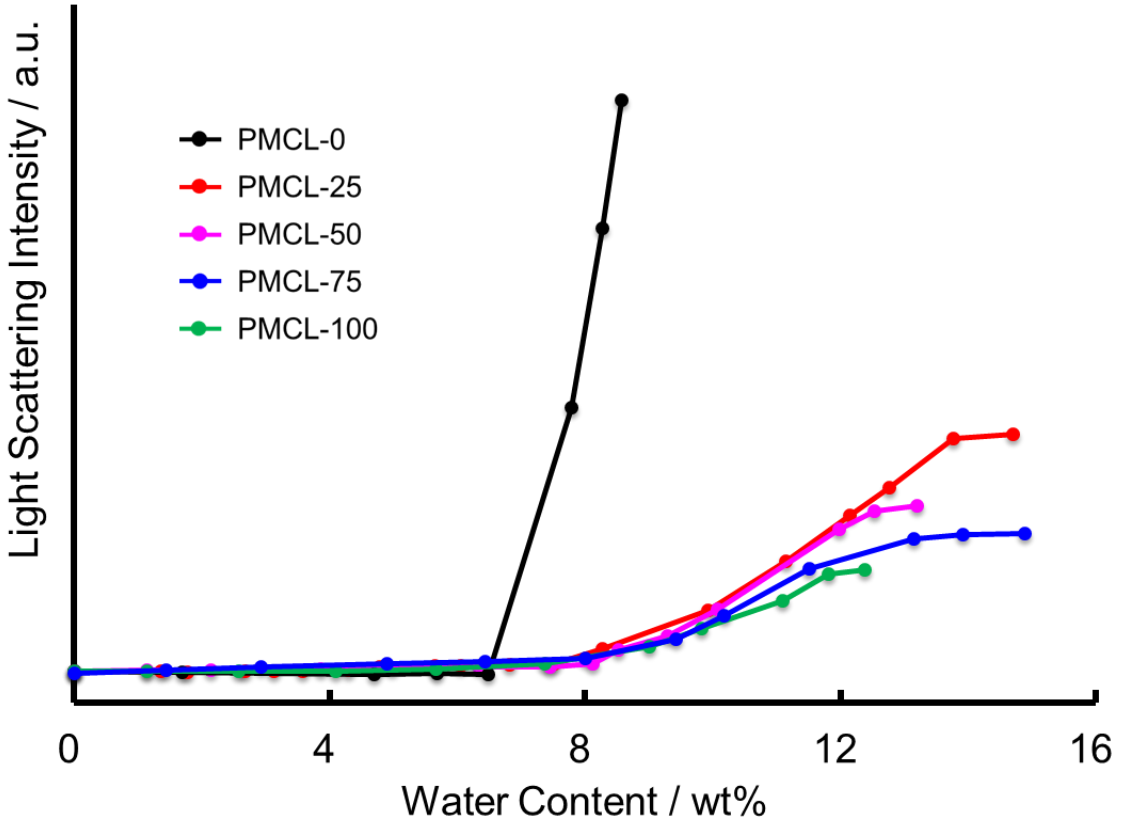

Figure S4-2. Titration curves of cwc determination of series of P(MCL-*co*-CL)-*b*-PEO.

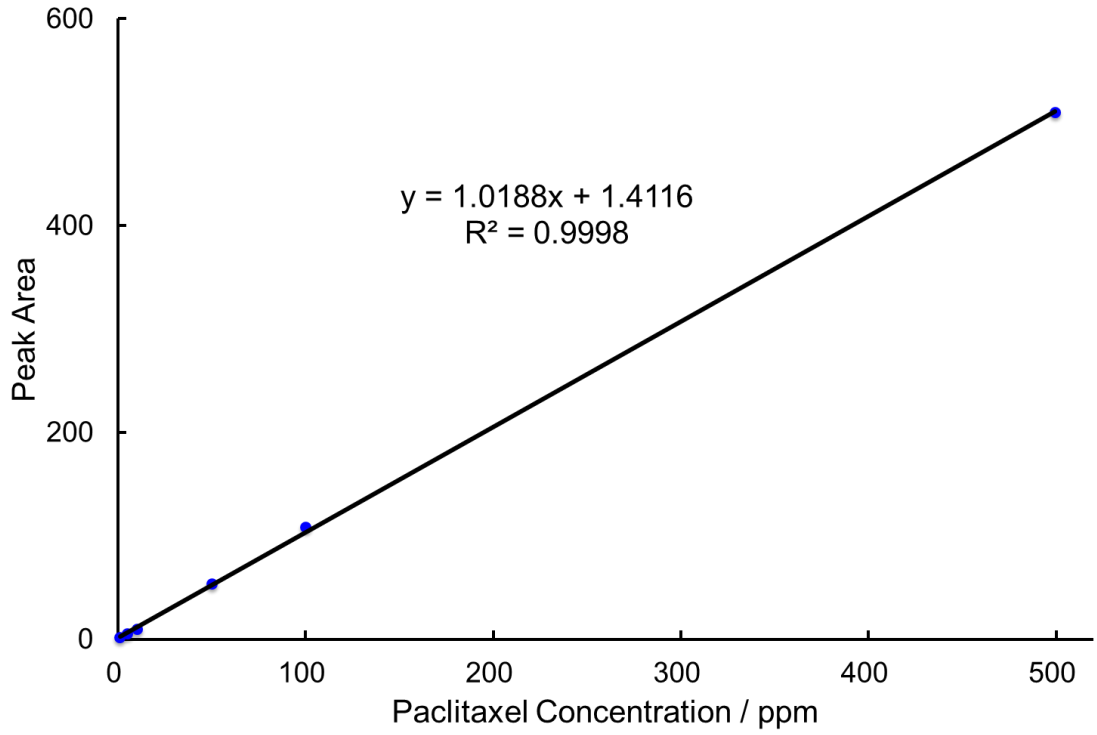

Figure S4-3. Calibration curve of paclitaxel in acetonitrile quantified by HPLC with DAD at 227 nm as detector.

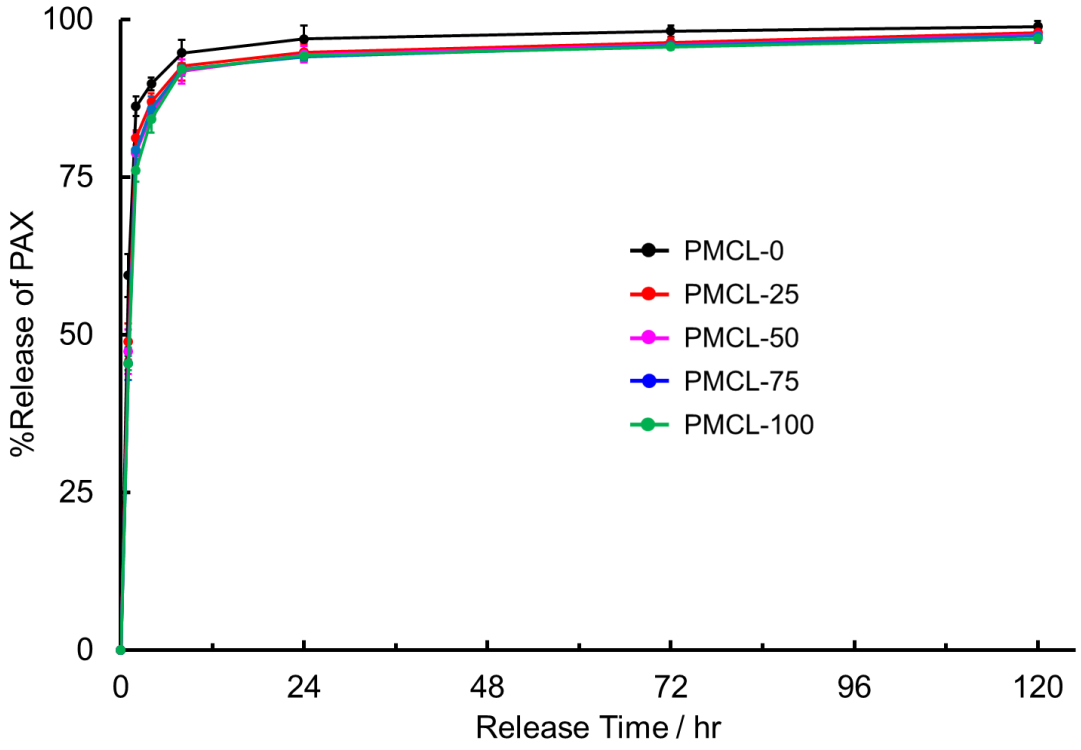

Figure S4-4. Effect of PMCL fraction on *in vitro* release profile of paclitaxel-loaded P(MCL-*co*-CL)-*b*-PEO nanoparticles (r = 0.25) prepared in the bulk over 5 days. Errors are standard deviations of mean values determined for three separate preparations.

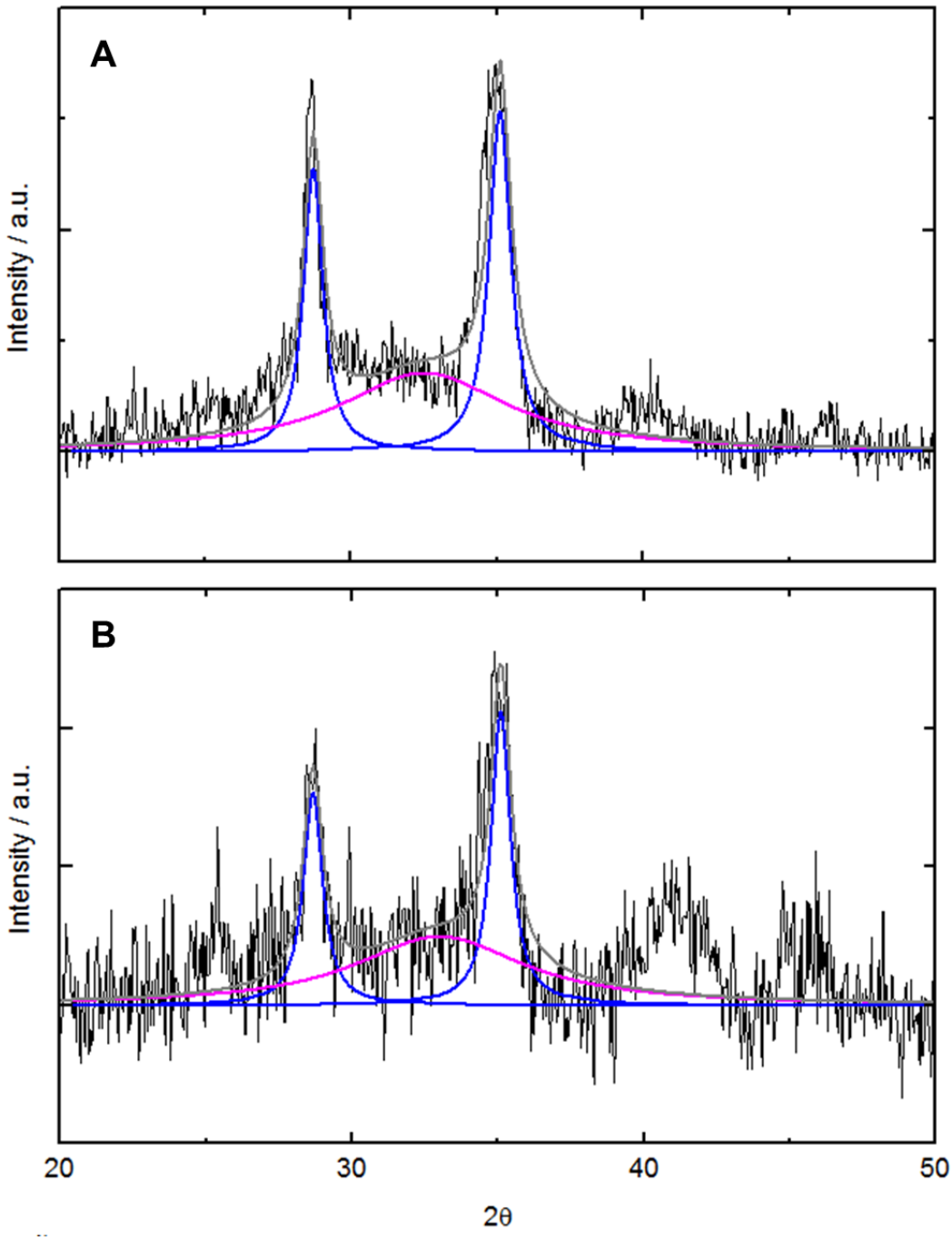

Figure S4-5. XRD patterns and fitting of PMCL-25 nanoparticles formed in bulk (A) and at 50 μL/min on gas-liquid segmented microfluidic reactor (B).

Appendix D

Evaluation of Different Methods of Extracting PAX from PBS Buffer Components during *In Vitro* Release Experiments

Experimental

A key issue in carrying out *in vitro* experiments of hydrophobic drugs or probes from drug delivery nanoparticles into PBS release medium is how to extract the drug from the aqueous PBS salt medium into pure ACN for HPLC injection. According to the literature, there are several methods to extract the drug from the PBS medium, including liquid-liquid extraction with dichloromethane[1-3] or *t*-butyl methyl ether,[4] filtration,[5-7] centrifugation[8] and direct dilution.[9] A key figure of merit for these extraction methods is the percentage of recovery, which is the amount of drug within the aliquot that is extracted for HPLC analysis. If the percentage of recovery is significantly less than 100%, then an internal standard may be necessary to normalize the measured drug amount relative to loss of drug due to the extraction method. Rather than relying on the additional complication of an internal standard, we set out to evaluate if an extraction method with close to 100% recovery could be developed such that an internal standard was not required. To do this, we evaluated three different extraction methods: 1) liquid-liquid extraction into *t*-butyl methyl ether, 2) liquid-liquid extraction into dichloromethane and 3) removal of solvent from the aliquot by rotary evaporation, followed by extraction of drug from the dried solids using ACN.

The following experiment was carried out using the PAX-loaded PMCL-50 nanoparticles prepared in the bulk (r = 0.25) from three separate preparations.

Dialyzed nanoparticles was centrifuged to remove precipitate and transferred into 4 glass vials, each containing 2 g of sample. One of the vials was designated as the control and the procedures for loading efficiency determination were followed. The aim for the control is to get the real concentration of the sample.

Solutions in other vials were dried by rotary evaporation and then the solid nanoparticles obtained were redispersed in PBS to mimic the solution environment after release. Each vial was used to investigate one of the methods.

For method 1 and 2, 2 mL of *t*-butyl methyl ether or DCM was added to nanoparticles in PBS. The mixture was vortexed for 5 min, allowed to settle for 10 min and then the organic layer was removed by a Pasteur pipet. This step was repeated for 3 times, and then all organic layers removed were combined and dried by rotary evaporation. 0.2 g ACN was added to the vial to dissolve copolymer and drug. The vial was vortexed for 2 min to aid dissolution and then injected into HPLC.

For method 3, nanoparticles in PBS were dried by rotary evaporation. The salt crystals from PBS and solid nanoparticles were obtained. 0.2 g ACN was added to the vial to dissolve the nanoparticles while leaving the salt crystals on the inner wall of the glass vial. The vial was vortexed for 2 min to aid dissolution. The solution was then carefully decanted into an HPLC vial and injected into HPLC.

For each method, the percentage of recovery was determined by evaluating by HPLC the concentration of extracted drug relative to the concentration of drug in the control. It is calculated using the following equation:

$$\%Recovery = \frac{Concentration\ of\ sample}{Concentration\ of\ control} \times 100\% \qquad \text{(D-1)}$$

For the evaporation method (method 3), we also evaluated the effect of salt and drug concentration on the percentage of recovery, since these two concentrations will change throughout the *in vitro* release experiment, as drug diffuses into the release medium from the sample and salt diffuses from the release medium into the sample. The initial drug concentration and a 5 times diluted drug concentration (equals to 80% release) was studied. The PBS buffer we use in release experiments and a 2 time diluted PBS was investigated. These results are tabulated in Table D-2.

Results and Discussion

Three different methods were assessed to extract the PAX from the aqueous PBS medium into pure ACN: 1) liquid-liquid extraction into *t*-butyl methyl ether, 2) liquid-liquid extraction into dichloromethane, and 3) removal of solvent from the aliquot by rotary evaporation, followed by extraction of drug from the dried solids using ACN (direct drying). The results are tabulated in Table D-1. It obvious that direct drying has a much higher percentage of recovery. This is because liquid-liquid extraction is an equilibrium process in which recover of PAX is dependent on the partition coefficient. Loss of drug in these methods is inevitable. However, for the drying method, the dried salt sticks to the inner wall of glass vials, so only drug and polymer in ACN can be pipetted out. Loss of drug happens when it is trapped in the salt. Therefore, the drug concentration and salt concentration should have an effect on %recovery. During release, drug concentration decreases because released drug will diffuse from sample dialysis tube into medium, while salt concentration increases due to diffusion of drug from the release medium into sample dialysis tube. Therefore, samples at different release time will have different drug and salt concentrations.

Table D-1. %Recovery[a] of different methods. 1. liquid-liquid extraction into *t*-butyl methyl ether. 2. liquid-liquid extraction into dichloromethane 3. direct drying.

Method	1	2	3
%Recovery	61.7 ± 1.4	69.2 ± 1.6	92.1 ± 2.5

a) Errors are standard deviations of mean values determined for three separate preparations.

The %recovery of drying method at different drug and salt concentrations are tabulated in Table D-2. As expected, concentration of salt has a more profound effect on %recovery and less drug lead to higher % recovery as fewer drugs could be trapped. However, concentration of paclitaxel doesn't seem to affect %recovery much. An explanation is that our drug concentration is low enough that any change is insignificant in the process. Overall, at the concentration range investigated, %recovery of drying method is high. Therefore, it is employed in this study without measurement of and correction to %recovery for each sample.

Table D-2. Effect of PAX and PBS concentrations on %recovery for evaporation method.

PAX/polymer ratio	PBS	PBS diluted by 2
0.05 w/w (no dilution)	92.1 ± 2.5	98.5 ± 0.6
0.01 w/w (diluted by 5)	93.3 ± 0.3	96.6 ± 1.0

a) Errors are standard deviations of mean values determined for three separate preparations.

References

1. A. Kumar, P. Srinivas, K. Spandana, N. Rama and J. VidyaSagar Rapid and Sensitive Hplc Method for the Determination of Sirolimus with Ketoconazole as Internal Standard and Its Further Applications. *International Journal of Pharmaceutical Sciences Drug Research* **2012,** *4*, 70.

2. L. Mu and S. S. Feng Vitamin E Tpgs Used as Emulsifier in the Solvent Evaporation/Extraction Technique for Fabrication of Polymeric Nanospheres for Controlled Release of Paclitaxel (Taxol®). *Journal of Controlled Release* **2002,** *80*, 129.

3. H. Chu, N. Liu, X. Wang, Z. Jiao and Z. Chen Morphology and in Vitro Release Kinetics of Drug-Loaded Micelles Based on Well-Defined Pmpc–B–Pbma Copolymer. *International Journal of Pharmaceutics* **2009,** *371*, 190.

4. S. Li, B. Byrne, J. Welsh and A. F. Palmer Self-Assembled Poly(Butadiene)-B-Poly(Ethylene Oxide) Polymersomes as Paclitaxel Carriers. *Biotechnology Progress* **2007,** *23*, 278.

5. A. Potineni, D. M. Lynn, R. Langer and M. M. Amiji Poly(Ethylene Oxide)-Modified Poly(B-Amino Ester) Nanoparticles as a Ph-Sensitive Biodegradable System for Paclitaxel Delivery. *Journal of Controlled Release* **2003,** *86*, 223.

6. F.-Q. Hu, G.-F. Ren, H. Yuan, Y.-Z. Du and S. Zeng Shell Cross-Linked Stearic Acid Grafted Chitosan Oligosaccharide Self-Aggregated Micelles for Controlled Release of Paclitaxel. *Colloids and Surfaces B: Biointerfaces* **2006,** *50*, 97.

7. S. Cai, K. Vijayan, D. Cheng, E. Lima and D. Discher Micelles of Different Morphologies—Advantages of Worm-Like Filomicelles of Peo-Pcl in Paclitaxel Delivery. *Pharm Res* **2007,** *24*, 2099.

8. Y. Geng and D. E. Discher Visualization of Degradable Worm Micelle Breakdown in Relation to Drug Release. *Polymer* **2006,** *47*, 2519.

9. T. Yang, F.-D. Cui, M.-K. Choi, J.-W. Cho, S.-J. Chung, C.-K. Shim and D.-D. Kim Enhanced Solubility and Stability of Pegylated Liposomal Paclitaxel: In Vitro and in Vivo Evaluation. *International Journal of Pharmaceutics* **2007,** *338*, 317.